Development and Application of Therapeutics for Repair of Polytraumatic Volumetric Muscle Loss Injuries

---

Dissertation of

Jonathan S Turner

Submitted in partial fulfillment of the requirements for the degree of

Doctor of Philosophy under the Executive Committee

of the Graduate School of Engineering and Applied Science at the University of Virginia

Read and Approved by the Examining Committee:

George J. Christ, PhD, Advisor

Shayn Peirce-Cottler, PhD, Committee Chair

Don Griffin, PhD

Kacey Marra, PhD

Steven Caliari, PhD

David Weiss, MD

Biomedical Engineering

2022

Acknowledgements

This dissertation is the result of a long, arduous, and amazing journey through research and studies at the University of Virginia in pursuit of a Ph.D. in Biomedical Engineering. I would like to express my thanks and gratitude to all the people that helped me get here. First and foremost, I would like to acknowledge my advisor, Dr. George Christ, for his constant guidance. He was always what I needed him to be, kind and understanding when I could use it, direct and heavy handed when I required it, a joke and a laugh in the office, or a pep talk in private, I could not have gotten through this experience without him. I would like to thank my research collaborators; Kyle Christensen, Michael Francis, Baris Bengur, Kacey Marra, and Brian Jones. Thank you to my committee chair, Dr. Shayn Peirce-Cottler, for her unyielding support. Thank you to my entire committee, Dr. Don Griffin, Dr. Steven Caliari, Dr. Kacey Marra, and Dr. David Weiss for their hard work, patience, enthusiasm, and thought-provoking questions. I would like to acknowledge all the faculty and front office staff in the UVA BME department. From the very first faculty I encountered at UVA to my last day as a student, I have felt supported and guided through the entire process, they have garnered a sense of community and developed an excellent program. I would also like to thank Poonam Sharma, Juliana Passipieri, Ellen Mintz, Sarah Dyer, Rachel Bour, Michael Rariden, Olivia Sergent, Sydney Shriver, Christian Tessman and the other members of the Christ Lab for their help in learning new research techniques, keeping the lab running, bouncing ideas around, or occasionally just staying sane. I would like to acknowledge Mari-Peyton Kouchinsky for standing by my side during the hardest of times and providing the motivation and support I needed to get through this. Lastly, a final thanks to my parents, children, and close friends for supporting me through this journey day in and day out.

I dedicate this dissertation to my three children, who are the reason for everything I do, Daphne Turner, Jack Turner, and Eliza Turner. I also dedicate this to my parents, John and Moira Turner, for helping me towards this goal and never giving up on me.

Abstract

Volumetric muscle loss (VML) injuries lead to permanent functional and cosmetic deficits and are a serious challenge faced by both civilian and military personnel. Further complicating repair of these injuries is extensive simultaneous damage to multiple tissue components, such as nerve and bone outside of the VML injury. Currently there are no therapies available that can completely restore neuromuscular function following polytraumatic VML injury. As a first step in that direction, this thesis proposal work will address the need for therapies targeting repair of both nerve and muscle, in order to improve functional outcomes for polytraumatic VML repair. First, co-culture and bioprinting techniques were applied for the biofabrication of tissue engineered repair constructs. Specifically, in vitro examination of bioprinted HA hydrogels laden with cells reveals the potential for bioprinting of scaffolds incorporating multiple cell types, with a tunable cell matrix architecture. The efficacy of a preferred therapeutic construct, that is, an Assembled Cell-Decorated Collagen (AC-DC) scaffold, was evaluated in a biologically relevant rat tibialis anterior (TA) VML model injury. Longitudinal studies of functional recovery were conducted over a 12 week time frame following surgical creation of a TA VML injury—with or without repair. Second, an in vitro co-culture strategy is evaluated for building engineered skeletal muscle that permits survival of nerve and muscle progenitor cells under identical cell culture conditions. Finally, we have endeavored to identify a reproducible and repairable nerve injury model in vivo that would permit simultaneous repair of muscle and nerve damage to the TA muscle. In short, this dissertation highlights the extant challenges and opportunities associated with designing novel therapeutics that incorporate a variety of cell types and architectures to improve regenerative support for polytraumatic VML injury.

Table of Contents

List of Figures and Graphs

Chapter 2

Chapter 3

Chapter 4

Chapter 1: Introduction to *Volumetric Muscle Loss, Polytraumatic Injuries* and tissue engineering approaches for regeneration/repair

(1.1) Volumetric Muscle Loss and Polytraumatic Injuries

Skeletal muscle comprises the largest portion of tissue in the human body and is composed of well-organized extracellular matrix (ECM), with high levels of innervation and vascularization throughout. All of these components are necessary in order for muscle to maintain full function and maximum efficiency (Mauro, 1961, Passipieri and Christ, 2016). Musculoskeletal tissue injuries are commonplace in athletes, military men and women, and civilians alike with over 60 million injuries reported annually in the United States alone. For warfighters in particular, extremity injuries account for up to 70% of trauma cases in theater (Covey, 2002) and are the leading cause for medical treatment in warfighters with ~2 million cases per year (Corona *et al.*, 2013). These injuries can cause permanent loss of function and crippling disabilities for service men and women, often preventing return to duty and leading to long term physical rehabilitation and costly treatments that may last a lifetime. Additionally, at least 20 million injuries to extremities are reported in traffic incidents, while at least 35% of sports injuries also involve muscle damage at the myofiber level (Liu *et al.*, 2018). Treatment costs alone can exceed 176 billion dollars a year with substantially greater costs in loss of productivity and disability costs. This highlights the importance of regenerative medicine approaches for both military and civilian populations that target functional and cosmetic recovery of musculoskeletal extremity injuries.

While the regenerative capacity of typical muscle injuries is well known, in severe traumatic injuries, for example, the endogenous capacity of muscle repair is exceeded. When muscle is damaged past the extent of endogenous repair, this is deemed a volumetric muscle loss (VML) injury.

By definition, VML injuries result in permanent functional and cosmetic deficits, and in many cases are associated with multi-level loss of tissue components, such as bone, tendon, nerve, and vessel. This means they are characterized by their polytraumatic nature, affecting significantly more than muscle tissue alone. Polytraumatic injuries, like VML commonly occur in the extremities, caused by high impact blunt force traumas, collisions, and high-grade muscle tears, and thus, may include damage to ligaments, tendons, bones and peripheral nerves. The effectiveness and long-term outcomes of current treatment options are often limited. Available therapies for polytraumatic VML injuries rely on surgical repairs, such as autografting, which lead to loss of function and morbidity at the donor site (Seon, Song and Park, 2006), while cadaveric grafts can be subject to complications due to tissue availability and immunoreactivity/biocompatibility. VML injuries can also be treated using microsurgery or flap transfer procedures, but both methods require significant lengths of physical rehabilitation and flap transfer procedures do not show high levels of functional recovery. Thus, regenerative medicine and tissue engineering approaches need to be developed that can provide efficient, long-term repair of muscle tissue while also targeting the peripheral damage to tissues in the area. This will allow for a more complete recovery of polytraumatic injuries.

Even though many traumatic injuries affect multiple tissue types, current studies regarding VML injury repair address only the immediate damage to the muscle tissue, for mechanistic clarity. This leaves a gap in knowledge and treatment options where the interactions of multiple tissues are of the utmost importance, for example nerves that provide signals to muscle tissue downstream. Nerve damage due to VML injury is common and can include damage to peripheral and intramuscular nerves, neuromuscular junctions, and motoneuron-muscle fiber signaling may be disrupted (Corona, Rivera and Greising, 2018). Peripheral nerve damage causes disruption of nerve fibers and Wallerian degeneration, leading to a progressive breakdown of the distal end of nerve fibers and disruption of the neuromuscular junction(s)/synapses within the target muscle. Because the simultaneous loss of nerve and muscle tissue exacerbates the functional recovery process, restoration of neuronal integrity

must be included in any therapeutic strategy for complete functional recovery from polytrauma. While there are currently no effective treatments for such injuries, regenerative medicine and tissue engineering approaches are rapidly developing and could be adapted in the future towards polytraumatic repair. Key considerations when designing tissue engineering constructs are the cell type delivered and the delivery method or scaffold to facilitate growth. Seeking to repair polytraumatic injuries, tissue engineering design considerations should carefully select scaffold and cell delivery methods capable of facilitating regeneration in multiple tissue types. In the instance of polytraumatic VML, this may include, but is not limited to skeletal muscle, peripheral and intramuscular nerves, tendon, and bone. The use of emerging technologies, such as bioprinting and advanced biomanufacturing processes have been explored within this work to address the needs for polytraumatic injury repair, in particular with regards to volumetric muscle loss.

(1.2) Scaffold and Cell-based Approaches for Volumetric Muscle Loss Injuries

In addition to the work presented here, current work in the field explores many other applications of scaffold and cell-based approaches for VML repair and have shown effective, functional recovery of muscle tissue. Current literature addressing scaffold-based approaches for tissue engineering typically focus on one tissue type and most relevant to the objective set forth in this paper are VML injuries. Many of these exciting approaches could be explored further and may be useful in the design of polytraumatic injuries. For example, Corona *et al* (2013) used syngeneic muscle derived ECM scaffolds, which showed functional improvement over no treatment at 2 and 4 months post-injury, but not at 6 months post-injury. Our group has developed, over the last several years, the tissue-engineered muscle repair (TEMR) technology platform. The TEMR technology has been extensively researched in a variety of injury models by a number of researchers, it was designed

to enhance endogenous skeletal muscle repair by creating a more favorable microenvironment for regeneration. In brief, the TEMR constructs are created by seeding muscle progenitor cells (MPCs) onto a porcine bladder acellular matrix (BAM). The cellularized constructs are then preconditioned in a custom-designed, cyclical stretch bioreactor prior to implantation *in vivo*. In initial studies, Corona *et al* (2012) used the TEMR constructs in a nude mouse latissimus dorsi (LD) VML injury model and found functional recovery of 60-70% of contractile force within 2 months of implantation. In another study, Corona *et* al (2014) compared TEMR to BAM alone or no repair in an immunocompetent rat TA VML injury model. In some cases, positive responder TEMR groups saw functional recovery of over 60% of contractile force, while others underperformed compared to the controls. Passipieri *et al* (2019) also used TEMR constructs and found substantial tissue regeneration and functional recovery at 12 weeks post repair (≈90%), in a rat LD VML injury model. Most recently, Mintz *et al* (2020) used TEMR constructs as developed by Corona *et al* and again found positive and negative responders to the treatment, with the positive responder group showing highly significant functional recovery (87%). In addition to the TEMR technology developed by this group, other work has been conducted in the attempt to repair VML injury in a rat TA model. Greising *et al* (2017) used porcine UBM or decellularized small intestine submucosa but observed no difference at 10 weeks versus no repair. Kim *et al (2020)* used muscle plugs with varying degrees of alignment and found that plugs with an alignment of zero degrees showed significant improvement over controls or alignments of 45 and 90 degrees.

As an alternative to current musculoskeletal injury treatments, numerous additive biomanufacturing, or three-dimensional (3D) bioprinting, approaches have been explored in an effort to produce biological scaffolds and tissue mimetics with regenerative medicine applications (Murphy, De Coppi and Atala, 2020). Additive biomanufacturing offers the potential for on-demand fabrication of clinically relevant grafts capable of facilitating the restoration of functional native-like tissue, and thus, has the potential to greatly improve current treatment paradigms for musculoskeletal injuries. Cell-

based therapies offer the potential to improve the treatment of degenerative, inflammatory, and traumatic musculoskeletal disorders (O'Keefe *et al.*, 2020), and cellularized constructs may promote more rapid and complete tissue regeneration compared to the use of biomaterial scaffolds alone. Through the combination of novel scaffold design and cell-based therapies, the functional recovery of polytraumatic injuries could become realized in the near future.

1.3 References

Abrahamsson, C.K. *et al.* (2010) ‘Chondrogenesis and Mineralization During *In Vitro* Culture of Human Mesenchymal Stem Cells on Three-Dimensional Woven Scaffolds’, *Tissue Engineering Part A*, 16(12), pp. 3709–3718. Available at: https://doi.org/10.1089/ten.tea.2010.0190.

Achilli, M. and Mantovani, D. (2010) ‘Tailoring Mechanical Properties of Collagen-Based Scaffolds for Vascular Tissue Engineering: The Effects of pH, Temperature and Ionic Strength on Gelation’, *Polymers*, 2(4), pp. 664–680. Available at: https://doi.org/10.3390/polym2040664.

Akbari, M. *et al.* (2014) ‘Composite Living Fibers for Creating Tissue Constructs Using Textile Techniques’, *Advanced Functional Materials*, 24(26), pp. 4060–4067. Available at: https://doi.org/10.1002/adfm.201303655.

Ankrum, J.A., Ong, J.F. and Karp, J.M. (2014) ‘Mesenchymal stem cells: immune evasive, not immune privileged’, *Nature Biotechnology*, 32(3), pp. 252–260. Available at: https://doi.org/10.1038/nbt.2816.

Bliley, J.M. *et al.* (2015) ‘Ethylene Oxide Sterilization Preserves Bioactivity and Attenuates Burst Release of Encapsulated Glial Cell Line Derived Neurotrophic Factor from Tissue Engineered Nerve Guides For Long Gap Peripheral Nerve Repair’, *ACS Biomaterials Science & Engineering*, 1(7), pp. 504–512. Available at: https://doi.org/10.1021/ab5001518.

Bour, R.K. *et al.* (2020) ‘Bioprinting on sheet-based scaffolds applied to the creation of implantable tissue-engineered constructs with potentially diverse clinical applications: Tissue-Engineered Muscle Repair (TEMR) as a representative testbed’, *Connective Tissue Research*, 61(2), pp. 216–228. Available at: https://doi.org/10.1080/03008207.2019.1679800.

Butler, D.L., Juncosa, N. and Dressler, M.R. (2004) ‘Functional Efficacy of Tendon Repair Processes’, *Annual Review of Biomedical Engineering*, 6(1), pp. 303–329. Available at: https://doi.org/10.1146/annurev.bioeng.6.040803.140240.

Butler, D.L., Kay, M.D. and Stouffer, D.C. (1986) ‘Comparison of material properties in fascicle-bone units from human patellar tendon and knee ligaments’, *Journal of Biomechanics*, 19(6), pp. 425–432. Available at: https://doi.org/10.1016/0021-9290(86)90019-9.

Chandrashekar, N. *et al.* (2006) ‘Sex-based differences in the tensile properties of the human anterior cruciate ligament’, *Journal of Biomechanics*, 39(16), pp. 2943–2950. Available at: https://doi.org/10.1016/j.jbiomech.2005.10.031.

Christensen, K.W. *et al.* (2022) ‘Assembled Cell-Decorated Collagen (AC-DC) Fiber Bioprinted Implants with Musculoskeletal Tissue Properties Promote Functional Recovery in Volumetric Muscle Loss’, *Advanced Healthcare Materials*, 11(3), p. 2101357. Available at: https://doi.org/10.1002/adhm.202101357.

Cittadella Vigodarzere, G. and Mantero, S. (2014) ‘Skeletal muscle tissue engineering: strategies for volumetric constructs’, *Frontiers in Physiology*, 5. Available at: https://doi.org/10.3389/fphys.2014.00362.

Colvin, A.C. *et al.* (2012) ‘National Trends in Rotator Cuff Repair’, *JBJS*, 94(3), pp. 227–233. Available at: https://doi.org/10.2106/JBJS.J.00739.

Corona, B.T. *et al.* (2012) ‘Further Development of a Tissue Engineered Muscle Repair Construct In Vitro for Enhanced Functional Recovery Following Implantation In Vivo in a Murine Model of Volumetric Muscle Loss Injury’, *Tissue Engineering Part A*, 18(11–12), pp. 1213–1228. Available at: https://doi.org/10.1089/ten.tea.2011.0614.

Corona, B.T. *et al.* (2013) ‘Autologous minced muscle grafts: a tissue engineering therapy for the volumetric loss of skeletal muscle’, *American Journal of Physiology-Cell Physiology*, 305(7), pp. C761–C775. Available at: https://doi.org/10.1152/ajpcell.00189.2013.

Corona, B.T. *et al.* (2014) ‘Implantation of In Vitro Tissue Engineered Muscle Repair Constructs and Bladder Acellular Matrices Partially Restore In Vivo Skeletal Muscle Function in a Rat Model of Volumetric Muscle Loss Injury’, *Tissue Engineering Part A*, 20(3–4), pp. 705–715. Available at: https://doi.org/10.1089/ten.tea.2012.0761.

Corona, B.T. *et al.* (2015) ‘Volumetric muscle loss leads to permanent disability following extremity trauma’, *Journal of Rehabilitation Research and Development*, 52(7), pp. 785–792. Available at: https://doi.org/10.1682/JRRD.2014.07.0165.

Corona, B.T., Rivera, J.C. and Greising, S.M. (2018) ‘Inflammatory and Physiological Consequences of Debridement of Fibrous Tissue after Volumetric Muscle Loss Injury’, *Clinical and Translational Science*, 11(2), pp. 208–217. Available at: https://doi.org/10.1111/cts.12519.

Covey, D.C. (2002) ‘Blast and Fragment Injuries of the Musculoskeletal System’, *JBJS*, 84(7), pp. 1221–1234.

Dasgupta, A. *et al.* (2021) ‘Comprehensive collagen crosslinking comparison of microfluidic wet-extruded microfibers for bioactive surgical suture development’, *Acta Biomaterialia*, p. S1742706121002658. Available at: https://doi.org/10.1016/j.actbio.2021.04.028.

Dyer, S.E. *et al.* (2022) ‘Administration of particulate oxygen generators improves skeletal muscle contractile function after ischemia-reperfusion injury in the rat hindlimb’, *Journal of Applied Physiology*, 132(2), pp. 541–552. Available at: https://doi.org/10.1152/japplphysiol.00259.2021.

Eckenrode, B.J. *et al.* (2017) ‘Prevention and Management of Post-operative Complications Following ACL Reconstruction’, *Current Reviews in Musculoskeletal Medicine*, 10(3), pp. 315–321. Available at: https://doi.org/10.1007/s12178-017-9427-2.

Fadia, N.B. *et al.* (2020) ‘Long-gap peripheral nerve repair through sustained release of a neurotrophic factor in nonhuman primates’, *Science Translational Medicine*, 12(527), p. eaav7753. Available at: https://doi.org/10.1126/scitranslmed.aav7753.

Foolen, J. *et al.* (2018) ‘Tissue alignment enhances remodeling potential of tendon-derived cells - Lessons from a novel microtissue model of tendon scarring’, *Matrix Biology*, 65, pp. 14–29. Available at: https://doi.org/10.1016/j.matbio.2017.06.002.

Fu, S.Y. and Gordon, T. (1995) ‘Contributing factors to poor functional recovery after delayed nerve repair: prolonged denervation’, *Journal of Neuroscience*, 15(5), pp. 3886–3895. Available at: https://doi.org/10.1523/JNEUROSCI.15-05-03886.1995.

Fuoco, C. *et al.* (2016) ‘Matrix scaffolding for stem cell guidance toward skeletal muscle tissue engineering’, *Journal of Orthopaedic Surgery and Research*, 11(1), p. 86. Available at: https://doi.org/10.1186/s13018-016-0421-y.

Garg, K. *et al.* (2015a) ‘Volumetric muscle loss: persistent functional deficits beyond frank loss of tissue’, *Journal of Orthopaedic Research: Official Publication of the Orthopaedic Research Society*, 33(1), pp. 40–46. Available at: https://doi.org/10.1002/jor.22730.

Garg, K. *et al.* (2015b) ‘Volumetric muscle loss: Persistent functional deficits beyond frank loss of tissue’, *Journal of Orthopaedic Research*, 33(1), pp. 40–46. Available at: https://doi.org/10.1002/jor.22730.

Garg, K., Corona, B.T. and Walters, T.J. (2015) ‘Therapeutic strategies for preventing skeletal muscle fibrosis after injury’, *Frontiers in Pharmacology*, 6. Available at: https://www.frontiersin.org/articles/10.3389/fphar.2015.00087 (Accessed: 31 October 2022).

Gentleman, E. *et al.* (2003) ‘Mechanical characterization of collagen fibers and scaffolds for tissue engineering’, *Biomaterials*, 24(21), pp. 3805–3813. Available at: https://doi.org/10.1016/S0142-9612(03)00206-0.

Gentleman, E. *et al.* (2006) ‘Development of Ligament-Like Structural Organization and Properties in Cell-Seeded Collagen Scaffolds in vitro’, *Annals of Biomedical Engineering*, 34(5), pp. 726–736. Available at: https://doi.org/10.1007/s10439-005-9058-4.

Grasman, J.M. *et al.* (2015) ‘Biomimetic scaffolds for regeneration of volumetric muscle loss in skeletal muscle injuries’, *Acta Biomaterialia*, 25, pp. 2–15. Available at: https://doi.org/10.1016/j.actbio.2015.07.038.

Greising, S.M., Dearth, C.L. and Corona, B.T. (2016) ‘Regenerative and Rehabilitative Medicine: A Necessary Synergy for Functional Recovery from Volumetric Muscle Loss Injury’, *Cells Tissues Organs*, 202(3–4), pp. 237–249. Available at: https://doi.org/10.1159/000444673.

Grogan, B.F., Hsu, J.R. and Consortium, S.T.R. (2011a) ‘Volumetric Muscle Loss’, *JAAOS - Journal of the American Academy of Orthopaedic Surgeons*, 19, p. S35.

Grogan, B.F., Hsu, J.R. and Consortium, S.T.R. (2011b) ‘Volumetric Muscle Loss’, *JAAOS - Journal of the American Academy of Orthopaedic Surgeons*, 19, p. S35.

Han, H., Furst, E.M. and Kim, C. (2014) ‘Lagrangian analysis of consecutive images: Quantification of mixing processes in drops moving in a microchannel’, *Rheologica Acta*, 53(7), pp. 489–499. Available at: https://doi.org/10.1007/s00397-014-0769-z.

Herchenhan, A. *et al.* (2013) ‘In vitro tendon tissue development from human fibroblasts demonstrates collagen fibril diameter growth associated with a rise in mechanical strength’, *Developmental Dynamics*, 242(1), pp. 2–8. Available at: https://doi.org/10.1002/dvdy.23896.

Itoi, E. *et al.* (1995) ‘Tensile properties of the supraspinatus tendon’, *Journal of Orthopaedic Research*, 13(4), pp. 578–584. Available at: https://doi.org/10.1002/jor.1100130413.

Jang, K.-M. *et al.* (2015) ‘Efficacy and Safety of Human Umbilical Cord Blood–Derived Mesenchymal Stem Cells in Anterior Cruciate Ligament Reconstruction of a Rabbit Model: New Strategy to Enhance Tendon Graft Healing’, *Arthroscopy: The Journal of Arthroscopic & Related Surgery*, 31(8), pp. 1530–1539. Available at: https://doi.org/10.1016/j.arthro.2015.02.023.

Janssen, I. *et al.* (2000) ‘Skeletal muscle mass and distribution in 468 men and women aged 18–88 yr’, *Journal of Applied Physiology*, 89(1), pp. 81–88. Available at: https://doi.org/10.1152/jappl.2000.89.1.81.

Jiang, X. *et al.* (2020) ‘3D printing of multilayered scaffolds for rotator cuff tendon regeneration’, *Bioactive Materials*, 5(3), pp. 636–643. Available at: https://doi.org/10.1016/j.bioactmat.2020.04.017.

Juhas, M. and Bursac, N. (2013) ‘Engineering skeletal muscle repair’, *Current Opinion in Biotechnology*, 24(5), pp. 880–886. Available at: https://doi.org/10.1016/j.copbio.2013.04.013.

Juhas, M., Ye, J. and Bursac, N. (2016) ‘Design, evaluation, and application of engineered skeletal muscle’, *Methods*, 99, pp. 81–90. Available at: https://doi.org/10.1016/j.ymeth.2015.10.002.

Kaiser, N.J. *et al.* (2019) ‘Digital Design and Automated Fabrication of Bespoke Collagen Microfiber Scaffolds’, *Tissue Engineering Part C: Methods*, 25(11), pp. 687–700. Available at: https://doi.org/10.1089/ten.tec.2018.0379.

Kishore, V. *et al.* (2012) ‘TENOGENIC DIFFERENTIATION OF HUMAN MSCs INDUCED BY THE TOPOGRAPHY OF ELECTROCHEMICALLY ALIGNED COLLAGEN THREADS’, *Biomaterials*, 33(7), pp. 2137–2144. Available at: https://doi.org/10.1016/j.biomaterials.2011.11.066.

Kokai, L.E. *et al.* (2011) ‘Sustained Growth Factor Delivery Promotes Axonal Regeneration in Long Gap Peripheral Nerve Repair’, *Tissue Engineering Part A*, 17(9–10), pp. 1263–1275. Available at: https://doi.org/10.1089/ten.tea.2010.0507.

Kokai, L.E., Ghaznavi, A.M. and Marra, K.G. (2010) ‘Incorporation of double-walled microspheres into polymer nerve guides for the sustained delivery of glial cell line-derived neurotrophic factor’, *Biomaterials*, 31(8), pp. 2313–2322. Available at: https://doi.org/10.1016/j.biomaterials.2009.11.075.

Lee, S.Y. *et al.* (2017) ‘Therapeutic Mechanisms of Human Adipose-Derived Mesenchymal Stem Cells in a Rat Tendon Injury Model’, *The American Journal of Sports Medicine*, 45(6), pp. 1429–1439. Available at: https://doi.org/10.1177/0363546517689874.

Li, C. and Cui, W. (2021) ‘3D bioprinting of cell-laden constructs for regenerative medicine’, *Engineered Regeneration*, 2, pp. 195–205. Available at: https://doi.org/10.1016/j.engreg.2021.11.005.

Liberski, A.R. *et al.* (2011) ‘Organ Weaving: Woven Threads and Sheets As a Step Towards a New Strategy for Artificial Organ Development: Organ Weaving: Woven Threads and Sheets As a Step Towards …’, *Macromolecular Bioscience*, 11(11), pp. 1491–1498. Available at: https://doi.org/10.1002/mabi.201100086.

Liu, J. *et al.* (2018) ‘Current Methods for Skeletal Muscle Tissue Repair and Regeneration’, *BioMed Research International*, 2018, p. e1984879. Available at: https://doi.org/10.1155/2018/1984879.

Maghdouri-White, Y. *et al.* (2020) ‘Biomanufacturing organized collagen-based microfibers as a Tissue ENgineered Device (TEND) for tendon regeneration’, *Biomedical Materials* [Preprint]. Available at: https://doi.org/10.1088/1748-605X/abb875.

Mandrycky, C. *et al.* (2016) ‘3D bioprinting for engineering complex tissues’, *Biotechnology Advances*, 34(4), pp. 422–434. Available at: https://doi.org/10.1016/j.biotechadv.2015.12.011.

Mauck, R.L. *et al.* (2009) ‘Engineering on the Straight and Narrow: The Mechanics of Nanofibrous Assemblies for Fiber-Reinforced Tissue Regeneration’, *Tissue Engineering Part B: Reviews*, 15(2), pp. 171–193. Available at: https://doi.org/10.1089/ten.teb.2008.0652.

Merceron, T.K. *et al.* (2015) ‘A 3D bioprinted complex structure for engineering the muscle–tendon unit’, *Biofabrication*, 7(3), p. 035003. Available at: https://doi.org/10.1088/1758-5090/7/3/035003.

Mertens, J.P. *et al.* (2014) ‘Engineering muscle constructs for the creation of functional engineered musculoskeletal tissue’, *Regenerative Medicine*, 9(1), pp. 89–100. Available at: https://doi.org/10.2217/rme.13.81.

Mintz, E.L. *et al.* (2016) ‘Applications of In Vivo Functional Testing of the Rat Tibialis Anterior for Evaluating Tissue Engineered Skeletal Muscle Repair’, *Journal of Visualized Experiments : JoVE*, (116), p. 54487. Available at: https://doi.org/10.3791/54487.

Mintz, E.L. *et al.* (2020) ‘Long-Term Evaluation of Functional Outcomes Following Rat Volumetric Muscle Loss Injury and Repair’, *Tissue Engineering Part A*, 26(3–4), pp. 140–156. Available at: https://doi.org/10.1089/ten.tea.2019.0126.

Moimas, S. *et al.* (2013) ‘Effect of vascular endothelial growth factor gene therapy on post-traumatic peripheral nerve regeneration and denervation-related muscle atrophy’, *Gene Therapy*, 20(10), pp. 1014–1021. Available at: https://doi.org/10.1038/gt.2013.26.

Murphy, S.V. and Atala, A. (2014) '3D bioprinting of tissues and organs', *Nature Biotechnology*, 32(8), pp. 773–785. Available at: https://doi.org/10.1038/nbt.2958.

Murphy, S.V., De Coppi, P. and Atala, A. (2020) 'Opportunities and challenges of translational 3D bioprinting', *Nature Biomedical Engineering*, 4(4), pp. 370–380. Available at: https://doi.org/10.1038/s41551-019-0471-7.

Ngan, C. *et al.* (2017) 'Engineering skeletal muscle - from two to three dimensions', *Australian Institute for Innovative Materials - Papers*, pp. 1–6. Available at: https://doi.org/10.1002/term.2265.

Novakova, S.S. *et al.* (2017) 'Tissue-engineered tendon constructs for rotator cuff repair in sheep: ENGINEERED TENDON ROTATOR CUFF REPAIR', *Journal of Orthopaedic Research* [Preprint]. Available at: https://doi.org/10.1002/jor.23642.

Noyes, F. and Grood, E. (1976) 'The strength of the anterior cruciate ligament in humans and Rhesus monkeys':, *The Journal of Bone & Joint Surgery*, 58(8), pp. 1074–1082. Available at: https://doi.org/10.2106/00004623-197658080-00006.

Ober, T.J., Foresti, D. and Lewis, J.A. (2015) 'Active mixing of complex fluids at the microscale', *Proceedings of the National Academy of Sciences*, 112(40), pp. 12293–12298. Available at: https://doi.org/10.1073/pnas.1509224112.

O'Keefe, Regis J *et al.* (2020) 'American Society for Bone and Mineral Research-Orthopaedic Research Society Joint Task Force Report on Cell-Based Therapies', *Journal of Bone and Mineral Research*, 35(1), pp. 3–17. Available at: https://doi.org/10.1002/jbmr.3839.

Passipieri, J. a. *et al.* (2017) 'Keratin Hydrogel Enhances In Vivo Skeletal Muscle Function in a Rat Model of Volumetric Muscle Loss', *Tissue Engineering Part A*, 23(11–12), pp. 556–571. Available at: https://doi.org/10.1089/ten.tea.2016.0458.

Passipieri, J.A. *et al.* (2019) ‘In Silico and In Vivo Studies Detect Functional Repair Mechanisms in a Volumetric Muscle Loss Injury’, *Tissue Engineering Part A*, 25(17–18), pp. 1272–1288. Available at: https://doi.org/10.1089/ten.tea.2018.0280.

Passipieri, J.A. *et al.* (2021) ‘Adipose Stem Cells Enhance Nerve Regeneration and Muscle Function in a Peroneal Nerve Ablation Model’, *Tissue Engineering Part A*, 27(5–6), pp. 297–310. Available at: https://doi.org/10.1089/ten.tea.2018.0244.

Passipieri, J.A. and Christ, G.J. (2016) ‘The Potential of Combination Therapeutics for More Complete Repair of Volumetric Muscle Loss Injuries: The Role of Exogenous Growth Factors and/or Progenitor Cells in Implantable Skeletal Muscle Tissue Engineering Technologies’, *Cells Tissues Organs*, 202(3–4), pp. 202–213. Available at: https://doi.org/10.1159/000447323.

Pittenger, M.F. *et al.* (1999) ‘Multilineage Potential of Adult Human Mesenchymal Stem Cells’, *Science*, 284(5411), pp. 143–147. Available at: https://doi.org/10.1126/science.284.5411.143.

Puetzer, J.L. and Bonassar, L.J. (2016) ‘Physiologically Distributed Loading Patterns Drive the Formation of Zonally Organized Collagen Structures in Tissue-Engineered Meniscus’, *Tissue Engineering Part A*, 22(13–14), pp. 907–916. Available at: https://doi.org/10.1089/ten.tea.2015.0519.

Qazi, T.H. *et al.* (2015) ‘Biomaterials based strategies for skeletal muscle tissue engineering: Existing technologies and future trends’, *Biomaterials*, 53, pp. 502–521. Available at: https://doi.org/10.1016/j.biomaterials.2015.02.110.

Sahoo, S., Cho-Hong, J.G. and Siew-Lok, T. (2007) ‘Development of hybrid polymer scaffolds for potential applications in ligament and tendon tissue engineering’, *Biomedical Materials*, 2(3), pp. 169–173. Available at: https://doi.org/10.1088/1748-6041/2/3/001.

Seon, J.K., Song, E.K. and Park, S.J. (2006) ‘Osteoarthritis after anterior cruciate ligament reconstruction using a patellar tendon autograft’, *International Orthopaedics*, 30(2), pp. 94–98. Available at: https://doi.org/10.1007/s00264-005-0036-0.

Sheean, A.J., Dickens, J.F. and Provencher, M.T. (2021) ‘Extremity War Injury Symposium XV: Sports and Readiness Symposium Summary’, *The Journal of the American Academy of Orthopaedic Surgeons* [Preprint]. Available at: https://doi.org/10.5435/JAAOS-D-20-00930.

Shin, Y.K. *et al.* (2018) ‘Predictive Factors of Retear in Patients With Repaired Rotator Cuff Tear on Shoulder MRI’, *American Journal of Roentgenology*, 210(1), pp. 134–141. Available at: https://doi.org/10.2214/AJR.17.17915.

Smith, L.R. and Barton, E.R. (2014) ‘SMASH – semi-automatic muscle analysis using segmentation of histology: a MATLAB application’, *Skeletal Muscle*, 4(1), p. 21. Available at: https://doi.org/10.1186/2044-5040-4-21.

Tamayol, A. *et al.* (2013) ‘Fiber-based tissue engineering: Progress, challenges, and opportunities’, *Biotechnology Advances*, 31(5), pp. 669–687. Available at: https://doi.org/10.1016/j.biotechadv.2012.11.007.

Taylor, K.A. *et al.* (2013) ‘In vivo measurement of ACL length and relative strain during walking’, *Journal of Biomechanics*, 46(3), pp. 478–483. Available at: https://doi.org/10.1016/j.jbiomech.2012.10.031.

Turner, N.J. and Badylak, S.F. (2012) ‘Regeneration of skeletal muscle’, *Cell and Tissue Research*, 347(3), pp. 759–774. Available at: https://doi.org/10.1007/s00441-011-1185-7.

Walters, V.I., Kwansa, A.L. and Freeman, J.W. (2012) ‘Design and Analysis of Braid-Twist Collagen Scaffolds’, *Connective Tissue Research*, 53(3), pp. 255–266. Available at: https://doi.org/10.3109/03008207.2011.634532.

Wang, J.H.-C. *et al.* (2003) ‘Cell orientation determines the alignment of cell-produced collagenous matrix’, *Journal of Biomechanics*, 36(1), pp. 97–102. Available at: https://doi.org/10.1016/S0021-9290(02)00233-6.

Westman, A.M. *et al.* (2021) ‘Agent-based model provides insight into the mechanisms behind failed regeneration following volumetric muscle loss injury’, *PLOS Computational Biology*, 17(5), p. e1008937. Available at: https://doi.org/10.1371/journal.pcbi.1008937.

Wolf, M.T. *et al.* (2015) ‘Naturally derived and synthetic scaffolds for skeletal muscle reconstruction’, *Advanced Drug Delivery Reviews*, 84, pp. 208–221. Available at: https://doi.org/10.1016/j.addr.2014.08.011.

Wu, Y. *et al.* (2017) ‘Direct E-jet printing of three-dimensional fibrous scaffold for tendon tissue engineering: DIRECT E-JET PRINTING OF SCAFFOLD FOR TENDON TISSUE ENGINEERING’, *Journal of Biomedical Materials Research Part B: Applied Biomaterials*, 105(3), pp. 616–627. Available at: https://doi.org/10.1002/jbm.b.33580.

Zhang, J. *et al.* (2015) ‘The challenges and promises of allogeneic mesenchymal stem cells for use as a cell-based therapy’, *Stem Cell Research & Therapy*, 6(1), p. 234. Available at: https://doi.org/10.1186/s13287-015-0240-9.

Chapter 2: Development and evaluation of tissue engineering applications for repair of polytraumatic VML injuries

Some sections adapted from: Bour RK, Sharma PR, Turner JS, Hess WE, Mintz EL, Latvis CR, Shepherd BR, Presnell SC, McConnell MJ, Highley C, Peirce SM, Christ GJ. Bioprinting on sheet-based scaffolds applied to the creation of implantable tissue-engineered constructs with potentially diverse clinical applications. Connective tissue research. 2020;61(2):216–228.

2.1 Introduction

In vitro co-culture systems are an important tool for investigation of cellular interactions. Many strategies currently exist for co-culture evaluation, which may include 2D or 3D cultures and with cells either in direct or indirect contact. Recent studies involve the use of tunable, biomimetic hydrogels and other scaffold-based systems for studying co-culture. The inclusion of multiple cell types *in vitro* provides a better recapitulation of tissue features *in vivo*. Previous research has shown the ability of co-culture systems to produce more biologically relevant tissue mimetics than single cells alone [Paschos 2014]. While these *in vitro* studies provide valuable information, they are mostly targeted at identifying characteristics of cellular interactions and cell signaling and are not currently being investigated for potential in pre-clinical studies.

Because co-culture systems can create more biologically relevant tissue, it is therefore of interest to apply this knowledge to the application of cell-based therapeutics for tissue regeneration. More biologically relevant tissues have already been explored through introduction of technologies such as bioreactor conditioning *in vitro*. Bioreactor conditioning of muscle cells can create a more competent tissue with mature muscle fibers compared to typical static cultures. Cell-based therapeutics incorporating this technology have already shown significant improvement in functional recovery of muscle tissues (Corona *et al.*, 2014; Mintz *et al.*, 2020). Therefore, it is our belief that

further improving the quality of tissue *in vitro* prior to implantation will lead to greater functional recovery *in vivo*. *In vitro* co-culture systems can be used to this end by pre-conditioning cells towards a more mature and defined state prior to implantation *in vivo* in animal models.

In this regard, bioprinting is an important emerging technology in the tissue engineering field that may facilitate the need for co-culture methods scaled to use in pre-clinical studies. Bioprinting allows for highly reproducible and tunable methods of cell deposition in both 2D and 3D cultures(Bour *et al.*, 2020). Bioprinting may consist of inkjet, laser assisted, or extrusion methods. Extrusion bioprinting is the most used method currently and can utilize bioinks from a variety of synthetic and naturally derived ECM material. Some examples of bases for bioinks include hyaluronic acid, collagen, poly(vinyl alcohol) (PVA) and many others. Bioprinted muscle tissues have been shown to improve cellular alignment of muscle fibers grown in vitro (Li and Cui, 2021). Increasing cellular alignment on sheet-based therapeutics in combination with mechanical stimulation *in vitro* has been shown to produce more biologically relevant tissues and improve functional outcomes when implanted into VML injury models *in vivo* (Corona *et al.*, 2014).

In this chapter we will focus on the potential for biomanufacturing tissue engineered constructs capable of restoring form and function in polytraumatic injuries. To this end, we have modified the TEMR constructs highlighted in chapter 1 using bioprinting technology to incorporate co-culture methods aiming to produce innervated muscle tissue constructs ready for implantation *in vivo*. First, co-culture methods for nerve and muscle cells were explored to create innervated muscle tissue *in vitro*. Bioprinting was conducted using hyaluronic acid (HA) based bioinks to print both nerve progenitor cells (NPCs) and muscle progenitor cells (MPCs). Following success developing co-culture methods, next steps involved the use of formerly established sheet-based cellularized therapeutics.

As discussed in chapter 1, Tissue engineered muscle repair (TEMR) constructs have been shown to improve functional recovery of VML injuries. These therapeutics are based on porcine

bladder acellular matrix scaffolds, which are then seeded with muscle progenitor cells and subjected to bioreactor conditioning to improve cellular alignment. Stretching in the bioreactor helps to provide mechanical cues to MPCs that aid in differentiation into more mature muscle fibers and have already been shown to improve injury repair over the use of bladder acellular matrix alone. The use of TEMR technology in functional muscle recovery is well established, but the use of these scaffolds as a basis for muscle and neuronal co-culture had not yet been explored and was the aim of this chapter. By introducing neural progenitor cells onto the cell culture platform, an innervated muscle construct was formed, which was named the nTEMR.

Materials that show success in culturing multiple types of cells as well as the potential for regenerative therapy could be biomanufactured to face the issue of polytraumatic injuries. Customizable, and tailored therapeutics to repair the interface of tissues or multiple tissues at the same time are key to the next step of regenerative therapeutics. Here, we utilized bioprinting, co-culture methods, and sheet-based scaffolds to produce biologically relevant tissues from nerve and muscle cells. The ultimate goal would be to use these strategies in polytraumatic VML injury repair.

2.2 Materials and Methods

Cell Culture and Collection

Muscle progenitor cells (MPCs) were isolated as previously described (Corona *et al.*, 2014). The tibialis anterior (TA) and soleus muscles of 4-week-old female Lewis rats (Charles River Laboratories, Wilmington, MA) were excised, sterilized in iodine, and rinsed with PBS (Hyclone). Muscles were minced to create a homogenous cell slurry, and then incubated for 2 h at 37C in 0.2% collagenase (Worthington Biochemicals, Lakewood, NJ) in DMEM. The homogenous muscle slurry was then pre-plated onto 10-cm collagen-coated tissue culture dishes (Corning, Corning, NY) at 37C in myogenic medium containing DMEM high glucose with 20% FBS, 10% horse serum (Gibco by Life

Technologies); 1% chick embryo extract (Accurate, Westbury, NY), and 1% AA. After 24 h, the cell suspension was transferred to 15-cm Matrigel-coated (1:50; BD Biosciences, Franklin Lakes, NJ) tissue culture dishes. Cells were passaged at 70–90% confluence and further cultured in proliferation media containing DMEM low glucose with 15% FBS and 1% AA. All cells were cultured in incubators at 37° C and 5% CO^2. Human MPCs were collected through biopsy punch and gifted from the orthopedic department at the University of Virginia Hospital. Human NPCs were gifted by the McConnell lab at UVA. During co-culture experiments, human NPCs and neurons were differentiated in the same media as the rat MPCs, but neuronal differentiation media was used prior to co-culture.

Bioprinting and Co-culture

When bioprinting, cell suspensions and Hyaluronic Acid (HA) were combined to form a 2wt% HA bioink, which could then be loaded into sterile syringe tubes from Cellink. MPCs were loaded at a density of 1-5 million/ml, while NPCs were loaded at a density of 0.2-1 million/mL. A Cellink Inkredible bioprinter was used to extrude 3D hydrogels into a predefined geometry based on the scaffold shape and size. Bioprinting was done directly into a dish for 2D culture environments or were bioprinted onto bladder acellular matrix (BAM) scaffolds for 3D culture. Co-culture was conducted using human muscle differentiation media with only the addition of GDNF (Glial derived neurotrophic factor) at a concentration of 0.1 ng/ml. Culture conditions were kept at 37° C and 5% CO^2.

nTEMR Preparation

The TEMR construct was prepared as previously described (Corona *et al.*, 2012) and will be called nTEMR in this publication due to the addition of the neural component. Briefly, sterilized bladder acellular matrix scaffolds were seeded with 2 milliliters of HA bioink containing MPCs and NPCs on one side, and 24h later the scaffold and mold were flipped and 2 milliliters of HA bioink was

seeded on the alternate side. After 3 days in seeding media, a media change was performed to immerse the scaffolds in differentiation media (DMEM F12, 2% horse serum, 1% AA, 0.1% GDNF) for an additional 7 days. After ten days in static culture, the cell-seeded scaffolds were placed in a bioreactor system. The bioreactor conditions the nTEMR with cyclic stretching to ~10% strain three times per minute for the first 5 minutes of every hour over a 5-day period. The nTEMR scaffolds were immersed in seeding media for the duration of their time in the bioreactor, and the bioreactor was placed in an incubator that was continuously aerated with 95% air-5% carbon dioxide at 37°C.

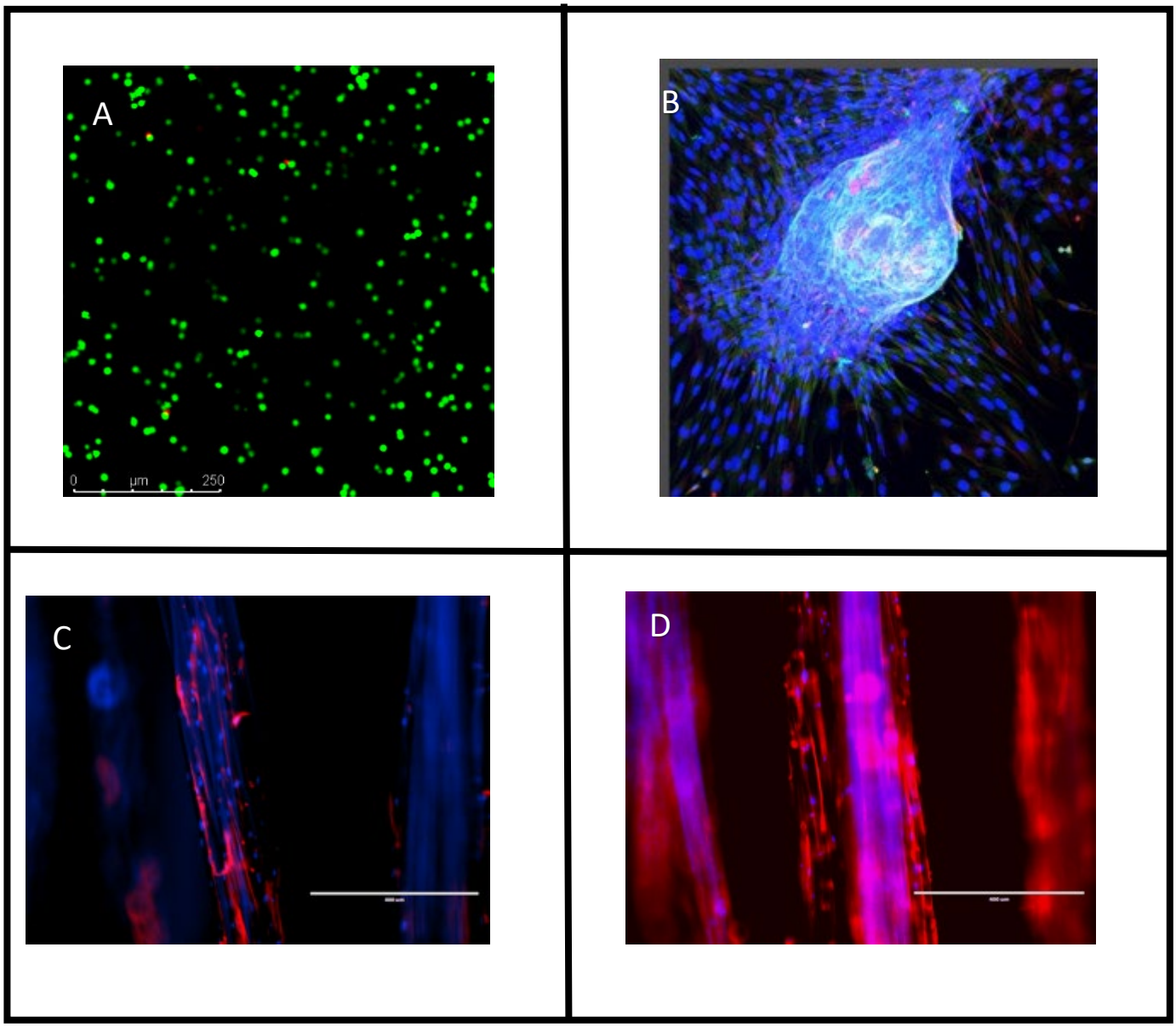

Figure 2-1. Hyaluronic Acid Hydrogel based printing. (A) Live-Dead Assay showing high viability when printing MPCs using HA hydrogel in a CellLink Inkredible Bioprinter. (B) Combination of MPCs and NPCs printed on a dish and kept in culture for 14 days, BIII (Beta III) Tubulin (green), Desmin (red), nuclei (blue). (C+D) MPCs bioprinted onto electrospun collagen microfiber scaffolds (Embody, LLC) and kept in culture for 9 days. Scale bar for (A) is 250 μm and scale bar for (C+D) are 1000 μm.

(2.3) Results

Cell Viability Following Bioprinting

Cells were printed in HA bioink using the Celllink Inkredible bioprinter onto a variety of scaffolds and under a variety of culture conditions in the pursuit of determining appropriate co-culture conditions for neural and muscle progenitor cells. Figure 1 demonstrates some of the early success in bioprinting a variety of cell types using this setup. Cell viability was very high in bioprinting, either on 2D or 3D surfaces (Fig. 1a). Cells were successfully cultured in 2D culture in a disposable cell culture dish as well as 3D cultures on both bladder acellular matrix and collagen microfiber scaffolds. When seeding muscle cells on microfiber collagen scaffolds alignment along the fibers was achieved (Fig. 1c,d). The collagen microfiber scaffolds showed exceptional attachment and alignment capabilities for muscle progenitor cells as well as tenocytes and these scaffolds are further examined in future chapters. Hyaluronic Acid bioinks were a suitable delivery vehicle for numerous cell types and a variety of culture conditions (Table 1). Table 1 contains a summary of experiments performed in tuning the hydrogel and cell densities, as well as experimentation with a wide range of cell types. The cell types successfully printed with high viability using these methods were rat MPCs, human MPCs,

human NPCs, human neurons, and tenocytes. Viability for all these methods exceeded 90% (results not shown).

Cell Suspension Material	Cell Type(s)	Scaffolding	Cell Seeding Method and density
Cellink START bioink	C2C12s	Dish, BAM	Bioprinted, 1 mil/mL
1.5wt% HA Hydrogel, 2wt% HA Hydrogel, 2.5wt% HA hydrogel	Rat MPCs	Dish, BAM, Wet spun collagen	Bioprinted, 1-5 mil/mL
2wt% HA Hydrogel	Rat MPCs + Human NPCs	Dish, BAM	Bioprinted, 1-5 mil/mL MPCs and 0.2-1 mil/mL NPCs
2wt% HA Hydrogel	Human MPCs + Human NPCs	Dish, BAM	Bioprinted,1-2 mil/mL MPCs and 0.2-1 mil/mL NPCs
2wt% HA Hydrogel	Human Neurons + hMPCs	nTEMR	Bioprinted, Neurons 0.2-1 mil/mL
2wt% HA Hydrogel	Tenocytes	Wet spun collagen	Bioprinted, not documented

Table 2-1. Bioprinting approaches using Cellink Inkredible bioprinter. Multiple cell types, densities, and suspension materials were used all showing high viability.

Co-Culture of Muscle and Neural Progenitors

Neural and muscle progenitor cells were kept in culture for a minimum of 14 days to allow time for nerve differentiation. Cells maintained high viability and started to form higher order cell structures when kept in co-culture for an extended period (Fig. 1b). The addition of GDNF to human muscle differentiation media was deemed sufficient to induce neural differentiation. Beta-III tubulin staining confirmed the presence of dendrites in 2D culture. Alpha bungarotoxin staining did not show the presence of neuromuscular junctions (NMJs) at this time.

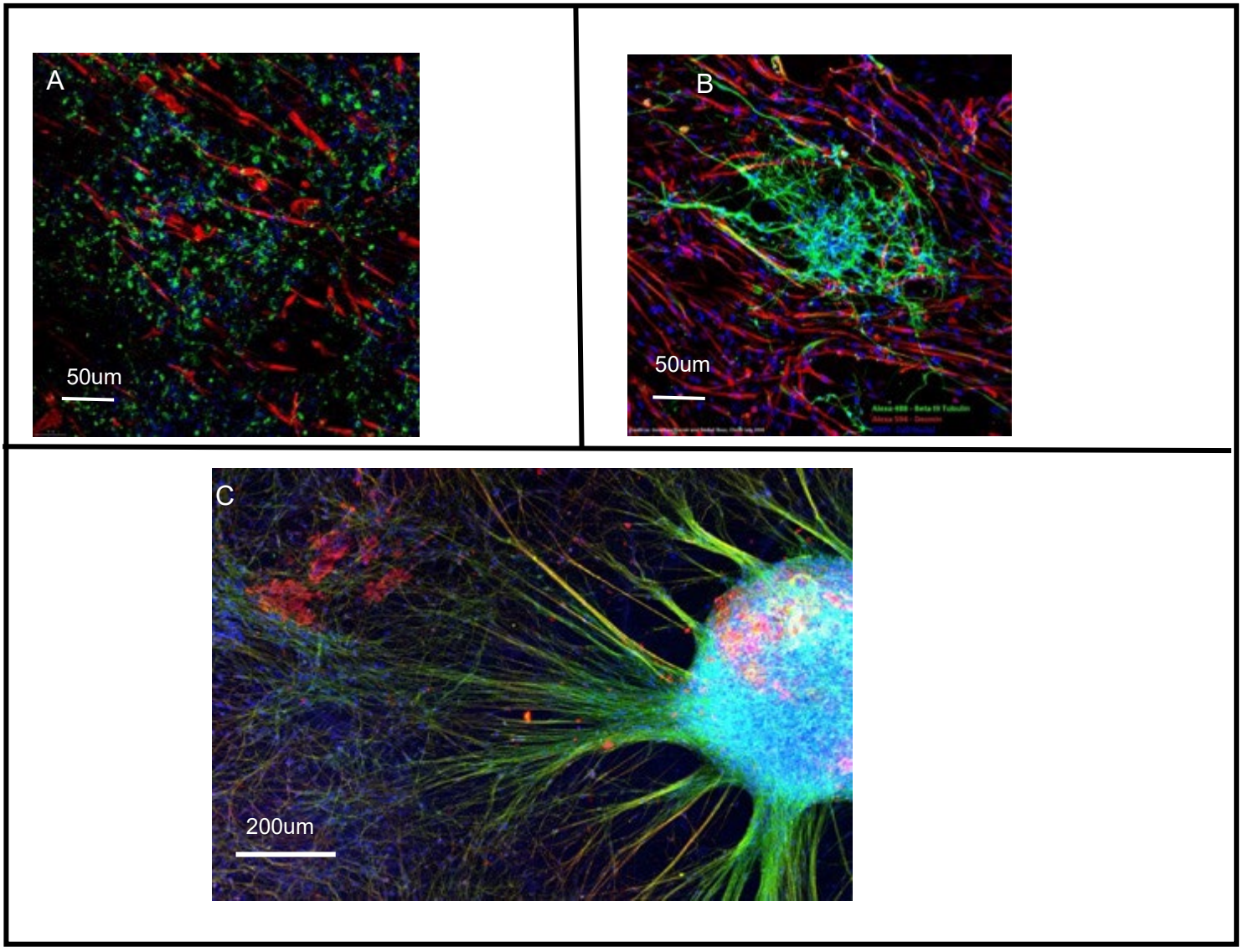

Figure 2-2. Neuron and Muscle Progenitor Co-Culture Experiments. BIII Tubulin staining neural tissue (green), Desmin staining muscle tissue (red), and DAPI staining cell nuclei (blue) (A) hNPCs + hMPCs bioprinted onto BAM and co-cultured for 14 days. (B) Neurons (cultured for 3 weeks) bioprinted with hMPCs onto BAM and further cultured for 13 days. (C) nTEMR, bioprinted human neurons (3 weeks old) and hMPCs bioreactor conditioned for 5 days and further maturation for 7 days.

nTEMR fabrication

Neuronal and muscle co-culture was examined both in 2D as well as on the BAM scaffolds with the goal of producing nTEMRs, an innervated muscle tissue scaffold with muscular regenerative capacity. Initial results included the printing of human NPCs and human MPCs in conjunction on the BAM (Fig. 2a). However, even after sufficient time in culture, the NPCs were not showing dendrites or maturation into neuron like cells. Furthermore, α-bungarotoxin staining for neuromuscular junction acetylcholine receptors was inconclusive. This led to attempting to print pre-matured neurons with MPCs despite being concerned with risk for damage to neurons during printing. In figure 2b, the prints shown consisted of human muscle progenitor cells printed first at Day 0 at a density of 3.7 × 105 hMPCs/cm^2. After 24 h, the human neurons were printed at a density of 3 × 10^4 neurons/cm^2. These samples were imaged after 13 days in culture. Initial studies showed success (Fig. 2b) where not only did neurons survive the printing process but seemed to form dendritic extensions toward the forming muscle fibers. The α-bungarotoxin staining remained inconclusive, but this method was chosen to move forward for production of nTEMR constructs, where the printed cell matrix was bioreactor conditioned for a period of 5 days. The results of this preliminary experiment are shown (Fig. 2c). The resulting nTEMR was unexpected as the neurons seemed overly abundant (BIII tubulin staining in green) and

the muscle tissue was not as robust as anticipated (desmin staining in red). However, the presence of both cell types was encouraging, and the maturity and health of the neurons was apparent.

(2.4) Conclusions and Future Directions

In this chapter we have explored the potential for co-culture and bioprinting techniques in the pursuit of cellularized therapeutics for polytraumatic injury regeneration. Muscle and neuronal cells cultured together may provide a more robust, innervated tissue *in vitro,* leading to better functional outcomes when used as a cellularized therapeutic. Bioprinting allows for a controlled, tunable, and repeatable process to ensure the long-term efficacy and scalability of fabricated constructs. Perhaps the most important finding is that the human neurons bioprinted in co-culture with human MPCs in this work were shown to extend presumptive branched dendrites to co-localized MPCs, consistent with expected neuron activity, and moreover, suggestive of potential interaction directly with muscle cells. In that regard, nTEMR fabrication showed success in preserving muscle and nerve cells as higher order structures. With further experimentation and analysis, this could prove to be a potentially valuable implantable regenerative construct for repair of nerve and muscle injuries.

In summary, while this portion of work showed promise, there were issues that could be addressed in future work. As noted in the previous sections, the nTEMR fabrication had some setbacks and did not produce a fully competent innervated muscle tissue as expected. The muscle fibers were small and did not show a particularly mature morphology despite developing neurons on the nTEMR. This was likely caused by an early overgrowth of neurons leading to less space for growth of the muscle fibers. It is our hypothesis that these challenges may be overcome by making adjustment to cell densities or adjusting the timing that printed cells are introduced to the BAM matrix. Specifically, in future studies, I would like to attempt to reduce the density of neurons from roughly 20% of the quantity of MPCs to as little as 5%. I would also give the muscle progenitor cells more time to proliferate on the BAM surface prior to introduction of the neurons, for a minimum of 5 days.

While the co-culture step is pertinent to the outcome, cell growth *in vitro* must be delicately balanced. In conclusion, we have further developed an existing sheet-based cellularized therapeutic in the way of the nTEMR to incorporate multiple cell types utilizing bioprinting technology and HA bioinks as a delivery method. This construct still needs further design considerations to form the most biologically relevant tissue possible but is a step towards an implantable therapeutic targeting reinnervation of muscle tissue in a VML injury. I believe with enough time and funding the fabrication of an nTEMR capable of significantly improving functional recovery in a VML injury model is possible.

2.5 References

Bour, R.K. *et al.* (2020) 'Bioprinting on sheet-based scaffolds applied to the creation of implantable tissue-engineered constructs with potentially diverse clinical applications: Tissue-Engineered Muscle Repair (TEMR) as a representative testbed', *Connective Tissue Research*, 61(2), pp. 216–228. Available at: https://doi.org/10.1080/03008207.2019.1679800.

Corona, B.T. *et al.* (2012) 'Further Development of a Tissue Engineered Muscle Repair Construct In Vitro for Enhanced Functional Recovery Following Implantation In Vivo in a Murine Model of Volumetric Muscle Loss Injury', *Tissue Engineering Part A*, 18(11–12), pp. 1213–1228. Available at: https://doi.org/10.1089/ten.tea.2011.0614.

Corona, B.T. *et al.* (2013) 'Autologous minced muscle grafts: a tissue engineering therapy for the volumetric loss of skeletal muscle', *American Journal of Physiology-Cell Physiology*, 305(7), pp. C761–C775. Available at: https://doi.org/10.1152/ajpcell.00189.2013.

Corona, B.T. *et al.* (2014) ‘Implantation of In Vitro Tissue Engineered Muscle Repair Constructs and Bladder Acellular Matrices Partially Restore In Vivo Skeletal Muscle Function in a Rat Model of Volumetric Muscle Loss Injury’, *Tissue Engineering Part A*, 20(3–4), pp. 705–715. Available at: https://doi.org/10.1089/ten.tea.2012.0761.

Li, C. and Cui, W. (2021) ‘3D bioprinting of cell-laden constructs for regenerative medicine’, *Engineered Regeneration*, 2, pp. 195–205. Available at: https://doi.org/10.1016/j.engreg.2021.11.005.

Liu, J. *et al.* (2018) ‘Current Methods for Skeletal Muscle Tissue Repair and Regeneration’, *BioMed Research International*, 2018, p. e1984879. Available at: https://doi.org/10.1155/2018/1984879.

Mintz, E.L. *et al.* (2020) ‘Long-Term Evaluation of Functional Outcomes Following Rat Volumetric Muscle Loss Injury and Repair’, *Tissue Engineering Part A*, 26(3–4), pp. 140–156. Available at: https://doi.org/10.1089/ten.tea.2019.0126.

Paschos, N.K. *et al.* (2015) ‘Advances in tissue engineering through stem cell-based co-culture’, *Journal of Tissue Engineering and Regenerative Medicine*, 9(5), pp. 488–503. Available at: https://doi.org/10.1002/term.1870.

Passipieri, J.A. and Christ, G.J. (2016) ‘The Potential of Combination Therapeutics for More Complete Repair of Volumetric Muscle Loss Injuries: The Role of Exogenous Growth Factors and/or Progenitor Cells in Implantable Skeletal Muscle Tissue Engineering Technologies’, *Cells Tissues Organs*, 202(3–4), pp. 202–213. Available at: https://doi.org/10.1159/000447323.

Chapter 3: Assembled Cell Decorated Collagen (AC-DC) Fiber Bioprinted Implants with Musculoskeletal Tissue Properties Promote Functional Recovery in Volumetric Muscle Loss

The following chapter has been published in Advanced Healthcare Materials in 2021. A preface and conclusion have been added for this work to place it in the greater context of the overall work of this dissertation but has otherwise been included exactly as published. The work submitted was done in collaboration with Embody, LLC out of Norfolk, VA. Special thanks to Kyle Christensen and Michael Francis for their collaboration and contributions.

(3.1) Preface

In order to further examine the potential for polytraumatic injury therapeutics we collaborated with partners at Embody, LLC interested in utilizing existing technologies, a microfiber collagen scaffold, for tendon repair to transition to skeletal muscle and polytraumatic injuries. We believed we could set the ground work for future VML and myotendinous junction (MTJ) polytrauma injuries. This would be highly relevant in sports injuries as well as with combat fighters. To show the potential for a complex polytraumatic therapeutic, it was necessary to show the ability for their scaffold to be utilized in muscle injury models. As the scaffolds were originally designed for tendon, the tensile properties were significantly higher than would be found in native muscle tissues. We worked to tune the properties of their microfiber collagen scaffolds in order to fit a more acceptable range for muscle. They developed a novel biofabrication method to directly seed cells onto their microfiber scaffolds through an extrusion printing process. The resulting cellularized constructs were dubbed assembled cell decorated collagen (AC-DC) scaffolds and after initial characterization, *in vivo* work began at the University of Virginia to show whether the AC-DC scaffolds could provide functional recovery in a rat TA VML injury model. The following chapter is the result of that work.

(3.2)

Title: Assembled Cell-Decorated Collagen (AC-DC) fiber bioprinted implants with musculoskeletal tissue properties promote functional recovery in volumetric muscle loss

Authors: Kyle W. Christensen[1†], Jonathan Turner[2†], Kelly Coughenour[1], Yas Maghdouri-White[1], Anna A. Bulysheva[3], Olivia Sergeant[2], Michael Rariden[2], Alessia Randazzo[2], Andrew J. Sheean[4], George J. Christ[2‡*], Michael P. Francis[1‡*]

Affiliations:

[1]Embody, Inc.; Norfolk, Virginia, USA.

[2]Department of Biomedical Engineering and Orthopaedic Surgery, University of Virginia; Charlottesville, Virginia, USA.

[3]Depeartment of Electrical and Computer Engineering, Old Dominion University, Norfolk, VA, USA

[4] Department of Orthopaedic Surgery, San Antonio Military Medical Center, USAF 59th MDW, San Antonio, TX, USA

† These authors contributed equally to this work.

‡ Senior authors.

* Corresponding author. Email: mpf3b@virginia.edu

One Sentence Summary: Bioprinted collagen microfiber-based implants mimic musculoskeletal tissue properties in vitro and promote functional recovery in vivo.

Abstract: Musculoskeletal tissue injuries, including volumetric muscle loss (VML), are commonplace and often lead to permanent disability and deformation. We developed an advanced biomanufacturing platform producing cellularized collagen microfiber implants to facilitate functional repair and regeneration of musculoskeletal soft tissues. This Assembled Cell-Decorated Collagen (AC-DC) bioprinting process rapidly and reproducibly forms 3D implants using clinically relevant cells and strong, microfluidic extruded collagen fibers. Quantitative analysis showed that the directionality and distribution of cells throughout AC-DC implants mimic the cellular properties of native musculoskeletal tissue. AC-DC bioprinted implants further approximate or exceed the strength and stiffness of human musculoskeletal tissue and exceeded the properties of commonplace collagen hydrogels by orders of magnitude. The regenerative potential of AC-DC implants was also assessed in vivo in a rodent VML model. A critically sized muscle injury in the hindlimb was created and repaired, and limb torque generation potential was measured over 12 weeks. Both acellular and cellular implants were found to promote functional recovery compared to the unrepaired group, with AC-DC implants containing therapeutic muscle progenitor cells promoting the highest degree of recovery. Histological analysis and automated image processing of explanted muscle cross-sections revealed increased total muscle fiber count, median muscle fiber size, and increased cellularization for injuries repaired with cellularized implants. These studies introduce the tremendous potential of an advanced bioprinting method for generating tissue analogs with near-native biological and biomechanical properties with the potential to repair numerous challenging musculoskeletal injuries.

Main Text:

INTRODUCTION

Musculoskeletal tissue injuries are exceptionally commonplace in athletes, military, civilians, men, and women, from young to old, with over 30 million injuries reported annually in the United States alone (Butler, Juncosa and Dressler, 2004). For warfighters, extremity injuries account for up to 70% of trauma cases in theater (Covey, 2002). These injuries, including the damage and rupture of ligaments and tendons, tears at the myotendinous junction (MTJ), and volumetric muscle loss (VML) have been observed among military service members and civilians alike as sequelae of high energy trauma and recreational activity. These traumatic injuries often require surgical intervention as they exceed the body's self-repair capabilities and can significantly delay or entirely prevent a return to regular activity. Musculoskeletal injuries often require surgery, with as many as 250,000 repairs of the rotator cuff (Colvin et al., 2012) and 200,000 reconstructions of the anterior cruciate ligament (ACL) (Eckenrode et al., 2017) performed annually. As the most abundant tissue in the human body, comprising ~40% of total body mass (Janssen et al., 2000), skeletal muscle damage also frequently occurs, with as many as 55% of sport injuries involving damage at the myofiber level (Liu et al., 2018b). While muscle has a high regenerative capacity for relatively minor injuries, natural repair mechanisms are overwhelmed in cases of VML and lead to chronic functional deficits (Turner and Badylak, 2012; Corona et al., 2015; Garg et al., 2015a; Grasman et al., 2015).

Unfortunately, the effectiveness and long-term outcomes of current traumatic musculoskeletal soft tissue treatment options, particularly with severe muscle involvement, are often limited (Mintz et al., 2020b). Rotator cuff repair, for example, has been reported with re-injury rates greater than 50% (Shin et al., 2018), can have coincident muscle damage, and often leads to permanent stiffness and limited range of motion. Autografting, can lead to loss of function and morbidity at the donor site

(Seon, Song and Park, 2006b), and cadaveric grafts can be subject to complications due to tissue availability and immunoreactivity. Treatment options for VML are currently severely limited and include autologous free muscle flap transfer (Grogan, Hsu and Consortium, 2011a; Garg et al., 2015a), muscle transposition (Corona et al., 2015; Garg et al., 2015a), or amputation and power bracing (Grogan, Hsu and Consortium, 2011a). Again, donor site morbidity, when tissue is available for harvest, and the need for a uniquely skilled surgical team decrease positive patient outcomes and complicate VML treatment (Grogan, Hsu and Consortium, 2011a).

Numerous additive biomanufacturing, or three-dimensional (3D) bioprinting, approaches have been explored to produce biological implants and tissue mimetics with regenerative potential (Murphy and Atala, 2014; Murphy, De Coppi and Atala, 2020b). Toward addressing VML in particular, several tissue engineering approaches have been investigated to restore function to injured muscle (Juhas and Bursac, 2013; Cittadella Vigodarzere and Mantero, 2014; Mertens et al., 2014; Qazi et al., 2015; Wolf et al., 2015; Fuoco et al., 2016; Juhas, Ye and Bursac, 2016; Ngan et al., 2017). Additive biomanufacturing offers the potential for on-demand creation of clinically relevant implants capable of facilitating the restoration of functional native-like tissue. Thus, it has the potential to improve current treatment paradigms for musculoskeletal injuries significantly (Sheean, Dickens and Provencher, 2021). A biomimicry approach is often favored, where recreating the biochemical, morphological, and functional properties of targeted tissue is paramount to the therapeutic utility of manufactured implants (Murphy and Atala, 2014). In addition to mimicking the structural and material properties of native tissue, therapeutic cells are often included as key components of implants. Cell-based treatments offer the potential to improve the treatment of degenerative, inflammatory, and traumatic musculoskeletal disorders (Regis J. O'Keefe et al., 2020), and cellularized constructs may promote more rapid and complete tissue regeneration compared to the use of biomaterial implants alone.

However, to date, biomanufacturing approaches incorporating cells are often unable to adequately recreate fundamental properties of native tissue, limiting their use in a clinical setting. For example, soft hydrogels are the primary structural component used in typical bioprinting approaches (Mandrycky et al., 2016). Yet, they fail to match the mechanical properties of native musculoskeletal tissues by orders of magnitude (Noyes and Grood, 1976; Butler, Kay and Stouffer, 1986; Itoi et al., 1995). In efforts to improve the strength of hydrogel-based or even cell or ECM-only constructs, bioreactors and extended lengths of in vitro culture have been used to facilitate cellular remodeling and self-assembly (Herchenhan et al., 2013; Puetzer and Bonassar, 2016; Novakova et al., 2017). While this has led to marked improvements in strength and histological likeness to native tissue, the approach is costly, may have limited scalability commercially, and the produced implants ultimately still fail to match the mechanical properties of native tissues. Specialized hybrid bioprinting approaches have been developed that incorporate thermoplastic polymers and hydrogels to improve the mechanical properties of printed parts with a modest increase in biological activity (Merceron et al., 2015; Jiang et al., 2020). However, composite implants' mechanical and biological properties may still differ significantly. Further, synthetic materials often elicit a chronic inflammatory response and limit tissue remodeling and regeneration in vivo.

As an alternative to traditional 3D bioprinting, various fiber-based biomanufacturing approaches have been explored (Tamayol et al., 2013). These approaches build on the well-established clinical use of textiles and textile manufacturing processes, with additional means to seed scaffolds with cells after fabrication. Of particular importance for musculoskeletal tissue repair, synthetic (Sahoo, Cho-Hong and Siew-Lok, 2007; Abrahamsson et al., 2010) and natural biomaterial fibers (Gentleman et al., 2003, 2006; Walters, Kwansa and Freeman, 2012; Kaiser et al., 2019) may offer mechanical properties approximating native tissue (Gentleman et al., 2006; Walters, Kwansa and Freeman, 2012). Fibrous biomaterial scaffolds have been directly produced by wet-spinning (Kaiser et al., 2019; Dasgupta et al., 2021), electrospinning (Mauck et al., 2009; Maghdouri-White et al., 2020), and direct

writing (Wu et al., 2017), in which fiber production by solvent evaporation, polymerization within a solution bath, or temperature-based recrystallization, respectively, are integral aspects of the scaffold fabrication process. Alternatively, fibers can be produced as a feedstock for secondary assembly processes (Tamayol et al., 2013) by wet spinning, microfluidic spinning, biospinning, interface complexation, or melt spinning before being assembled into designed geometries as biotextiles by weaving (Abrahamsson et al., 2010), knitting (Sahoo, Cho-Hong and Siew-Lok, 2007), braiding (Walters, Kwansa and Freeman, 2012), manual assembly (Gentleman et al., 2006) and other approaches (47-55). In addition, across varying fabrication approaches, scaffolds have been seeded with cells after fabrication by manual pipetting, casting, and perfusion-based cell seeding, among other techniques (Tamayol et al., 2013).

The assembly of biomaterial fibers into cellularized 3D geometries has relied almost exclusively on complex manual assembly by weaving, knitting, braiding, or winding (Tamayol et al., 2013). These approaches offer severely limited reproducibility and scalability, both critical concerns for transitioning biomanufacturing processes and produced implants toward commercial scale and clinical use (Murphy, De Coppi and Atala, 2020b). More automated and well-characterized fiber-based approaches, such as electrospinning, have seen success clinically. However, these scaffolds typically still fail to match native tissue biological or mechanical properties and commonly require cytotoxic processing conditions during manufacturing, precluding the controlled use of therapeutic cells in-process. Post-fabrication manual cell seeding has been used to cellularize such implants, but seeding processes typically lack precision, control, feedback, are subject to human variability, and may depend on the micro- and macro-scale scaffold geometry. Controlled cell seeding remains a significant challenge for scaffolds with complex geometries, high thicknesses, low porosity, and especially for producing scaffolds with designed and controllable cellularity throughout. Approaches that coat natural and synthetic threads with cell-laden hydrogels have been developed to avoid the need for manual cell seeding but again require a complex manual assembly, yet with limited control and reproducibility

to form 3D structures (Liberski et al., 2011; Akbari et al., 2014). Due to the inherent variability of manual assembly and cell-seeding processes, the development of automated, controlled, and consistent biomanufacturing processes is critical for producing clinically relevant cellularized implants.

In this study, a non-traditional bioprinting approach that controls for scalable, high output, and high print-fidelity is developed, where clinically relevant cells are positioned controllably along clinically relevant, high strength collagen fibers to biomanufacture musculoskeletal tissue analogs for restoring form and function to injured tissues. Human mesenchymal stem cells (hMSCs) or rat muscle progenitor cells (MPCs) are bioprinted to create an engineered implant that may be valuable for a diverse array of indications including, tendon or muscle regeneration. Mesenchymal stem cells offer excellent potential for augmenting musculoskeletal tissue repair and regeneration due to their immune-evasive properties (Ankrum, Ong and Karp, 2014; Zhang et al., 2015), therapeutic effects (Jang et al., 2015; Zhang et al., 2015; Lee et al., 2017), multilineage differentiation potential (Pittenger et al., 1999), and availability as a commercial clinically relevant cell type. Similarly, MPCs have shown marked therapeutic effects in facilitating functional recovery in volumetric muscle loss injuries in validated animal models (Passipieri et al., 2019a; Mintz et al., 2020b). This study is the first report of using glyoxal crosslinked collagen fibers with high tensile strength as a filament for bioprinting and is a further significant advancement across the 3D biofabrication field by recreating the structural, cellular, and mechanical likeness of native tissue in an automated, scalable fabrication process, which was previously an ambitious and unrealized challenge (Murphy and Atala, 2014; Murphy, De Coppi and Atala, 2020).

RESULTS

Subhead 1: Bioprinting concept and design

We established an original Assembled Cell-Decorated Collagen (AC-DC) bioprinting method (Fig. 1) to produce implants approximating native musculoskeletal tissue properties for collagen fiber alignment and cellular distribution, such as found in musculoskeletal tissue. AC-DC bioprinting controllably seeds or “decorates” cells onto collagen microfiber as it passes through a cell-seeding reservoir before being wrapped next to and on top of itself to produce aligned 3D constructs mimicking native, regularly organized (aligned) musculoskeletal tissue architecture (movie S1). Printed implants are formed on temporary rigid frames, which maintain fiber alignment and 3D macrostructure during printing. With AC-DC bioprinting, fiber-based implants with designed width, length, thickness, and porosity, based on the print bed conformation and the computer-aided design (CAD) file, can be rapidly and repeatably produced via a fully automated process.

A custom extrusion printhead (Fig. 1A) was designed and incorporated with a Folger Tech FT-5 R2 commercial 3D printer. Two separate planetary geared stepper motors with lead screw assemblies mechanically compress disposable syringes individually, extruding cell suspension with sub-microliter resolution. Multiple cell-solution printheads can prospectively facilitate the production of heterogeneous implants with differing cell populations in distinct regions (Fig. S1). Cell suspensions prepared in hyaluronic acid (HA) solutions, acting as “cellular glue”, were extruded into the seeding manifold during printing, where cells uniformly coated collagen fiber being drawn through the manifold (Fig. 1B). The volume of cell suspension extruded per millimeter of drawn fiber is a user-determined process parameter, offering a means to control the resulting cell density and the total number of cells throughout an implant. A custom printed implant collection assembly was designed (Fig. 1A) in which small rigid frames (Fig. 1C) are held between two stepper motors. Typically, frame designs consist of two horizontal bars or dowels kept a fixed distance apart by custom 3D-printed frame ends, forming a central opening to limit cell migration from the implant to the frame and enable improved nutrient diffusion to the implant from the surrounding cell culture media. Hyaluronic acid was selected at 5mg/ml based on empirical testing of lower and higher concentrations, where the chosen

concentration provided optimal manufacturability without clogging the print head or being to dilute to adhere to the collagen fibers

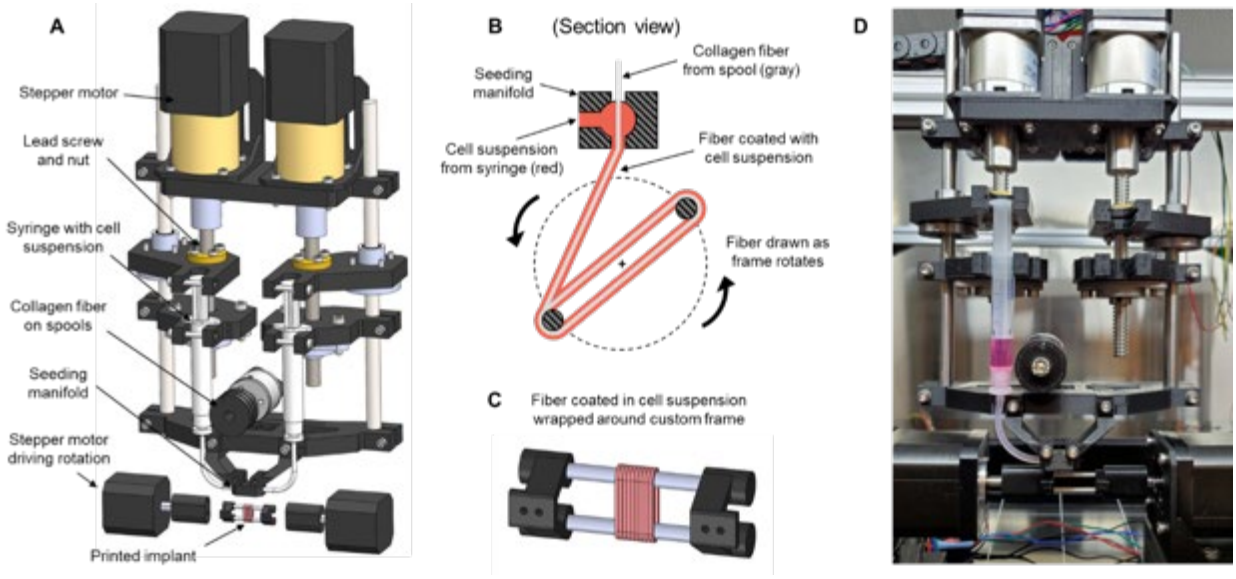

Fig. 3-1. Assembled Cell-decorated Collagen (AC-DC) bioprinting concept and design. (**A**) Computer-aided design (CAD) model of our custom extrusion printhead and collection assembly with critical components identified. (**B**) Section view illustrating the cell seeding and implant biofabrication process. Collagen fiber passes through a seeding manifold, where it is uniformly coated with a cell suspension. The coated fiber is drawn onto a frame of arbitrary shape and dimensions and wrapped in parallel and on top of itself to form a 3D implant. (**C**) CAD model of a parallel fiber implant formed on a rigid frame with a multifunctional design. Frames maintain implant fidelity during culture, and implants are secured with sutures and easily removed from frames before further testing or implantation. (**D**) Photograph of printhead and collection assembly housed in a laminar flow hood during a single cell-solution bioprint.

Subhead 2: Implant fidelity and cellularity

Cellularized collagen microfiber implants were printed rapidly and repeatably onto various frame geometries (Fig. 2A-C) with centimeter-scale implants produced in around 20 minutes. After securing implants into bundles using sutures, they were easily removed from a frame (Fig. 2D) by removing one or both PLA frame ends and sliding implants off the steel dowels. Across varying custom geometries, rigid frames were found to maintain fiber alignment and the macrostructure of printed implants in culture over several weeks. As such, benchmark implants were printed with hMSCs to assess cell metabolic activity after 1, 4, and 7 days in culture using the alamarBlue assay (Fig. 2E). Fluorescence indicating metabolic activity of cellularized implants was found to increase 5-fold over a 7-day culture period, indicating an increase in cell health, activity, and proliferation.

Transmitted light microscopy of printed implants shows striations indicative of densely packed parallel fiber after four days of culture (Fig. 2F). Fluorescence imaging of implants printed with hMSCs stained with a cytoplasmic label (green), dead cell nuclear label (red), and fiber autofluorescence (blue) after four days of culture shows cells distributed throughout (Fig. 2G). Notably, cells were visibly parallel to the collagen fiber direction. A grouping of three collagen microfiber strands (printed simultaneously from 3 spools of fiber attached to the printhead) was printed with hMSCs and labeled to assess the precision of the printing process (Fig. 2H). These three fiber strands act as the “building blocks” of printed implants, as three fiber strands are continuously drawn through the printhead, seeded with cells, and wrapped next to and on top of one another to form 3D implants.

Cell viability throughout printed implants was assessed qualitatively and quantitatively by fluorescent imaging of hMSCs. Qualitatively, generally, high viability is indicated by live cells (green), greatly outnumbering dead cells (red) (Fig. 2G, H). Quantitatively, ImageJ was used with established cell counting techniques to compare the number of live and dead cells throughout implants immediately after printing. For representative implants printed with typical process parameters,

hMSCs were found to be 93.2±1.7% viable immediately after printing, and cell viability was consistently above 90% for various implants geometries and printing conditions. However, quantifying viability by fluorescent imaging becomes difficult beyond several days of culture, as cells become confluent throughout the implants, with individual cells becoming indistinguishable.

Additionally, fluorescence imaging of cells (green) and fiber autofluorescence (blue) shows printed implants with a uniform initial distribution of hMSCs throughout after one day in culture and confluent densely-cellularized implants after 26 days in culture (Fig. 2I). Printed cells were found to attach to and grow along the collagen fiber within 24 hours and continued to proliferate to confluency at a rate dependent on cell type, initial cell printing density, and culture conditions. In extended culture, the gross appearance of implants transitioned from largely translucent with visible fiber-like surface texture to an opaque white to yellowish color with a smooth surface texture (Fig. S2), indicating a significant accumulation of deposited ECM. Dense cellular ingrowth as cells bridged gaps between adjacent fibers was also observed, including hMSCs after six weeks of culture on implants sutured into bundles (Fig. 2J) imaged by transmitted light and fluorescence microscopy with cells (green) and fiber autofluorescence (blue).

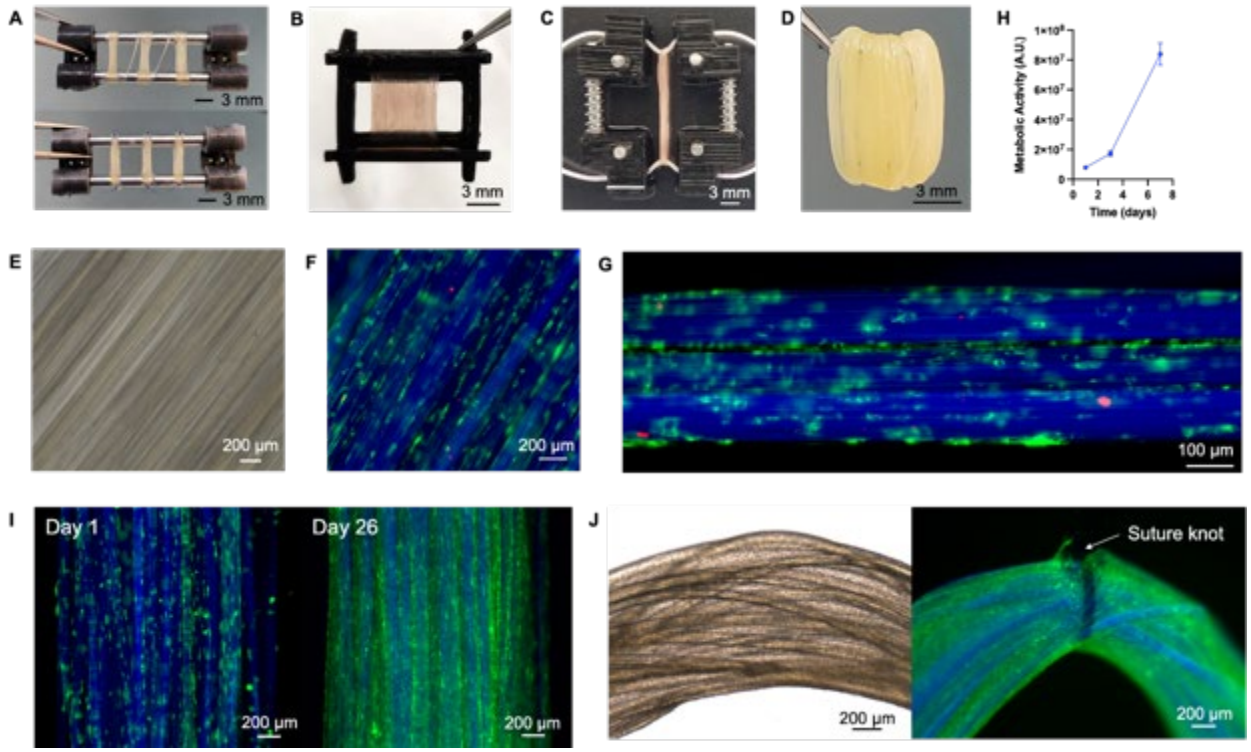

Fig. 3-2. Implant fidelity and cellularity. (**A**) Three printed implants on a multifunctional frame before (top) and after (bottom) being secured with suture. (**B**) A larger printed implant on a custom frame geometry. (**C**) An implant is printed onto two lengths of sutures and held in tension by a custom frame. (**D**) Tweezers hold a printed implant after being secured with a suture and removed from a frame. (**E**) Fluorescence intensity indicating cell metabolic activity using the alamarBlue assay for implants printed with hMSCs after 1, 4, and 7 days of culture (n=6). **(F)** The transmitted light image of a printed implant showing striations indicative of densely packed parallel fiber after four days of culture. (**G**) Fluorescence image showing hMSCs distributed throughout and parallel to the fiber direction after four days of culture. Fluorescence images F-I show all cells with the cytoplasmic label DiD (green) and collagen fiber autofluorescence at 405 nm (blue), with images F and G additionally showing dead cell nuclei with EthD-1 (red). (**H**) Fluorescence image showing hMSCs attached to and distributed along three “building block” strands of collagen fiber after four days in culture. (**I**) Fluorescence images of a printed implant showing an initial distribution of cells after 1 day of culture and a confluent densely-

cellularized implant after 26 days of culture. (**J**) Transmitted light image (left) and fluorescence image (right) of implants secured by suture showing dense cellular ingrowth of hMSCs between and on top of collagen fibers after 6 weeks of culture.

Subhead 3: Cell directionality and distribution

The directionality of the matrix has been shown to affect function, cellular remodeling potential (Foolen *et al.*, 2018) and the alignment of cell-produced extracellular matrix (Wang *et al.*, 2003). As such, directionality analysis in ImageJ was used to quantify matrix directionality throughout AC-DC implants using fluorescence imaging and image processing techniques. A representative composite image of a typical 2 × 2 mm field of view of an implant printed with MPCs after 14 days of culture is shown in Fig. 3A, with directionality analysis conducted on the fiber-only component of the image (blue) and cell-only component (green) shown in Fig. 3B and Fig. 3C, respectively. Analysis of the fiber-only component shows a narrow frequency distribution, indicating highly parallel fiber with nearly all directional features within ±10° of the peak orientation.

Additionally, we developed methods to quantify the distribution of cells throughout implants by adapting means for analyzing the distribution of particles within a field of view (Han, Furst and Kim, 2014; Ober, Foresti and Lewis, 2015). These methods offer a quantitative means to validate AC-DC process control and repeatability for the uniform placement of cells throughout implants. The results shown herein are representative and illustrate the capabilities of the cell distribution analysis methods. Images of printed AC-DC implants with fluorescently labeled MPC cytoplasmic membranes (Fig. 3D) were processed according to our protocols. The relative cellularity, determined by the number of white pixels indicating cellular material compared to black pixels indicating space devoid of cells, is calculated and plotted along the transverse (Fig. 3E) and longitudinal directions (Fig. 3F) of the image. Plots of relative cellularity offer a means to easily visualize cell distribution throughout printed

implants, with peaks, valleys, and skewness indicating variations in the number and placement of cells throughout a field of view. Linear regression analysis can further be used as a facile method to assess cellularity. For a perfectly uniform cell distribution with data analyzed in 100 bins, linear regression analysis will result in a horizontal line with a *y*-intercept of 0.01. Thus, the relative cellularity of each bin will be one-hundredth of the total number of cells. From a representative field of view of a printed AC-DC implant with MPCs, it is seen that linear regression results in a nearly horizontal line when measured across both the transverse and longitudinal directions (Fig. 3E, F), indicating an essentially uniform distribution of cells throughout the print. To contrast this, Fig. S3 illustrates a case where the distribution of cells is nonuniform and is made apparent by distribution analysis.

We further implemented an additional method to quantify the distribution of cells with a uniformity measure *U* based on Shannon entropy (Han, Furst and Kim, 2014; Ober, Foresti and Lewis, 2015). Briefly, the uniformity measure *U* ranges from 0 to 1, where a perfectly nonuniform distribution in which cells are present in exactly one half of a field of view scores a 0, and a perfectly uniform distribution in which cells are present exactly equally throughout scores a 1. As with calculating and plotting relative cellularity, uniformity was calculated across the transverse direction (U_{trans}), and the longitudinal direction (U_{long}) and was determined using the same imaging and image processing techniques. For example, for a representative AC-DC implant with MPCs, after 14 days of culture, cell uniformity analysis yields U_{trans}=0.87 and U_{long}=0.95 (Fig. 3D-F). Additional implants with hMSCs were analyzed immediately after printing and showed uniformity measures U_{trans}=0.65±0.07 and U_{long}=0.81±0.07, indicating that implants are initially substantially uniform and increase in uniformity as cells proliferate throughout during culture.

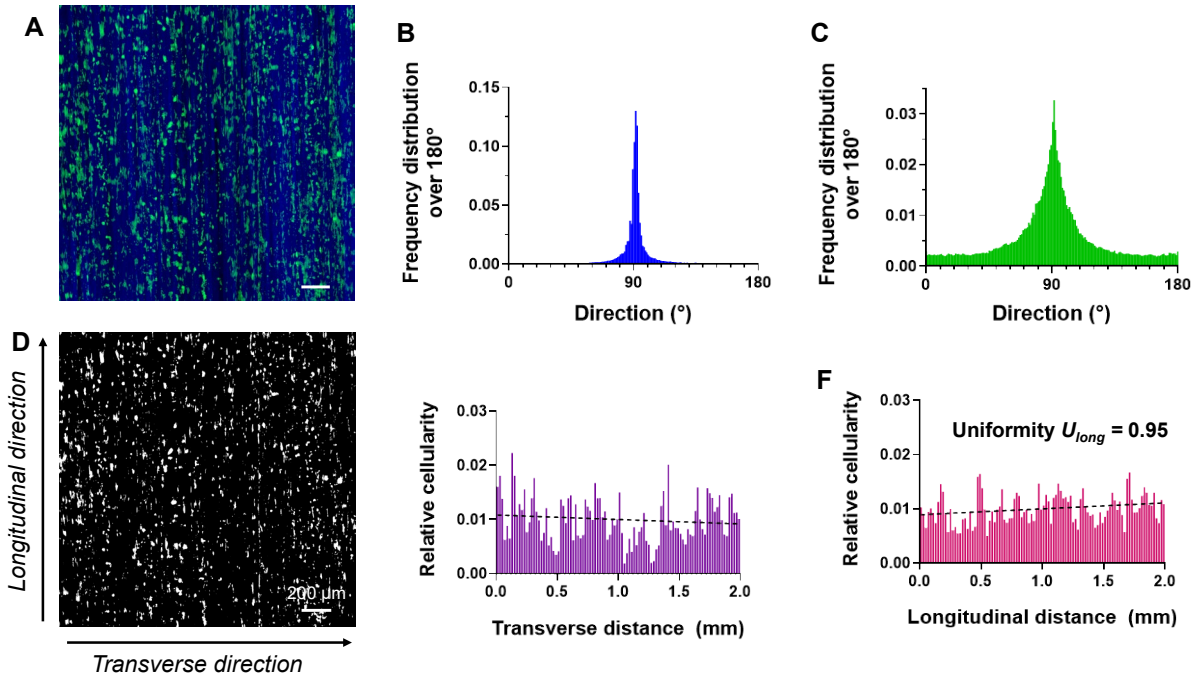

Fig. 3-3. Quantitative cellular distribution. (**A**) Typical field of view of a printed implant with rat muscle progenitor cells (MPCs) distributed throughout and aligned after 14 days in culture. The fluorescence image shows all cells with the cytoplasmic label DiD (green) and DAPI, with collagen fiber autofluorescence at 405 nm (blue). (**B**) Directionality analysis of the fiber-only component of (A), indicating highly parallel fiber. (**C**) Directionality analysis of the cell-only component of (A). (**D**) Image of (A) after processing for cell distribution analysis with cells shown in white, background in black, and transverse and longitudinal directions labeled. (**E**) Relative cellularity plotted along the transverse and (**F**) longitudinal directions, with nearly horizontal linear regression (dashed lines) and quantified uniformity measure *U* (ranging from 0 to 1), indicating a highly uniform distribution of cells.

Subhead 4: Implant mechanical properties

As MPCs are difficult to isolate and culture, and MSCs are well characterized, well adapted to culture, and used widely among different labs, MSCs were used for seeding in biomechanical testing. We assessed the mechanical properties of AC-DC implants printed with and without hMSCs after 1

day and 28 days in static culture to evaluate the load-bearing capabilities, stability, and effects of cellular remodeling *in vitro*. A custom 2-pin mounting approach for tensile testing (Fig. 4A) was found to provide significantly more consistent results when compared to mounting implants in standard compression grips, which often lead to implant damage, slippage, or staggered breakage of individual fibers within an implant. Representative stress-strain curves for each tested group are shown in Fig. 4B, with distinct “toe” regions of gradually increasing slope followed by linear regions of maximum slope and ultimately well-defined rapid decreases in stress indicating failure.

The cross-sectional area, ultimate tensile strength (UTS), tangent modulus, and strain at break were measured (Fig. 4D-F). For plots displaying UTS (Fig. 4D) and tangent modulus (Fig. 4E), horizontal lines are plotted indicating the mean UTS and tensile modulus of human ACL (Chandrashekar *et al.*, 2006), the strongest portion of the human supraspinatus tendon (Itoi *et al.*, 1995), and typical collagen gels used in tissue engineering (Achilli and Mantovani, 2010). Acellular and cellular implants produced using AC-DC bioprinting nearly match or exceed key mechanical properties of representative native human tendons directly after printing and continue to do so after 28 days in culture. Notably, the UTS and modulus of collagen microfiber implants are several orders of magnitude larger than the strength and stiffness of collagen gels commonplace in biomanufacturing approaches, which have a typical UTS around 20 kPa and tensile modulus around 200 kPa for a gel prepared at 2.8 mg/mL (Achilli and Mantovani, 2010). These values are characteristic of a collagen gel itself, irrespective of cell types included or the intended maturation of a 3D printed construct. Both acellular and cellular implants after 1 day and 28 days in culture underwent greater than 20% strain before failure (Fig. 4F). Thus, AC-DC implants providing sufficient elasticity to withstand typical strain values *in vivo*, such as the peak strain of 13.2% of the ACL during normal walking (Taylor *et al.*, 2013). While muscle biomechanical testing is very difficult to accurately assess due to its anisotropic, viscoelastic, hyperelastic, and highly nonlinear elastic behaviors, and thus largely understudied in the field, generally, the tensile properties of AC-DC implants greatly exceeded those of muscle, which can

have as low as 0.44MPa of UTS, around 2.0MPa of modulus, and strain at break exceeding 40% along the direction of the fibers (71).

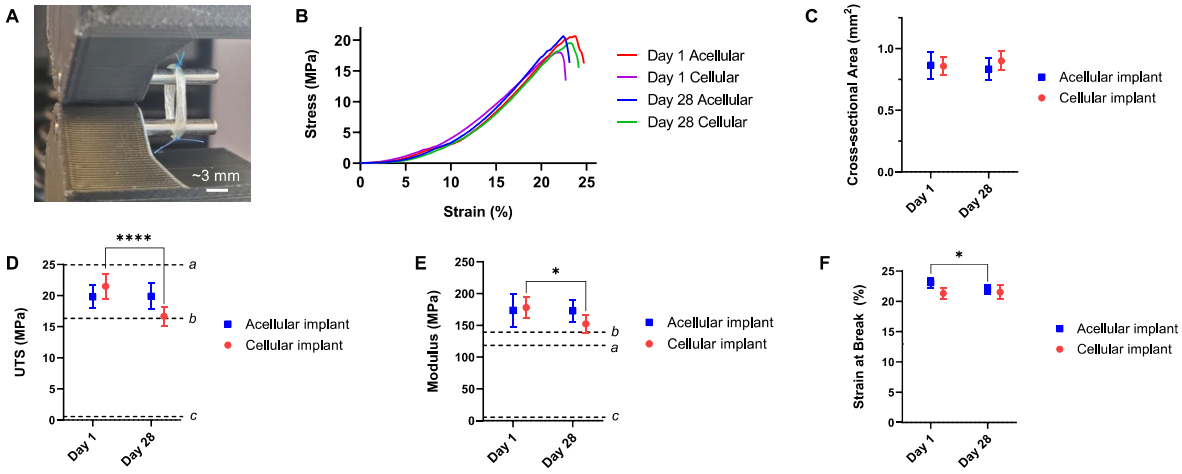

Fig 3-4. Implant mechanical properties. AC-DC implants were printed with and without hMSCs and assessed after 1 day and 28 days in culture. **(A)** A custom 2-pin uniaxial tensile tensing setup was found to improve consistency in implant failure compared to traditional compression grips. **(B)** Typical stress-strain curves for each experimental group. **(C)** Measured cross-sectional areas suggest space between individual fiber centers from the HA coating and the fiber swelling as we previously reported (43). **(D)** Ultimate tensile stress (UTS). **(E)** Tangent modulus. **(F)** Strain at break. [a] Mean UTS and modulus of human ACL (Chandrashekar *et al.*, 2006). [b] Mean UTS and modulus of the strongest portion of the human supraspinatus tendon (Itoi *et al.*, 1995). [c] Mean UTS and modulus of typical collagen gels used in tissue engineering (Achilli and Mantovani, 2010). (All data n=10 per group per time point *P<0.05, **** P <0.0001 indicates significance).

Subhead 5: Functional recovery in a volumetric muscle loss model

In vivo skeletal muscle repair studies were conducted over 12 weeks in a validated rodent VML model. At least 20% of overall muscle weight was removed from the tibialis anterior (TA) muscle of the lower left hindlimbs of Lewis rats (Corona *et al.*, 2014a; Mintz *et al.*, 2020b). Three methods of repair were assessed head-to-head: a control group receiving no repair, an acellular implant group receiving repair with AC-DC implants with no cellular component, and a cellular implant group receiving repair with AC-DC implants printed with rodent MPCs. Defect creation, initial placement of an implant, suture placement for implant attachment, and fascia replacement are shown in Fig 5A-D, respectively. All animals recovered post-surgery, and there were no signs of infection and no deaths. Across experimental groups, animal body weight increased similarly over the 12-week period (Fig. 5E), and measured defect weight at the time of surgery was not statistically different (Fig. 5F).

Functional testing was performed *in vivo* before defect creation and at 4, 8, and 12-weeks post-repair to assess muscle recovery post-operatively. Briefly, rat hind limbs were attached to a motorized footplate and stimulated electrically to measure maximum isometric torque generation (Corona *et al.*, 2014a; Passipieri *et al.*, 2019a; Mintz *et al.*, 2020b). Mean values are expressed as torque normalized to animal body weight at each time point (N-mm/kg of body weight) to control for increases in torque production due to animal growth. Baseline torque generation capability before defect creation did not vary statistically between treatment groups (Fig. 5G). Torque generation post-repair is expressed as raw torque (Fig. 5H) and percent of baseline torque generation (Fig. 5I). Both methods show similar trends with only slight variations in statistical significance.

Most notably, significant improvements in torque generating capability were observed over 12 weeks for injuries repaired with cellularized implants containing therapeutic MPCs. At 4 weeks, raw torque generation was significantly lower in the acellular and cellular implant groups than no repair, and the percent of baseline torque was significantly lower in the cellular implant group. We hypothesize that this initial decrease in torque generation capabilities is due to the early wound

healing processes, or possibly related to the initial tensile properties of the implant. However, by 8 weeks post-repair, there was no difference observed between the treatment groups. At 12-weeks post-repair, in contrast to findings at 4 weeks, raw torque generation was found to be significantly higher in the cellular implant group compared to the no repair group, and the percent of baseline torque was significantly higher in both the acellular and cellular implant groups, revealing key trends in the functional recovery of a VML injury among treatment groups. In addition, significant deterioration of function was found over 12 weeks for animals receiving no repair. In contrast, torque generation remained largely consistent for animals repaired with acellular implants, indicating that the presence of the collagen fiber implant without cells attenuated the functional deterioration associated with no repair.

It should be noted that the ablation of synergistic muscles during defect creation removes ~20% of torque generation in the anterior compartment (Mintz *et al.*, 2020b). As such, normalized torque would be limited to ~85 N-mm/kg across the treatment groups (106 N-mm/kg average at baseline). The mean functional recovery of the cellularized implant group at 12 weeks was 76% of the maximum theoretical recovery following synergist ablation compared to 67% in the acellular group and 57% in the no repair group. In addition, we noted that three of the seven animals receiving repair with cellular implants were observed to have a functional recovery of greater than 87%, with one animal recovering to near-maximal theoretical recovery compared to pre-injury levels (99%).

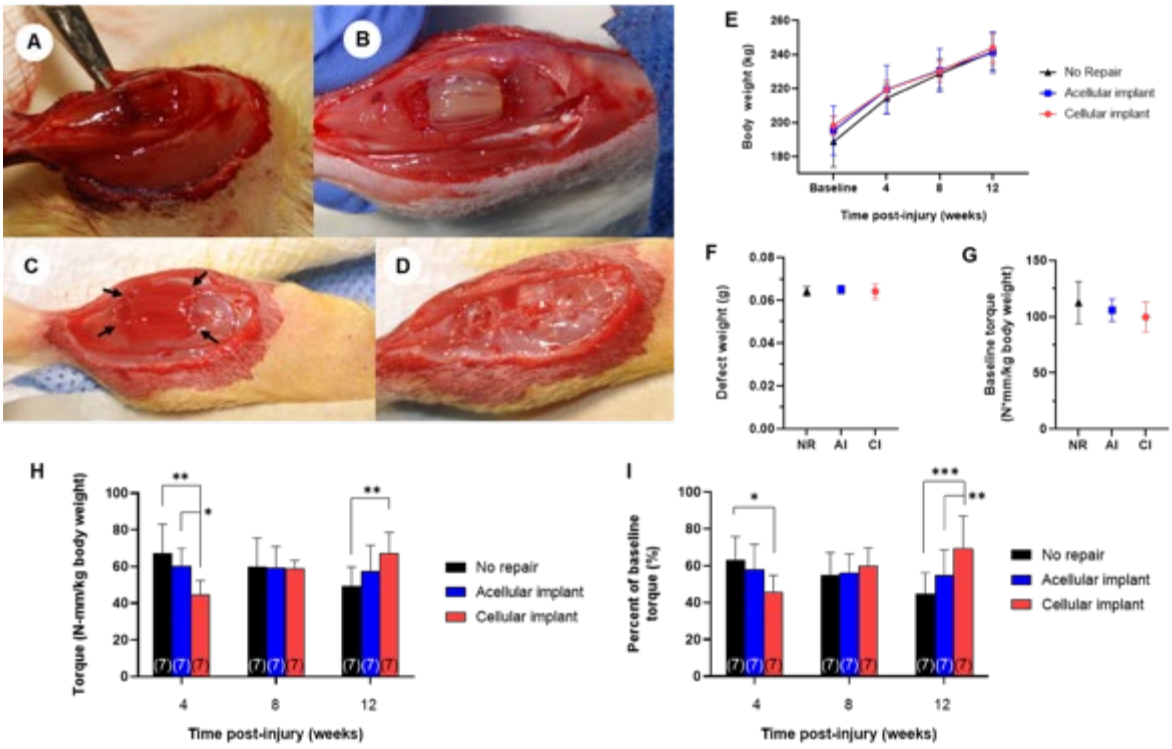

Fig. 3-5. Functional recovery in a rodent VML model. (**A**) Creation of a VML injury measuring approximately 1 cm x 0.7 cm x 0.5 cm and weighing at a minimum 20% of the overall TA weight. (**B**) Acellular AC-DC implant inserted into the injury site and (**C**) sutured into the injury site with arrows indicating attachment points. (**D**) Fascia sutured overtop of the injury site to secure the implant in place further. (**E**) Animal weight pre-injury at 4, 8, and 12-weeks post-injury, corresponding to functional testing timepoints. (**F**) Weight of defects created for No repair, acellular implant, and cellular implant (NR, AI, and CI, respectively) experimental groups (p = 0.8, no significant difference). (**G**) Baseline torque generation pre-injury (p = 0.9, no significant difference). (**H**) Measured torque and (**I**) percent of baseline torque at 4, 8, and 12-weeks post-repair, indicating functional recovery facilitated by implant implantation. (All data n=7 per group per time point, **P*<0.05, ***P*<0.01, ****P* <0.001 indicates significance).

Following assessment of functional recovery *in vivo* at 12-weeks, isolated TA muscles were collected for morphological and histological examination (Fig. S4). The gross morphology of those repaired by acellular and cellular AC-DC implants appeared more similar to control muscles than did the no repair group, which exhibited convex indentations at the injury location. More fascia was also noted in the repair groups. The distinction between implants and surrounding tissue was not obvious, indicating tissue ingrowth around or resorption of the collagen fiber implants. Isolated muscles were cross-sectioned through the belly and processed for H&E staining, with representative images for each experimental group shown in Fig. 6A-D.

As with gross examination, the unrepaired group exhibited distinct depressions at the injury site indicating a lack of tissue regeneration (Fig. 6B). Animals repaired with acellular and cellular implants, in contrast, exhibited more fullness to the tissue and uniform cross-sections similar to uninjured controls and thus improved cosmesis. Collagen fiber remaining from implants is visible within the injury sites as deep pink somewhat-circular cross-sections on the order of 100 μm diameter. Cellular ingrowth is visible in and around the implants (Fig. 6E and F). Fiber cross-sections are more apparent in the acellular implant group than the cellular implant group, possibly indicating an increased rate of fiber resorption for cellularized implants. For injuries repaired with cellular AC-DC implants, we also note the presence of new muscle fibers at the implant site (Fig. 6F). Higher magnification images from the H&E section further reveal the new muscle fibers and angiogenesis within the implant region (Fig S5), along with new collagen deposition as qualitatively indicated by Masson's Trichrome staining around the implant region (Fig S6).

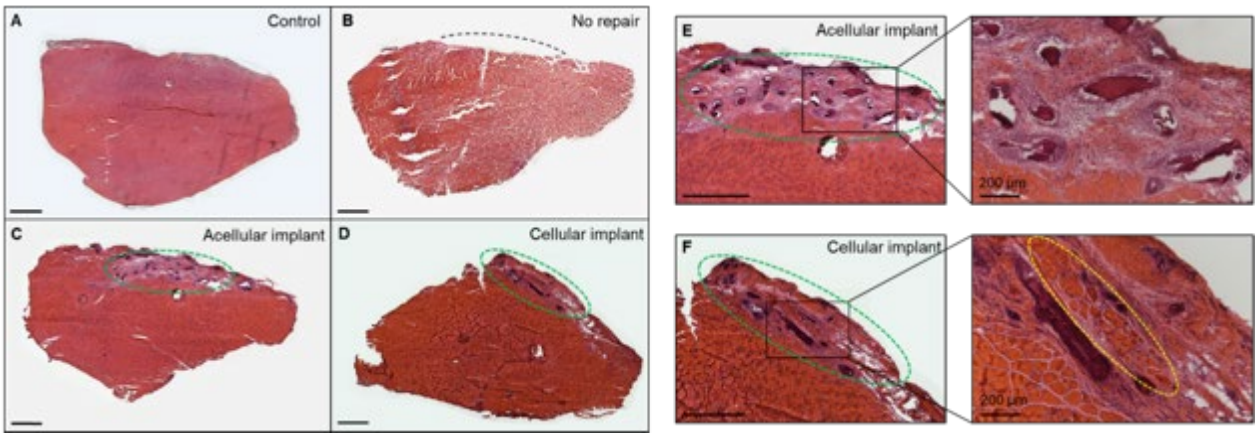

Fig. 3-6. Histological assessment of the TA. Representative H&E images of the TA muscle for (**A**) uninjured control, (**B**) no repair, (**C**) acellular implant, and (**D**) cellular implant experimental groups after 12 weeks. A black dashed line indicates the approximate area of defect creation. Green dashed ovals identify AC-DC implant locations. Magnified views of (**E**) acellular implant and (**F**) cellular implant locations with magnified windowed views showing cellular ingrowth and muscle fiber formation in the cellular implant location (yellow dashed oval). All scale bars are 1 mm unless otherwise noted.

Additional sections from the TA muscle belly were processed for analysis using SMASH, a semi-automated muscle fiber analysis software. Laminin and fluorophore 488 staining identify the outline of muscle fibers throughout sections (Fig. 7A-D) and SMASH analysis allows for individual fiber distinction, as seen with colorization applied (Fig. 6E-H). Analysis of the total number of fibers yields no significant difference between the uninjured control, no repair, acellular implant, and cellular implant groups (Fig. 7I). However, the median fiber cross-sectional area (FCSA) in muscle sections repaired with acellular and cellular AC-DC implants was significantly larger than that of the no repair group and did not differ significantly from the uninjured control (Fig. 7J). The cellularized implant and

control groups show the greatest difference from the no repair group, with p values of 0.0007 and 0.0002, respectively. Multiplying the total number of fibers by the median fiber cross-sectional area offers a representation of the total muscle fiber cross-sectional area (Fig. 7K). Again, this product shows no significant difference between uninjured controls and injuries repaired with acellular and cellular implants after 12 weeks in life, supporting that AC-DC implants facilitated an increase in total muscle fiber area.

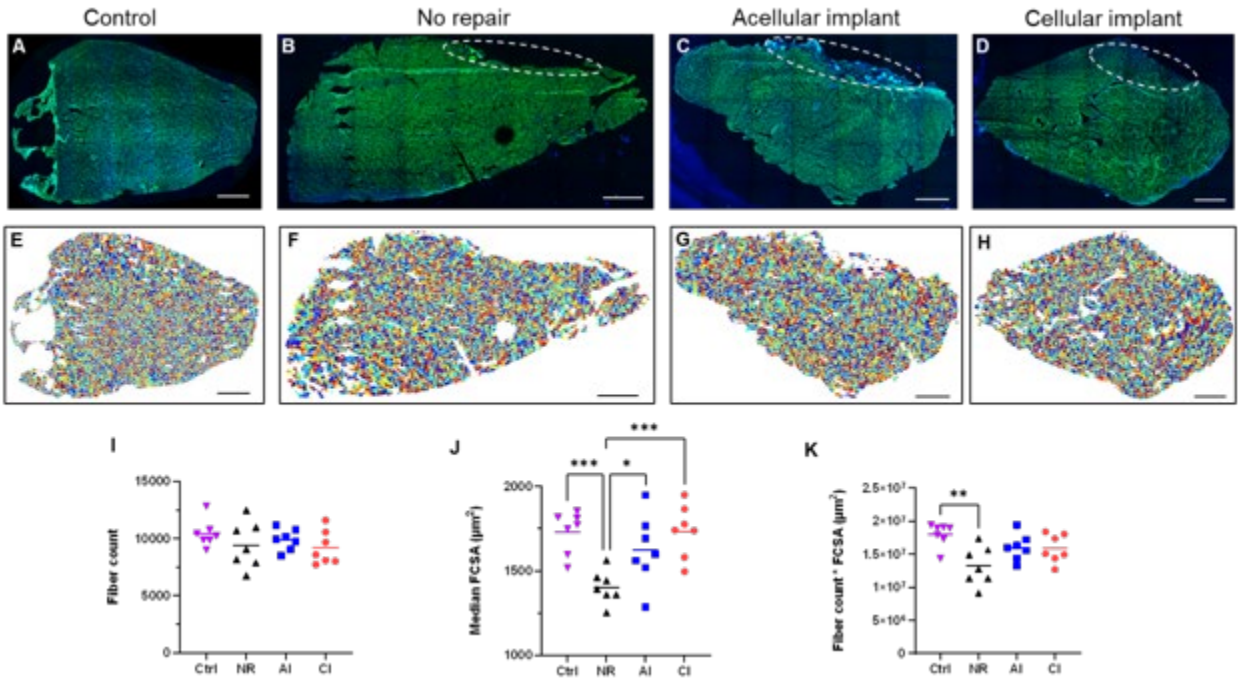

Fig. 3-7. Muscle fiber quantification using SMASH. Representative laminin-stained sections of the TA muscle for (**A**) uninjured control, (**B**) no repair, (**C**) acellular implant, and (**D**) cellular implant experimental groups with dashed ovals indicating the approximate region of injury. (**E-H**) Colorized outputs from the software identifying individual muscle fibers within sections corresponding to (A-D), respectively. (**I**) Total fiber count, (**J**) median fiber cross-sectional area (FCSA), and (**K**) the product of fiber count and FCSA for uninured control (Ctrl), no repair (NR), acellular implant (AI), and cellular

implant (CI) experimental groups. All scale bars are 1 mm. (All data n=7 per group per time point, *p<0.05 indicates significance).

DISCUSSION

Bioprinting concept and design. The AC-DC bioprinting approach rapidly and robustly produced implants consisting of highly aligned collagen microfiber with cells controllably placed throughout. As shown in Fig. 1, the system is built upon a commercial 3D printing platform. It is relatively affordable and straightforward in design, with all modifications completed using off-the-shelf components or parts 3D printed in-house from PLA. While densely packed parallel fiber implants with a rectangular macrostructure were the focus herein, fiber orientation, spacing, and overall implant geometry can be varied using the Python code developed to generate g-code for the AC-DC process. Printed fiber patterns can be designed such that fibers are angled with respect to one another to control material property anisotropy and fiber spacing or distribution. Additionally, fiber can be collected on “frames” of varying geometries rotated by the collection assembly (a cylindrical mandrel, for example), and achievable geometric complexity could feasibly be expanded using a collection assembly capable of multi-axis manipulation. This bioprinting process is particularly well-suited for producing planar, cylindrical, or prismatic geometries. Such geometries are ideal for applications targeting the augmentation or replacement of soft musculoskeletal tissues, where implants of aligned collagen fiber mimic the architecture of these native tissues. For applications in which complex geometries are required, however, AC-DC bioprinting could be augmented with additional substrate geometries to produce more complex shapes and patterns using biotextile or other approaches.

Implant print fidelity and cellularity. Printing with a single cell suspension, as in Fig. 2, AC-DC implants consist of densely-packed parallel collagen fiber with designed macroscopic dimensions. As Fig. 2 illustrates, the microarchitecture and topography of AC-DC implants were shown to facilitate and guide cell attachment, regular distribution, and proliferation *in vitro*. We envision that this

microstructural guidance for both printed and endogenous cells in the case of implantation will ultimately lead to improved tissue strength and functional contractility for VML and other musculoskeletal applications. Printed implants exhibited a high degree of directionality for collagen fiber and cells analogous to native musculoskeletal tissues (Fig. 3A-C). In addition to impacting cellular remodeling potential (Foolen *et al.*, 2018) and cell-produced ECM organization (Wang *et al.*, 2003), cell and matrix alignment may play a critical role in organized tissue biointegration and cell differentiation. For hMSCs in particular, an aligned collagen matrix has been shown to significantly upregulate the expression of tendon-specific markers, including scleraxis, tenomodulin, tenascin-C, and collagen-III compared to a randomly oriented matrix (Kishore *et al.*, 2012).

Cell directionality and distribution. Qualitative analysis methods were implemented to assess both cell orientation and distribution throughout the implants (Fig. S3). The validity and significance of both techniques are reliant on consistent use of fluorescence labeling, image collection, and image processing techniques. The qualitative analysis shown herein enables the characterization of printed implants and the standardization and quality assessment of the AC-DC bioprinting process. These methods may also be applied to various tissue engineering approaches traditionally relying on subjective and qualitative descriptions.

Cell labeling plays a significant role in the interpretation of quantitative cell orientation and distribution analysis and is a methodology lacking standardization in the bioprinting field that is helpful to assess print quality. Our approach provides the first steps towards an unbiased and quantitative means of accessing bioprint fidelity in a novel way to address this deficiency in the field. Our described systems quantify our AC-DC bioprints (Fig. 3) with uniformity measure U nearing 1 found for both representative cases, indicating a largely uniform and homogeneous distribution of cells when analyzed across both the transverse and longitudinal directions. Alongside calculation of relative cellularity, these analysis methods provide quantitative measures describing the placement and

overall homogeneity of cells throughout bioprinted implants or even sections of native tissue (Fig. 3). These measures offer a powerful means of comparing batch-to-batch variation in fabricated constructs and comparing the spatial cellular properties of native tissue targeted for repair or augmentation, and to compare results among products, bioprinters, and labs. Cell distribution analysis can be conducted with cytoplasmic labeling (Fig. 3D-F) or cell nuclei labeling (Fig. 3). Generally, cytoplasmic labeling enables analysis at a lower magnification and over a larger field of view. In contrast, cell nuclei labeling offers improved accuracy due to minor cell-to-cell variation in the size of the nucleus compared to the cytoplasm. Cell orientation was also found to impact cell distribution analysis when using cytoplasmic labeling. More severe peaks and valleys are present in the measured relative cellularity across the transverse direction compared to those measured across the longitudinal direction (Fig. 3D-F). Changes in cellular orientation can be attributed to cell direction, which acts to increase the measured grayscale value in the direction of the cell (pixel columns measured across the transverse direction). Regardless, both labeling approaches were found to enable meaningful quantification of cell distribution throughout a field of interest. Future studies will adapt these methods for direct comparison of cellularity between bioprinted constructs and native tissue sections.

Implant mechanical properties. As shown in Fig. 4, critical mechanical properties of AC-DC implants both with and without cells and after 1 and 28 days of culture were found to closely match or exceed properties of the human ACL (Chandrashekar *et al.*, 2006) and supraspinatus tendon of the rotator cuff (Itoi *et al.*, 1995), and offered properties ~1000 times those of typical collagen gels (Achilli and Mantovani, 2010) used in tissue engineering and bioprinting. Interestingly, the stress-strain curves of all experimental groups exhibited a distinct “toe” region, indicating a gradual increase in stress in response to tensile loading, which is often observed when testing explanted musculoskeletal tissue. While this behavior is attributed to the un-crimping of collagen fibrils in native tissue, herein, it is likely due to the non-simultaneous recruitment of constituent fiber throughout printed implants. Although by a different mechanism, the presence of a toe region may indicate that AC-DC implants further mimic

the functional behavior of native tissues to act as biological “shock absorbers” to suddenly applied loads.

Perhaps most notably, AC-DC implants offer the structural and mechanical properties required to withstand and transmit significant loads in the body and feasibly act as clinically relevant tissue augmentations immediately after printing. This progresses beyond current biomanufacturing approaches, which often require months of complex and costly bioreactor culture to improve the mechanical properties of produced constructs (Herchenhan *et al.*, 2013; Puetzer and Bonassar, 2016; Novakova *et al.*, 2017). Most (>80%) of the AC-DC print strength was retained in culture over 28 days, with the decreases in the strength and stiffness of cellularized implants being statistically significant over time. While acellular implants did not experience reductions in tensile properties over 28 days in culture, indicating the *in vitro* stability of the collagen microfiber alone, we hypothesize that the slight decreases in cellular implant properties could be attributed to cell-induced degradation and remodeling of the collagen fiber. From gross observation, cells were found to have bridged gaps between adjacent fibers and created a more opaque, smooth implant appearance as in Fig. 2J. In addition, while fibers were bound to one another by cells and newly synthesized ECM, we did not observe an increase in tensile strength or stiffness. Thus, we theorize that cell-induced degradation of the collagen fiber has outweighed any potential increase due to newly deposited ECM, primarily due to the difficulty of ECM materials matching the extremely high initial strength and stiffness of the collagen microfiber.

Strain rate should be considered when comparing mechanical properties of materials or tissues across different studies due to viscoelastic effects where differences in strain rate may affect measured strength and stiffness. AC-DC implants were tested at a strain rate of 10%/s, which falls within the range of studies included for comparison. Specifically, human supraspinatus tendon was tested at 10%/s (Itoi *et al.*, 1995), human ACL at 100%/s (Chandrashekar *et al.*, 2006), and collagen

gels were tested at 1%/s (Achilli and Mantovani, 2010). Measurement of properties at identical strain rates is not always feasible, as lower strain rates have been shown to cause avulsion failure rather than midsubstance failure of the ACL (Chandrashekar *et al.*, 2006), for example. While higher strain rates have been shown to moderately increase the properties of collagen gels, they remain several orders of magnitude below those of AC-DC implants or native tissue (~10 kPa UTS and ~25 kPa modulus at 6%/s strain rate)(64). Thus, the effects of varying strain rate on properties reported in these studies is assumed to be minor such that the general comparisons herein are valid.

Functional recovery in a volumetric muscle loss model. *In vivo* assessment of AC-DC implants revealed a substantial capacity for recovery in a volumetric muscle loss injury model, with acellular implants preventing functional deterioration associated with no repair and, most notably, cellular implants with MPCs facilitating a significant increase in torque generating ability (Fig. 5). Histological and computational analyses support that the mechanism for improved functional regeneration over 12 weeks is the formation of new muscle fibers (Fig. 6F) and increase in total muscle size (Fig. 7K). While all experimental groups showed a significant number of new cells in the area of the injury, the group receiving no repair did not exhibit the same maturity of cells as in groups receiving AC-DC implants. This was supported by the SMASH analysis, with the total fiber count between groups found to be similar (Fig. 7I) but the median fiber cross-sectional area in groups receiving implants found to be substantially higher (Fig. 7J). The SMASH analysis is however limited by the sectioning quality and region of interest defined. While implants with mechanical properties approximating those of tendon tissues were effective herein, performance may potentially be further improved by producing implants with properties more closely matching those of muscle.

Slight fiber degradation was noted in the 12 week explants and is consistent with our prior published work on the collagen fiber stability characteristics (43). Neovascularization was also noted around the implant region as demarcated by the collagen fibers, as again supported by our prior

studies with these collagen fibers implanted *in vivo* (43). Overall, the functional and histological properties of AC-DC implants meet or exceed our prior studies in this model. It is possible that the higher tensile properties of the AC-DC implants relative to native muscle tissue may beget scarring at time points beyond the range examined in this study. SMASH fiber analysis shows the median fiber cross-sectional area (FCSA) in muscle sections repaired with AC-DC implants was significantly larger than that of the no repair group, and did not differ significantly from the normal muscle tissue in the uninjured control (Fig. 7J). The cellularized implant and control groups show the greatest difference from the no repair group, with p values of 0.0007 and 0.0002, respectively. In a further assessment of the muscle fiber quality as stained by laminin, which generally excludes fibrotic (type I collagen tissue) in the implant site, multiplying the total number of fibers by the median fiber cross-sectional area offers a representation of the total muscle fiber cross-sectional area (Fig. 6K), where no significant difference between uninjured controls and injuries repaired with AC-DC implants after 12 weeks in life, supporting that AC-DC implants facilitated an increase in total muscle fiber area. Nonetheless, the strong collagen fiber implants may promote fibrosis in muscle which may be present or develop over longer treatment courses and will be explored in future works. While extensive further analysis is needed for assessing fibrosis in these samples, fibrosis may be suggested in the limited trichrome data, although fair comparisons to other technologies for VML are not possible due to a lack of direct comparisons or validated scoring methods.

Interpretation of results and clinical translation. We have developed AC-DC bioprinting to produce regenerative collagen fiber-based implants that can be incorporated into the surgical management of a number of musculoskeletal injuries to restore lost soft tissue structure and function. In particular, tears at the myotendinous junction of the muscle-tendon unit as well as en bloc muscle defects have remained vexing injuries with few, durable reconstructive solutions. Production and analyses were done at a scale appropriate for rodent-sized implants, yet processes can readily be scaled up to produce human-scale implants. In conjunction with scale-up, techniques to facilitate

implant handling and surgical delivery are needed for many surgical implants. For prospective human clinical use, critical quality attributes of AC-DC implants are important next steps. The *in vitro* analysis methods implemented herein provide valuable tools for quantifying cellular and mechanical properties, useful for future validation work. While acellular implants showed some efficacy in the VML model, only bioprinted implants containing therapeutic cells facilitated a significant degree of functional recovery. Although there are complexities associated with clinically translating cell-based biomanufactured products, AC-DC bioprinting has the potential to become a platform technology capable of producing implants with revolutionary regenerative capabilities to address a range of musculoskeletal and other disorders.

MATERIALS AND METHODS

Subhead 1: Study design and reproducibility

Rodent VML model. Choice of sample size (n=7 animals per group per time point) was informed by our previous studies and experience with regenerative implants in a rat TA injury model (Corona *et al.*, 2014a; J. A. Passipieri *et al.*, 2017; Mintz *et al.*, 2020b). This study was intended to provide robust statistics to determine significant differences between groups for quantitative *in vivo* functional analysis. Isometric contractile torque has historically resulted in the greatest variability among treatment groups and is the determining factor for the required number of animals. Power analysis assuming a 30% difference (standard deviation 20%) between treatment and control groups indicated that 7 animals per group achieves 80% power at alpha = 0.05. The number of animals was not altered over the course of the study and endpoints were determined before study initiation. No animals exhibited signs of pain and distress or required euthanasia before designated study end points.

Treatment groups were randomized and quantitative analysis methods were standardized to minimize any undue bias.

Subhead 2: Experimental methods

Collagen fiber production and sterilization. Collagen microfibers for use in AC-DC bioprinting were produced using a wet-spinning microfluidic extrusion process, as described in detail in our previous work (Dasgupta *et al.*, 2021). Briefly, clinical-grade lyophilized bovine collagen from Symatese (France) was dissolved in acetic acid. Next, acidified collagen at 16 mg/ml was extruded through microneedles into a bath of a neutralizing alkaline formation phosphate buffer containing salts and polyethylene glycol and passed through a bath of aqueous 20% ethanol. Eight monofilimanets runs of collagen fiber were pulled together during wet-extrusion to produce a resulting irregular (oblong)(43) ~41μm fiber (dry thickness as measured microscopically) that was collected on spools for subsequent glyoxal crosslinking, sterilization by electron beam sterilization (Steri-Tek, Fremont, CA) using a 20±2 kGy target dose, and stored desiccated until use.

hMSC and related cellularized implant culture. Human bone marrow-derived mesenchymal stem cells (hMSCs) (RoosterBio®, Ballenger Creek, MD) and 1×1×0.1cm AC-DC implants produced using hMSCs were cultured and maintained in serum-free, xeno-free media (RoosterBio®). Cell culture media was supplemented with 1-2% Gibco™ Antibiotic-Antimycotic (ABAM) (Thermo Fisher Scientific). Cells and implants were prepared and handled aseptically and cultured maintaining physiological conditions at 37°C and 5% CO_2. Implants remained fully submerged during culture, and two-thirds of the total media volume was replaced every 2-3 days. For comparative studies, acellular implants were cultured under conditions identical to those of cellularized implants.

MPC and related cellularized implant culture. Muscle progenitor cells (MPCs) were isolated as previously described (Corona *et al.*, 2014a). The tibialis anterior (TA) and soleus muscles of 4

weeks old female Lewis rats (Charles River Laboratories, Wilmington, MA) were excised, sterilized in iodine, and rinsed with PBS (Hyclone). Muscles were minced to create a homogenous cell slurry and then incubated for 2 h at 37C in 0.2% collagenase (Worthington Biochemicals, Lakewood, NJ) in DMEM. The homogenous muscle slurry was then pre-plated onto 10-cm collagen-coated tissue culture dishes (Corning, Corning, NY) at 37C in a myogenic medium containing DMEM high glucose with 20% FBS, 10% horse serum (Gibco by Life Technologies); 1% chick embryo extract (Accurate, Westbury, NY), and 1% ABAM. After 24 h, the cell suspension was transferred to 15-cm Matrigel-coated (1:50; BD Biosciences, Franklin Lakes, NJ) tissue culture dishes. Cells were passaged at 70–90% confluence and further cultured in proliferation media containing DMEM low glucose with 15% FBS and 1% AA. At passage 1, MPCs were frozen using proliferation media supplemented with 5% DMSO and subsequently shipped to Embody, Inc. for further passaging. 1×1×0.2 cm AC-DC implants printed with MPCs were cultured in myogenic media as described above. Acellular and cellular implants were printed 2-3 days before transportation to University of Virginia by car in a warmed and vented container (approximately 3-hour travel time), cultured 2-3 days before implantation. Cells and implants were prepared and handled aseptically and cultured maintaining physiological conditions at 37°C and 5% CO_2. Implants remained fully submerged during culture, and two-thirds of the total media volume was replaced every 2-3 days. For comparative studies, acellular implants were cultured under conditions identical to those of cellularized implants.

Preparation of cell suspensions for AC-DC bioprinting. Hyaluronic acid (HA) sodium salt from Streptococcus equi (Sigma-Aldrich, St. Louis, MO) was dissolved in appropriate cell type-dependent culture media to a final concentration of 5 mg/mL in a conical glass vial gently stirred overnight. HA concentration was previously optimized. Immediately before printing, cells were harvested and resuspended within the hyaluronic acid solution to desired concentrations by gentle pipetting. Fibers were coated in HA via the print head described and illustrated in Figure 1 by a

continual drawing of the HA on the fiber as it is pumped from the syringe onto the fibers with the cells in suspension within the HA. Cell suspensions remained at room temperature during printing. Typical printed concentrations ranged from 1×10^6 cells/mL to 5×10^6 cells/mL.

AC-DC process control and commercial printer customization. Three collagen fibers were fed together through the seeding manifold (as pictured in figure S1) and attached at an initial anchoring point on the collection assembly to initiate bioprinting. As the collection assembly motors rotate the frame, fiber is drawn under tension at a calculated 1.2 m/hr (previously optimized) through the seeding manifold and coated by the extruded cell suspension. By coordinating the rotation of the frame and linear translation of the printhead along the width of the frame (the feed), cellularized implants of dense, highly aligned collagen microfiber are produced. A custom Python code was developed to accept user inputs for designed implant geometry and printing parameters, including the number of implants per frame, implant width, length, number of layers of fiber, the extruded volume of cell suspension per millimeter drawn fiber, feed distance between parallel fibers, and frame rotation rate, and output a corresponding g-code file. The g-code file contains all parameters and motion/extrusion commands to execute a designed print and is sent to the printer to produce the designed implant. Repetier-Host is used as a user interface to execute these commands and manual homing, motion, and extrusion commands.

Folger Tech FT-5 R2 commercial 3D printer hardware and firmware were highly modified to facilitate the AC-DC biofabrication approach. The fused deposition modeling printhead was removed and replaced with custom printhead components (Fig. 1A). Non-stock components for the printhead and collection assembly were 3D printed in-house from PLA or machined. All stepper motors and drive pulleys were replaced to improve the resolution on *X*, *Y*, and *Z* axes. The printer *Z-axis* control was repurposed as a new *R* rotational axis for the custom collection assembly and mounted to the printer's build plate. The printer firmware was modified accordingly to accommodate hardware and

control scheme changes. All components of the AC-DC printing approach contacting implants during printing were autoclaved or soaked in 100% ethanol for at least one hour. The printing and auxiliary handling processes were conducted in either a biosafety cabinet or HEPA filtered laminar flow hood to maintain aseptic environments.

Fluorescent labeling, microscopic imaging, and cell viability. According to recommended manufacturer protocols, the fluorescent label Invitrogen Molecular Probes Vybrant™ DiD (Thermo Fisher Scientific, Waltham, MA) was used according to recommended manufacturer protocols to visualize cell cytoplasmic membranes. According to recommended manufacturer protocols, the fluorescent label Ethidium Homodimer-1 (EthD-1) (Thermo Fisher Scientific, Waltham, MA) was used according to recommended manufacturer protocols to visualize dead cell nuclei. Bright autofluorescence of the collagen fiber at 405 nm allowed for clear visualization of fiber throughout implants. All fluorescence and transmitted light microscopic imaging were conducted on an inverted light microscope (Axio Vert.A1 Model, Zeiss, Germany), and composite images were produced using ZEN imaging software (Zeiss, Germany). The quantitative viability of hMSCs in 1×1×0.1 cm AC-DC implants was assessed immediately after printing, where the total number of cells in a field of view was determined by DiD labeling. The number of dead cells was determined by EthD-1 labeling. Representative fields of view from the central region of each implant were taken for live/dead counting, with results presented as mean ± standard deviation (n=6).

Metabolic activity assay. The alamarBlue® assay (Bio-Rad, Hercules, CA) was used to assess the metabolic activity of 1×1×0.1 cm AC-DC implants printed with hMSCs according to recommended manufacturer protocols. After 1, 4, and 7 days of culture, implants were incubated in an alamarBlue working solution for 4 hours, and sample media and blanks were collected in triplicate. Media was analyzed for fluorescence intensity at 560/590 nm excitation/emission using a Synergy HTX multi-mode microplate reader.

Quantifying cell distribution and uniformity. Appropriate fluorescence labeling techniques were applied to visualize cells throughout 1×1×0.1 cm AC-DC implants for analysis of representative implants with MPCs used in the VML study and additional 10×1.5×1 mm implants with hMSCs (n=6) for multi-sample analysis. For MPC and hMSC samples respectively, 2×2 mm and 1.5×1.5 mm fields of view showing several hundred cells were captured from the implant midsection for analysis. Images were converted to binary to visualize cells in black on a white background. The “Plot Profile” function of ImageJ FIJI (NIH Shareware, Bethesda, MD) using was then used to measure and plot the average grayscale value, with black pixels measured as 255 and white pixels measured as 0, of pixel columns taken across the transverse direction of the field of view, with the value for each column being the average grayscale value of pixels contained in that column. Similarly, the grayscale value is measured for pixel rows taken along the longitudinal direction. The value for each row is the average grayscale value of pixels contained in that row. A custom Python code was developed to group measured greyscale values into 100 bins and normalized to the total grayscale value of the field of view to represent the relative cellularity or cell material found in each transverse or longitudinal bin relative to the entire field of view.

Based on prior applications (Han, Furst and Kim, 2014; Ober, Foresti and Lewis, 2015), U (Equation 1) defines the uniformity measure based on the Shannon entropy of a printed implant, sprinted, Shannon entropy of a perfectly nonuniform particle distribution, snonuniform, and Shannon entropy of a perfectly uniform particle distribution, suniform. A perfectly nonuniform distribution is one in which particles entirely fill exactly half of a field of view. A perfectly uniform distribution is one in which particles are present equally throughout. Shannon entropy s (Equation 2) is calculated for a field of view with N pixel columns/rows across a field of view based on the probability pj (Equation 3) that a particle lies within the jth pixel column/row, where mj is the grayscale value of the jth column/row and M is the sum of grayscale values across the field of view. Thus, the uniformity value U ranges from 0 for a perfectly nonuniform distribution in which cells are present in exactly half of the field of view to 1

where cells are present exactly equally throughout the entire area. A custom Python code was developed to calculate U for a given field of view.

$$U \equiv \frac{s_{printed} - s_{nonuniform}}{s_{uniform} - s_{nonuniform}} \quad \text{Equation 1}$$

$$s = -\sum_j^N p_j \ln p_j \quad \text{Equation 2}$$

$$p_j = \frac{m_j}{M} \quad \text{Equation 3}$$

Mechanical property testing. 1×0.2×0.2 cm implants were secured into bundles with a suture at each end, mounted to a custom 2-pin mechanical testing setup (Fig. 4A), and pulled to failure under uniaxial tension using a uniaxial tensile testing machine (MTS Systems Corporation, Eden Prairie, MN) with a 100 N load cell. Implants were tested after 1 day and 28 days of culture. Pins were displaced at a rate of 1 mm/s (10%/s), and load-displacement data were recorded continuously. The "solid only" theoretical cross-sectional area was determined by multiplying the average cross-sectional area of individual collagen fibers measured using microscopic imaging by the total number of constituent fibers within the printed implants (Gentleman et al., 2003, 2006). "Solid only" cross-sectional area was assumed to be identical for each experimental group based on the consistency and stability of the collagen fiber. "Full implant" cross-sectional area was measured using digital calipers for each sample immediately before testing. Ultimate tensile stress (UTS) was determined by the peak load and cross-sectional implant area, and tangent modulus was determined by the slope of the linear region of the stress-strain curve. The strain was determined from the linear pin displacement during testing, and the gauge length was taken as the initial center-to-center distance between the two pins, with strain at break measured at the peak recorded load. A sample number of n=10 was found to offer statistical significance and consistency based on prior experiments.

VML injury model. In vivo skeletal muscle repair studies were conducted over 12 weeks using a total of 21 female Lewis rats (11–14 weeks old with a mean bodyweight of 198.4 g – 3.5 g) (Charles

River Laboratories) split into three groups. A VML defect was surgically created in the TA muscle of each rat as previously described (Corona *et al.*, 2014a; Passipieri *et al.*, 2019a; Mintz *et al.*, 2020b). A longitudinal incision was made along the lateral side of the left lower hindlimb, from the ankle to the knee. The skin was separated by blunt dissection from the underlying fascia. The fascia was cut and separated from the anterior crural muscles. The extensor digitorum longus (EDL) and extensor hallicus longus (EHL), synergist muscles in the anterior compartment, were isolated and ablated at the tendons to assess the impact of VML injury to the TA. The VML injury was created by excising the middle of the TA in an area measuring approximately 1 cm x 0.5 cm x 0.7 cm and avoiding the underlying tendon. The defect size was calculated as 20% of the TA, which was determined experimentally to be 0.17% of the animal's body weight. Immediately post VML injury, each group (n=7) received a different treatment, with the control group receiving no treatment, the acellular implant group receiving a 1×0.5×0.5 cm collagen-based implant with no cellular component, and the cellularized implant group receiving 1×0.5×0.5 cm regenerative constructs incorporating muscle progenitor cells. Implants were bound and sutured into the wound bed at the corners of the wound boundary region. (6-0 Vicryl; Ethicon, Somerville, NJ). The fascia was also closed with 6-0 vicryl interrupted sutures. In addition, the skin was closed with 5-0 prolene (Ethicon) interrupted sutures and skin glue to prevent reopening of the incision. Buprenorphine (0.05 mg/kg) was administered subcutaneously for 3 days post-surgery. All animals in this study were treated per the Animal Welfare Act and the Guide for the Care and Use of Laboratory Animals. All procedures were approved by the University of Virginia Animal Care and Use Committee.

In vivo functional testing. Functional testing was performed on all animals prior to VML surgery to establish baseline torque responses for each animal. Testing was again conducted post-healing at three time points of 4, 8, and 12 weeks post-surgery. *In vivo,* functional analysis was performed to assess recovery post-VML injury. Torque production of the subject's TA was measured in vivo as previously described (Corona *et al.*, 2014a; Passipieri *et al.*, 2019a; Mintz *et al.*, 2020b).

Rats were anesthetized (2% isoflurane; Henry Schein, Dublin, OH), and the left hindlimb was aseptically prepared. The rat was placed on a heated platform, and the left foot was secured at a 90 angle to a footplate attached to the Aurora Scientific 305C-LR-FP servomotor (Aurora, ON, Canada). Two sterilized percutaneous needle electrodes (Chalgren, Gilroy, CA) were inserted superficially through the skin to stimulate the left peroneal nerve. An electrical stimulus was applied (Aurora Scientific Stimulator Model 701C), and stimulation voltage and electrode placement were optimized with continuous 1 Hz twitch contractions. Contraction of the anterior crural muscles leading to dorsiflexion of the foot was determined by measuring the maximal isometric tetanic torque over a range of stimulation frequencies sufficient to result in the plateau of the torque response (10–150 Hz). At 12 weeks, animals were euthanized through CO2 inhalation and injured TA muscles, and contralateral control muscles were explanted, weighed, and frozen in preparation for imaging.

Histological and immunofluorescence examination. Histological and immunofluorescence examination. TA muscles were explanted at sacrifice. All tissues were flash-frozen in liquid nitrogen and stored at -80C until ready for sectioning. A cryotome was used to create 12 μm thick cross-sections of the experimental and control TA muscles for all animals in each group at 12 weeks. To ensure analysis of similar areas, cross sections were always taken from an area in the center of the wound. Cross sections were all taken within 0.5 mm of the midpoint of the wound and numbered by depth to select cross sections from similar areas of each sample. The area of each cross section was approximately 7x8 mm. Hematoxylin and Eosin and Masson’s trichrome staining was performed following standard procedures to assess cellular morphology. Images were captured at 4x and 10x (Nikon Upright Microscope). Histological images were examined, particularly in the region of injury, to identify new fiber formation, cellular proliferation, growth, or potential fibrosis. At least 3 cross sections were imaged per animal and representative images were chosen for examination. Other cross-sectional images were stained with immunofluorescent fibrin antibody stain conjugated to Alexa Fluor 488. All antibodies were diluted in Dako Antibody Diluent (Dako Antibody Diluent S0809;

Agilent Technologies). Images were captured by confocal microscopy (Leica DMi8; Buffalo Grove, IL). These images were enhanced and uniformly edited using the CLAHE (contrast limited adaptive histogram equalization) plugin of ImageJ (NIH). The entire cross section of tissue was analyzed, which was approximately 7mm x 8mm. Again, cross sections were all from within 0.5 mm of the center of the wound. In control samples, the midpoint of where the wound would have been made was selected by measuring from the tendon of the TA. Analysis was conducted to determine the fiber cross-sectional area and the minimum Feret diameter. These area measurements were accomplished using the software SMASH, a semi-automatic muscle analysis program built in MATLAB (MathWorks), developed at the University of Pennsylvania. The SMASH software, its functions, and limitations have been thoroughly detailed (Smith and Barton, 2014a). One primary advantage to this software was the ability to analyze the entire area of the cross-section without the human errors associated with hand-counting small portions of the tissue. In the 12-week samples that were analyzed in this study, the site of the original VML defect was located by the presence of fibrosis on the surface of the muscle, and in all cases, either an apparent concave depression on the surface of the muscle or detectable, albeit sometimes modest disruptions of the usually smooth surface architecture of the surface of the TA muscle. One primary advantage to this software was the ability to analyze the entire area of the cross-section without In the 12-week samples that were analyzed in this study, the site of the original VML defect was located by the presence of fibrosis on the surface of the muscle, and in all cases, either an apparent concave depression on the surface of the muscle or detectable, albeit sometimes modest disruptions of the usually smooth surface architecture of the surface of the TA muscle. The distinct anatomical structure of the TA due to its close association with the tibia also allowed for ease in determining where the original defect was made.

Subhead 3: Statistical analysis. All data are presented as mean ± standard deviation unless otherwise noted. Sample group sizes are given in respective figure captions, main text, or Materials and Methods sections. Where appropriate, the statistical significance of functional recovery data was determined by one-way ANOVA or two-way ANOVA with multiple comparisons and Fisher's LSD. SMASH data was analyzed using the Brown-Forsythe and Welch ANOVA test with multiple comparisons.

Supplementary Materials*

Fig. S1. Dual-solution AC-DC bioprinting proof of concept.

Fig. S2. The difference in the appearance of acellular and cellular implants.

Fig. S3. Relative cellularity and uniformity of tissue interface.

Fig. S4. Explanted TA muscles 12 weeks post-repair.

Fig. S5. High magnification H&E

Fig. S6. Masson's Trichrome Staining

Movie S1. Video of AC-DC bioprinting showing the formation of a 3D implant.

*Can be found online https://onlinelibrary.wiley.com/doi/full/10.1002/adhm.202101357

References and Notes

Abrahamsson, C.K. *et al.* (2010) 'Chondrogenesis and Mineralization During *In Vitro* Culture of Human Mesenchymal Stem Cells on Three-Dimensional Woven Scaffolds', *Tissue Engineering Part A*, 16(12), pp. 3709–3718. Available at: https://doi.org/10.1089/ten.tea.2010.0190.

Achilli, M. and Mantovani, D. (2010) 'Tailoring Mechanical Properties of Collagen-Based Scaffolds for Vascular Tissue Engineering: The Effects of pH, Temperature and Ionic Strength on Gelation', *Polymers*, 2(4), pp. 664–680. Available at: https://doi.org/10.3390/polym2040664.

Akbari, M. *et al.* (2014) 'Composite Living Fibers for Creating Tissue Constructs Using Textile Techniques', *Advanced Functional Materials*, 24(26), pp. 4060–4067. Available at: https://doi.org/10.1002/adfm.201303655.

Ankrum, J.A., Ong, J.F. and Karp, J.M. (2014) 'Mesenchymal stem cells: immune evasive, not immune privileged', *Nature Biotechnology*, 32(3), pp. 252–260. Available at: https://doi.org/10.1038/nbt.2816.

Bliley, J.M. *et al.* (2015) 'Ethylene Oxide Sterilization Preserves Bioactivity and Attenuates Burst Release of Encapsulated Glial Cell Line Derived Neurotrophic Factor from Tissue Engineered Nerve Guides For Long Gap Peripheral Nerve Repair', *ACS Biomaterials Science & Engineering*, 1(7), pp. 504–512. Available at: https://doi.org/10.1021/ab5001518.

Bour, R.K. *et al.* (2020) 'Bioprinting on sheet-based scaffolds applied to the creation of implantable tissue-engineered constructs with potentially diverse clinical applications: Tissue-Engineered Muscle Repair (TEMR) as a representative testbed', *Connective Tissue Research*, 61(2), pp. 216–228. Available at: https://doi.org/10.1080/03008207.2019.1679800.

Butler, D.L., Juncosa, N. and Dressler, M.R. (2004) 'Functional Efficacy of Tendon Repair Processes', *Annual Review of Biomedical Engineering*, 6(1), pp. 303–329. Available at: https://doi.org/10.1146/annurev.bioeng.6.040803.140240.

Butler, D.L., Kay, M.D. and Stouffer, D.C. (1986) 'Comparison of material properties in fascicle-bone units from human patellar tendon and knee ligaments', *Journal of Biomechanics*, 19(6), pp. 425–432. Available at: https://doi.org/10.1016/0021-9290(86)90019-9.

Chandrashekar, N. *et al.* (2006) 'Sex-based differences in the tensile properties of the human anterior cruciate ligament', *Journal of Biomechanics*, 39(16), pp. 2943–2950. Available at: https://doi.org/10.1016/j.jbiomech.2005.10.031.

Christensen, K.W. *et al.* (2022) 'Assembled Cell-Decorated Collagen (AC-DC) Fiber Bioprinted Implants with Musculoskeletal Tissue Properties Promote Functional Recovery in Volumetric Muscle Loss', *Advanced Healthcare Materials*, 11(3), p. 2101357. Available at: https://doi.org/10.1002/adhm.202101357.

Cittadella Vigodarzere, G. and Mantero, S. (2014) 'Skeletal muscle tissue engineering: strategies for volumetric constructs', *Frontiers in Physiology*, 5. Available at: https://doi.org/10.3389/fphys.2014.00362.

Colvin, A.C. *et al.* (2012) 'National Trends in Rotator Cuff Repair', *JBJS*, 94(3), pp. 227–233. Available at: https://doi.org/10.2106/JBJS.J.00739.

Corona, B.T. *et al.* (2012) 'Further Development of a Tissue Engineered Muscle Repair Construct In Vitro for Enhanced Functional Recovery Following Implantation In Vivo in a Murine Model of Volumetric Muscle Loss Injury', *Tissue Engineering Part A*, 18(11–12), pp. 1213–1228. Available at: https://doi.org/10.1089/ten.tea.2011.0614.

Corona, B.T. *et al.* (2013) 'Autologous minced muscle grafts: a tissue engineering therapy for the volumetric loss of skeletal muscle', *American Journal of Physiology-Cell Physiology*, 305(7), pp. C761–C775. Available at: https://doi.org/10.1152/ajpcell.00189.2013.

Corona, B.T. *et al.* (2014a) 'Implantation of In Vitro Tissue Engineered Muscle Repair Constructs and Bladder Acellular Matrices Partially Restore In Vivo Skeletal Muscle Function in a Rat Model of Volumetric Muscle Loss Injury', *Tissue Engineering Part A*, 20(3–4), pp. 705–715. Available at: https://doi.org/10.1089/ten.tea.2012.0761.

Corona, B.T. *et al.* (2014b) 'Implantation of In Vitro Tissue Engineered Muscle Repair Constructs and Bladder Acellular Matrices Partially Restore In Vivo Skeletal Muscle Function in a Rat Model of Volumetric Muscle Loss Injury', *Tissue Engineering Part A*, 20(3–4), pp. 705–715. Available at: https://doi.org/10.1089/ten.tea.2012.0761.

Corona, B.T. *et al.* (2015) 'Volumetric muscle loss leads to permanent disability following extremity trauma', *Journal of Rehabilitation Research and Development*, 52(7), pp. 785–792. Available at: https://doi.org/10.1682/JRRD.2014.07.0165.

Corona, B.T., Rivera, J.C. and Greising, S.M. (2018) 'Inflammatory and Physiological Consequences of Debridement of Fibrous Tissue after Volumetric Muscle Loss Injury', *Clinical and Translational Science*, 11(2), pp. 208–217. Available at: https://doi.org/10.1111/cts.12519.

Covey, D.C. (2002) 'Blast and Fragment Injuries of the Musculoskeletal System', *JBJS*, 84(7), pp. 1221–1234.

Dasgupta, A. *et al.* (2021) 'Comprehensive collagen crosslinking comparison of microfluidic wet-extruded microfibers for bioactive surgical suture development', *Acta Biomaterialia*, p. S1742706121002658. Available at: https://doi.org/10.1016/j.actbio.2021.04.028.

Dyer, S.E. *et al.* (2022) 'Administration of particulate oxygen generators improves skeletal muscle contractile function after ischemia-reperfusion injury in the rat hindlimb', *Journal of Applied Physiology*, 132(2), pp. 541–552. Available at: https://doi.org/10.1152/japplphysiol.00259.2021.

Eckenrode, B.J. *et al.* (2017) 'Prevention and Management of Post-operative Complications Following ACL Reconstruction', *Current Reviews in Musculoskeletal Medicine*, 10(3), pp. 315–321. Available at: https://doi.org/10.1007/s12178-017-9427-2.

Fadia, N.B. *et al.* (2020) 'Long-gap peripheral nerve repair through sustained release of a neurotrophic factor in nonhuman primates', *Science Translational Medicine*, 12(527), p. eaav7753. Available at: https://doi.org/10.1126/scitranslmed.aav7753.

Foolen, J. *et al.* (2018) 'Tissue alignment enhances remodeling potential of tendon-derived cells - Lessons from a novel microtissue model of tendon scarring', *Matrix Biology*, 65, pp. 14–29. Available at: https://doi.org/10.1016/j.matbio.2017.06.002.

Fu, S.Y. and Gordon, T. (1995) 'Contributing factors to poor functional recovery after delayed nerve repair: prolonged denervation', *Journal of Neuroscience*, 15(5), pp. 3886–3895. Available at: https://doi.org/10.1523/JNEUROSCI.15-05-03886.1995.

Fuoco, C. *et al.* (2016) 'Matrix scaffolding for stem cell guidance toward skeletal muscle tissue engineering', *Journal of Orthopaedic Surgery and Research*, 11(1), p. 86. Available at: https://doi.org/10.1186/s13018-016-0421-y.

Garg, K. *et al.* (2015a) 'Volumetric muscle loss: persistent functional deficits beyond frank loss of tissue', *Journal of Orthopaedic Research: Official Publication of the Orthopaedic Research Society*, 33(1), pp. 40–46. Available at: https://doi.org/10.1002/jor.22730.

Garg, K. *et al.* (2015b) 'Volumetric muscle loss: Persistent functional deficits beyond frank loss of tissue', *Journal of Orthopaedic Research*, 33(1), pp. 40–46. Available at: https://doi.org/10.1002/jor.22730.

Garg, K., Corona, B.T. and Walters, T.J. (2015) 'Therapeutic strategies for preventing skeletal muscle fibrosis after injury', *Frontiers in Pharmacology*, 6. Available at: https://www.frontiersin.org/articles/10.3389/fphar.2015.00087 (Accessed: 31 October 2022).

Gentleman, E. *et al.* (2003) 'Mechanical characterization of collagen fibers and scaffolds for tissue engineering', *Biomaterials*, 24(21), pp. 3805–3813. Available at: https://doi.org/10.1016/S0142-9612(03)00206-0.

Gentleman, E. *et al.* (2006) 'Development of Ligament-Like Structural Organization and Properties in Cell-Seeded Collagen Scaffolds in vitro', *Annals of Biomedical Engineering*, 34(5), pp. 726–736. Available at: https://doi.org/10.1007/s10439-005-9058-4.

Grasman, J.M. *et al.* (2015) 'Biomimetic scaffolds for regeneration of volumetric muscle loss in skeletal muscle injuries', *Acta Biomaterialia*, 25, pp. 2–15. Available at: https://doi.org/10.1016/j.actbio.2015.07.038.

Greising, S.M., Dearth, C.L. and Corona, B.T. (2016) 'Regenerative and Rehabilitative Medicine: A Necessary Synergy for Functional Recovery from Volumetric Muscle Loss Injury', *Cells Tissues Organs*, 202(3–4), pp. 237–249. Available at: https://doi.org/10.1159/000444673.

Grogan, B.F., Hsu, J.R. and Consortium, S.T.R. (2011a) 'Volumetric Muscle Loss', *JAAOS - Journal of the American Academy of Orthopaedic Surgeons*, 19, p. S35.

Grogan, B.F., Hsu, J.R. and Consortium, S.T.R. (2011b) 'Volumetric Muscle Loss', *JAAOS - Journal of the American Academy of Orthopaedic Surgeons*, 19, p. S35.

Han, H., Furst, E.M. and Kim, C. (2014) 'Lagrangian analysis of consecutive images: Quantification of mixing processes in drops moving in a microchannel', *Rheologica Acta*, 53(7), pp. 489–499. Available at: https://doi.org/10.1007/s00397-014-0769-z.

Herchenhan, A. *et al.* (2013) 'In vitro tendon tissue development from human fibroblasts demonstrates collagen fibril diameter growth associated with a rise in mechanical strength', *Developmental Dynamics*, 242(1), pp. 2–8. Available at: https://doi.org/10.1002/dvdy.23896.

Itoi, E. *et al.* (1995) ‘Tensile properties of the supraspinatus tendon’, *Journal of Orthopaedic Research*, 13(4), pp. 578–584. Available at: https://doi.org/10.1002/jor.1100130413.

Jang, K.-M. *et al.* (2015) ‘Efficacy and Safety of Human Umbilical Cord Blood–Derived Mesenchymal Stem Cells in Anterior Cruciate Ligament Reconstruction of a Rabbit Model: New Strategy to Enhance Tendon Graft Healing’, *Arthroscopy: The Journal of Arthroscopic & Related Surgery*, 31(8), pp. 1530–1539. Available at: https://doi.org/10.1016/j.arthro.2015.02.023.

Janssen, I. *et al.* (2000) ‘Skeletal muscle mass and distribution in 468 men and women aged 18–88 yr’, *Journal of Applied Physiology*, 89(1), pp. 81–88. Available at: https://doi.org/10.1152/jappl.2000.89.1.81.

Jiang, X. *et al.* (2020) ‘3D printing of multilayered scaffolds for rotator cuff tendon regeneration’, *Bioactive Materials*, 5(3), pp. 636–643. Available at: https://doi.org/10.1016/j.bioactmat.2020.04.017.

Juhas, M. and Bursac, N. (2013) ‘Engineering skeletal muscle repair’, *Current Opinion in Biotechnology*, 24(5), pp. 880–886. Available at: https://doi.org/10.1016/j.copbio.2013.04.013.

Juhas, M., Ye, J. and Bursac, N. (2016) ‘Design, evaluation, and application of engineered skeletal muscle’, *Methods*, 99, pp. 81–90. Available at: https://doi.org/10.1016/j.ymeth.2015.10.002.

Kaiser, N.J. *et al.* (2019) ‘Digital Design and Automated Fabrication of Bespoke Collagen Microfiber Scaffolds’, *Tissue Engineering Part C: Methods*, 25(11), pp. 687–700. Available at: https://doi.org/10.1089/ten.tec.2018.0379.

Kishore, V. *et al.* (2012) ‘TENOGENIC DIFFERENTIATION OF HUMAN MSCs INDUCED BY THE TOPOGRAPHY OF ELECTROCHEMICALLY ALIGNED COLLAGEN THREADS’, *Biomaterials*, 33(7), pp. 2137–2144. Available at: https://doi.org/10.1016/j.biomaterials.2011.11.066.

Kokai, L.E. *et al.* (2011) 'Sustained Growth Factor Delivery Promotes Axonal Regeneration in Long Gap Peripheral Nerve Repair', *Tissue Engineering Part A*, 17(9–10), pp. 1263–1275. Available at: https://doi.org/10.1089/ten.tea.2010.0507.

Kokai, L.E., Ghaznavi, A.M. and Marra, K.G. (2010) 'Incorporation of double-walled microspheres into polymer nerve guides for the sustained delivery of glial cell line-derived neurotrophic factor', *Biomaterials*, 31(8), pp. 2313–2322. Available at: https://doi.org/10.1016/j.biomaterials.2009.11.075.

Lee, S.Y. *et al.* (2017) 'Therapeutic Mechanisms of Human Adipose-Derived Mesenchymal Stem Cells in a Rat Tendon Injury Model', *The American Journal of Sports Medicine*, 45(6), pp. 1429–1439. Available at: https://doi.org/10.1177/0363546517689874.

Li, C. and Cui, W. (2021) '3D bioprinting of cell-laden constructs for regenerative medicine', *Engineered Regeneration*, 2, pp. 195–205. Available at: https://doi.org/10.1016/j.engreg.2021.11.005.

Liberski, A.R. *et al.* (2011) 'Organ Weaving: Woven Threads and Sheets As a Step Towards a New Strategy for Artificial Organ Development: Organ Weaving: Woven Threads and Sheets As a Step Towards …', *Macromolecular Bioscience*, 11(11), pp. 1491–1498. Available at: https://doi.org/10.1002/mabi.201100086.

Liu, J. *et al.* (2018a) 'Current Methods for Skeletal Muscle Tissue Repair and Regeneration', *BioMed Research International*, 2018, p. e1984879. Available at: https://doi.org/10.1155/2018/1984879.

Liu, J. *et al.* (2018b) 'Current Methods for Skeletal Muscle Tissue Repair and Regeneration', *BioMed Research International*, 2018, p. e1984879. Available at: https://doi.org/10.1155/2018/1984879.

Maghdouri-White, Y. *et al.* (2020) 'Biomanufacturing organized collagen-based microfibers as a Tissue ENgineered Device (TEND) for tendon regeneration', *Biomedical Materials* [Preprint]. Available at: https://doi.org/10.1088/1748-605X/abb875.

Mandrycky, C. *et al.* (2016) '3D bioprinting for engineering complex tissues', *Biotechnology Advances*, 34(4), pp. 422–434. Available at: https://doi.org/10.1016/j.biotechadv.2015.12.011.

Mauck, R.L. *et al.* (2009) 'Engineering on the Straight and Narrow: The Mechanics of Nanofibrous Assemblies for Fiber-Reinforced Tissue Regeneration', *Tissue Engineering Part B: Reviews*, 15(2), pp. 171–193. Available at: https://doi.org/10.1089/ten.teb.2008.0652.

Merceron, T.K. *et al.* (2015) 'A 3D bioprinted complex structure for engineering the muscle–tendon unit', *Biofabrication*, 7(3), p. 035003. Available at: https://doi.org/10.1088/1758-5090/7/3/035003.

Mertens, J.P. *et al.* (2014) 'Engineering muscle constructs for the creation of functional engineered musculoskeletal tissue', *Regenerative Medicine*, 9(1), pp. 89–100. Available at: https://doi.org/10.2217/rme.13.81.

Mintz, E.L. *et al.* (2016) 'Applications of In Vivo Functional Testing of the Rat Tibialis Anterior for Evaluating Tissue Engineered Skeletal Muscle Repair', *Journal of Visualized Experiments : JoVE*, (116), p. 54487. Available at: https://doi.org/10.3791/54487.

Mintz, E.L. *et al.* (2020a) 'Long-Term Evaluation of Functional Outcomes Following Rat Volumetric Muscle Loss Injury and Repair', *Tissue Engineering Part A*, 26(3–4), pp. 140–156. Available at: https://doi.org/10.1089/ten.tea.2019.0126.

Mintz, E.L. *et al.* (2020b) 'Long-Term Evaluation of Functional Outcomes Following Rat Volumetric Muscle Loss Injury and Repair', *Tissue Engineering Part A*, 26(3–4), pp. 140–156. Available at: https://doi.org/10.1089/ten.tea.2019.0126.

Moimas, S. *et al.* (2013) 'Effect of vascular endothelial growth factor gene therapy on post-traumatic peripheral nerve regeneration and denervation-related muscle atrophy', *Gene Therapy*, 20(10), pp. 1014–1021. Available at: https://doi.org/10.1038/gt.2013.26.

Murphy, S.V. and Atala, A. (2014) '3D bioprinting of tissues and organs', *Nature Biotechnology*, 32(8), pp. 773–785. Available at: https://doi.org/10.1038/nbt.2958.

Murphy, S.V., De Coppi, P. and Atala, A. (2020a) 'Opportunities and challenges of translational 3D bioprinting', *Nature Biomedical Engineering*, 4(4), pp. 370–380. Available at: https://doi.org/10.1038/s41551-019-0471-7.

Murphy, S.V., De Coppi, P. and Atala, A. (2020b) 'Opportunities and challenges of translational 3D bioprinting', *Nature Biomedical Engineering*, 4(4), pp. 370–380. Available at: https://doi.org/10.1038/s41551-019-0471-7.

Ngan, C. *et al.* (2017) 'Engineering skeletal muscle - from two to three dimensions', *Australian Institute for Innovative Materials - Papers*, pp. 1–6. Available at: https://doi.org/10.1002/term.2265.

Novakova, S.S. *et al.* (2017) 'Tissue-engineered tendon constructs for rotator cuff repair in sheep: ENGINEERED TENDON ROTATOR CUFF REPAIR', *Journal of Orthopaedic Research* [Preprint]. Available at: https://doi.org/10.1002/jor.23642.

Noyes, F. and Grood, E. (1976) 'The strength of the anterior cruciate ligament in humans and Rhesus monkeys':, *The Journal of Bone & Joint Surgery*, 58(8), pp. 1074–1082. Available at: https://doi.org/10.2106/00004623-197658080-00006.

Ober, T.J., Foresti, D. and Lewis, J.A. (2015) 'Active mixing of complex fluids at the microscale', *Proceedings of the National Academy of Sciences*, 112(40), pp. 12293–12298. Available at: https://doi.org/10.1073/pnas.1509224112.

O'Keefe, Regis J *et al.* (2020) 'American Society for Bone and Mineral Research-Orthopaedic Research Society Joint Task Force Report on Cell-Based Therapies', *Journal of Bone and Mineral Research*, 35(1), pp. 3–17. Available at: https://doi.org/10.1002/jbmr.3839.

O'Keefe, Regis J. *et al.* (2020) 'American Society for Bone and Mineral Research-Orthopaedic Research Society Joint Task Force Report on Cell-Based Therapies – Secondary Publication', *Journal of Orthopaedic Research*, 38(3), pp. 485–502. Available at: https://doi.org/10.1002/jor.24485.

Passipieri, J. a. *et al.* (2017) 'Keratin Hydrogel Enhances In Vivo Skeletal Muscle Function in a Rat Model of Volumetric Muscle Loss', *Tissue Engineering Part A*, 23(11–12), pp. 556–571. Available at: https://doi.org/10.1089/ten.tea.2016.0458.

Passipieri, J.A. *et al.* (2017) 'Keratin Hydrogel Enhances In Vivo Skeletal Muscle Function in a Rat Model of Volumetric Muscle Loss', *Tissue Engineering. Part A*, 23(11–12), pp. 556–571. Available at: https://doi.org/10.1089/ten.tea.2016.0458.

Passipieri, J.A. *et al.* (2019a) 'In Silico and In Vivo Studies Detect Functional Repair Mechanisms in a Volumetric Muscle Loss Injury', *Tissue Engineering Part A*, 25(17–18), pp. 1272–1288. Available at: https://doi.org/10.1089/ten.tea.2018.0280.

Passipieri, J.A. *et al.* (2019b) 'In Silico and In Vivo Studies Detect Functional Repair Mechanisms in a Volumetric Muscle Loss Injury', *Tissue Engineering Part A*, 25(17–18), pp. 1272–1288. Available at: https://doi.org/10.1089/ten.tea.2018.0280.

Passipieri, J.A. *et al.* (2021) 'Adipose Stem Cells Enhance Nerve Regeneration and Muscle Function in a Peroneal Nerve Ablation Model', *Tissue Engineering Part A*, 27(5–6), pp. 297–310. Available at: https://doi.org/10.1089/ten.tea.2018.0244.

Passipieri, J.A. and Christ, G.J. (2016) 'The Potential of Combination Therapeutics for More Complete Repair of Volumetric Muscle Loss Injuries: The Role of Exogenous Growth Factors and/or Progenitor Cells in Implantable Skeletal Muscle Tissue Engineering Technologies', *Cells Tissues Organs*, 202(3–4), pp. 202–213. Available at: https://doi.org/10.1159/000447323.

Pittenger, M.F. *et al.* (1999) 'Multilineage Potential of Adult Human Mesenchymal Stem Cells', *Science*, 284(5411), pp. 143–147. Available at: https://doi.org/10.1126/science.284.5411.143.

Puetzer, J.L. and Bonassar, L.J. (2016) 'Physiologically Distributed Loading Patterns Drive the Formation of Zonally Organized Collagen Structures in Tissue-Engineered Meniscus', *Tissue Engineering Part A*, 22(13–14), pp. 907–916. Available at: https://doi.org/10.1089/ten.tea.2015.0519.

Qazi, T.H. *et al.* (2015) 'Biomaterials based strategies for skeletal muscle tissue engineering: Existing technologies and future trends', *Biomaterials*, 53, pp. 502–521. Available at: https://doi.org/10.1016/j.biomaterials.2015.02.110.

Sahoo, S., Cho-Hong, J.G. and Siew-Lok, T. (2007) 'Development of hybrid polymer scaffolds for potential applications in ligament and tendon tissue engineering', *Biomedical Materials*, 2(3), pp. 169–173. Available at: https://doi.org/10.1088/1748-6041/2/3/001.

Seon, J.K., Song, E.K. and Park, S.J. (2006a) 'Osteoarthritis after anterior cruciate ligament reconstruction using a patellar tendon autograft', *International Orthopaedics*, 30(2), pp. 94–98. Available at: https://doi.org/10.1007/s00264-005-0036-0.

Seon, J.K., Song, E.K. and Park, S.J. (2006b) 'Osteoarthritis after anterior cruciate ligament reconstruction using a patellar tendon autograft', *International Orthopaedics*, 30(2), pp. 94–98. Available at: https://doi.org/10.1007/s00264-005-0036-0.

Sheean, A.J., Dickens, J.F. and Provencher, M.T. (2021) 'Extremity War Injury Symposium XV: Sports and Readiness Symposium Summary', *The Journal of the American Academy of Orthopaedic Surgeons* [Preprint]. Available at: https://doi.org/10.5435/JAAOS-D-20-00930.

Shin, Y.K. *et al.* (2018) 'Predictive Factors of Retear in Patients With Repaired Rotator Cuff Tear on Shoulder MRI', *American Journal of Roentgenology*, 210(1), pp. 134–141. Available at: https://doi.org/10.2214/AJR.17.17915.

Smith, L.R. and Barton, E.R. (2014a) 'SMASH – semi-automatic muscle analysis using segmentation of histology: a MATLAB application', *Skeletal Muscle*, 4(1), p. 21. Available at: https://doi.org/10.1186/2044-5040-4-21.

Smith, L.R. and Barton, E.R. (2014b) 'SMASH – semi-automatic muscle analysis using segmentation of histology: a MATLAB application', *Skeletal Muscle*, 4(1), p. 21. Available at: https://doi.org/10.1186/2044-5040-4-21.

Tamayol, A. *et al.* (2013) 'Fiber-based tissue engineering: Progress, challenges, and opportunities', *Biotechnology Advances*, 31(5), pp. 669–687. Available at: https://doi.org/10.1016/j.biotechadv.2012.11.007.

Taylor, K.A. *et al.* (2013) 'In vivo measurement of ACL length and relative strain during walking', *Journal of Biomechanics*, 46(3), pp. 478–483. Available at: https://doi.org/10.1016/j.jbiomech.2012.10.031.

Turner, N.J. and Badylak, S.F. (2012) 'Regeneration of skeletal muscle', *Cell and Tissue Research*, 347(3), pp. 759–774. Available at: https://doi.org/10.1007/s00441-011-1185-7.

Walters, V.I., Kwansa, A.L. and Freeman, J.W. (2012) 'Design and Analysis of Braid-Twist Collagen Scaffolds', *Connective Tissue Research*, 53(3), pp. 255–266. Available at: https://doi.org/10.3109/03008207.2011.634532.

Wang, J.H.-C. *et al.* (2003) 'Cell orientation determines the alignment of cell-produced collagenous matrix', *Journal of Biomechanics*, 36(1), pp. 97–102. Available at: https://doi.org/10.1016/S0021-9290(02)00233-6.

Westman, A.M. *et al.* (2021) 'Agent-based model provides insight into the mechanisms behind failed regeneration following volumetric muscle loss injury', *PLOS Computational Biology*, 17(5), p. e1008937. Available at: https://doi.org/10.1371/journal.pcbi.1008937.

Wolf, M.T. *et al.* (2015) 'Naturally derived and synthetic scaffolds for skeletal muscle reconstruction', *Advanced Drug Delivery Reviews*, 84, pp. 208–221. Available at: https://doi.org/10.1016/j.addr.2014.08.011.

Wu, Y. *et al.* (2017) 'Direct E-jet printing of three-dimensional fibrous scaffold for tendon tissue engineering: DIRECT E-JET PRINTING OF SCAFFOLD FOR TENDON TISSUE ENGINEERING', *Journal of Biomedical Materials Research Part B: Applied Biomaterials*, 105(3), pp. 616–627. Available at: https://doi.org/10.1002/jbm.b.33580.

Zhang, J. *et al.* (2015) 'The challenges and promises of allogeneic mesenchymal stem cells for use as a cell-based therapy', *Stem Cell Research & Therapy*, 6(1), p. 234. Available at: https://doi.org/10.1186/s13287-015-0240-9.

Acknowledgments: The authors wish to thank P. Sharma, N. Kemper, and N. Sori for their contributions and efforts.

Funding: The work was funded in part by the MRDC (US ARMY), grant W81XWH1910475), Defense Advanced Research Projects Agency (DARPA, grant HR0011-15-9-0006, AFWERX FA8649-20-9-9080, and Virginia Catalyst (Principal Investigator: Michael Francis for all awards). Opinions, interpretations, conclusions, and recommendations are those of the authors and are not necessarily endorsed by respective funding agencies.

Author contributions: KWC performed AC-DC bioprinting conceptualization and design, implant fabrication, cell viability/directionality/distribution analysis, mechanical property testing, data analysis related to *in vitro* analysis, and contributed to manuscript preparation. JT performed animal surgeries and care, functional testing, immunohistochemistry, SMASH analysis, data analysis related to *in vivo* analysis, and contributed to manuscript preparation. KC assisted with implant fabrication and *in vitro* analysis. YM and AB assisted with *in vitro* analysis. OS and MR assisted with developing SMASH protocols. AR assisted with SMASH analysis. AS contributed to manuscript preparation. GJC provided project guidance and contributed to manuscript preparation. MPF provided funding, project guidance, AC-DC bioprinting conceptualization, and contributed to manuscript preparation.

Competing interests: Authors KWC, KC, YM and MPF declare that they are or were employees and/or shareholders of Embody Inc. Patents pertaining to some aspects of this work are pending. Other authors declare that they have no competing interests.

Data and materials availability: Materials described in this article may be available through material transfer agreements with the authors and their respective affiliations.

END of previously published material.

(3.3) Further Conclusions and Future Directions

The results of this chapter are highly promising and show great potential for AC-DC scaffolds as a means of VML and polytrauma repair. Future work in this area could be focused on the introduction of multiple architectures within a single scaffold. One region specifically designed with intent of regenerating muscle tissue and one region with the intent of regenerating tendon tissue. The

interface of these two scaffold architectures may be the biggest challenge to overcome and would be a next step of research. By varying the mechanical properties of the fibers and cell types bioprinted onto the scaffold surface, multiple regions could easily be fabricated. Having shown success already for the regeneration of a VML injury and the capability to proliferate and mature tenocytes, this novel microfiber collagen scaffold seems ideal for the continuation of these studies.

Chapter 4: Further Development of Peroneal Nerve Injury Models for Evaluation of Polytraumatic Volumetric Muscle Loss Injuries

The following chapter has been submitted for publication. A preface and conclusion have been added for this work to place it in the greater context of the overall work of this dissertation but has otherwise been included exactly as submitted.

(4.1) Preface

Volumetric muscle loss and polytrauma injuries often result in denervation of muscle tissue causing further atrophy of tissue from the original injury. The length of time for axonal growth is in the range of three months, which can take too long for the muscle tissue to become reinnervated before losing its native capacity to regenerate. Therefore, it is essential to address polytrauma injuries by improving axonal growth and shortening the time of reinnervation. To achieve improved functional recovery following a peripheral nerve injury, reducing the time of reinnervation is key to success (Moimas *et al.*, 2013).

To further our understanding of polytraumatic injuries in relationship to VML, we wanted to identify a nerve injury model that causes denervation based functional deficit in the tibialis anterior, while remaining capable of functional repair. Previous work by others in our lab laid the framework for this chapter by assessing a complete peroneal nerve ablation injury model. The study involved a 6mm nerve ablation receiving PCL based conduits with or without ASCs for repair. This resulted in little return to function at 12 weeks post repair in any groups. This study revealed that such an injury to the nerve created an unrecoverable functional deficit in the tissue, in which the denervation induced atrophy exceeded current VML injury models to the TA itself with no repair. This led us to design the study found in this chapter, to evaluate the functional recovery of rat TA following partial nerve laceration while receiving no repair or a nerve guide conduit with GDNF containing

microspheres over 12 weeks. The results have been compiled into a manuscript submitted for publication, which can be found in its entirety here.

The following manuscript has been submitted for approval and is awaiting publication as of December 2022. The work submitted was done in collaboration with the University of Pittsburgh, Department of Bioengineering. Special thanks to Kacey Marra, Baris Bengur, and Michael Rariden for their collaboration and contributions.

(4.2)

Further Development of Peroneal Nerve Injury Models For Evaluation of Polytraumatic Volumetric Muscle Loss Injuries

Authors: Jonathan Turner[1], Michael Rariden[1], Fuat Baris Bengur[3], Juliana Passipieri[1], Jack Dienes[1], Godwin Oluwafemi[1], Kunaal Agarwal[1], Kacey Marra[3,4‡], George J. Christ[1,2‡*]

Affiliations:

[1]Department of Biomedical Engineering, University of Virginia; Charlottesville, Virginia, USA.

[2]Department of Orthopaedic Surgery, University of Virginia; Charlottesville, Virginia, USA.

[3]Department of Bioengineering, University of Pittsburgh; Pittsburgh, PA, USA.

[4]Department of Plastic Surgery, University of Pittsburgh; Pittsburgh, PA, USA.

‡ Senior authors.

* Corresponding author. Email: gjc8w@virginia.edu

Keywords: Polytrauma, Injury Model, Nerve Regeneration, Tissue Engineering, Peripheral Nerve, Volumetric Muscle Loss, Conduit.

Abstract: Despite the fact that many traumatic injuries affect multiple tissue components, research is often, for mechanistic clarity, focused on recovery of one specific tissue type. As a first step toward developing improved preclinical models to more completely address functional recovery from co-incident nerve and muscle polytrauma, we further evaluated an established in vivo rodent peripheral nerve injury model. Specifically, a recoverable, partial transection to the peroneal nerve, was surgically created with and without repair via a polycaprolactone (PCL) nerve guide conduit. Functional recovery of tibialis anterior muscle contraction was measured by stimulation of the peroneal nerve every 4 weeks out to 12 weeks. The surgically implanted nerve conduit neither improved nor hindered the rate or magnitude of functional recovery. Histological and morphological examination of the retrieved TA muscle and peroneal nerve tissues revealed similar fiber counts and fiber sizes between the non-repaired control and PCL-treated groups. This study extends prior work and sheds important insight on the intrinsic complexity of VML polytraumic (simultaneous injury to nerve and muscle) injuries and repair. Moreover, it further highlights the importance of establishing the high-throughput and biologically-relevant animal models that are necessary to provide, in a cost-effective manner, the data and mechanistic understanding needed to develop novel regenerative therapeutics for improved functional outcomes from VML polytrauma.

(4) 1. Introduction

Traumatic skeletal muscle injuries are characterized by simultaneous loss of multiple tissue components, including muscle fibers, nerves, vessels, and extracellular matrix (ECM).(Mintz *et al.*, 2020a). Many skeletal muscle injuries retain an innate capability for effective wound healing. However, when the volume of muscle tissue loss exceeds the regenerative capacity of endogenous mechanisms (Grogan, Hsu and Consortium, 2011; Garg *et al.*, 2015), the injuries are referred to as volumetric muscle loss (VML) injuries. VML injuries are thus defined by permanent functional and cosmetic deficits. (Garg, Corona and Walters, 2015) Furthermore, there is currently no treatment capable of satisfactorily restoring skeletal muscle form and function following VML extremity trauma. Not surprisingly, there has been extensive research conducted into developing improved therapeutics for repair of VML injury. In fact, recent studies indicate that the mechanistic basis for the degree of functional recovery currently possible, may be accounted for, at least in part, by corresponding reclamation of muscle fiber number and cross sectional area (Fu and Gordon, 1995; Corona *et al.*, 2012, 2014b; Christensen *et al.*, 2022)

However, as encouraging as these findings may be, it is important to keep in mind that significant peripheral nerve damage frequently attends trauma-related VML injury. Such injuries are polytraumatic in nature and are accompanied by attenuated regenerative potential (Greising, Dearth and Corona, 2016). In this clinical scenario, peripheral nerve damage causes disruption of nerve fibers and Wallerian degeneration, leading to a progressive breakdown of the distal end of nerve fibers and disruption of the neuromuscular junction(s)/synapses within the target muscle. Because the simultaneous loss of nerve and muscle tissue exacerbates the functional recovery process, restoration of neuronal integrity must be included in any therapeutic strategy for complete functional recovery from polytrauma.

An absolute prerequisite to achieving more complete functional recovery from polytrauma is development of a preclinical nerve injury model(s) that can meet (at least) the following criteria: 1) provide sufficient nerve damage to a target muscle to elicit physiologically relevant atrophy and loss of contractile force, and yet, 2) be sufficiently reproducible and recoverable to permit therapeutic intervention and improved functional recovery of VML. In fact, previous research from our group documented the irrecoverable nature of a peripheral nerve injury created by surgically ablating 6 mm of the common peroneal nerve in a rat model (Passipieri *et al.*, 2021). That study compared the time course of functional recovery of contractile force in the tibialis anterior (TA) muscle following surgical creation of a 6mm nerve gap. More specifically, nerve repair with a PCL-based nerve guide filled with adipose derived stem cells and/or poloxamer hydrogel was compared to the current gold standard, a reverse polarity autograft—a non-repaired nerve injury group run in parallel.

More specifically, 12 weeks post-injury, in all treatment groups, even in those animals receiving "gold standard" nerve repair, the 6 mm nerve gap injury produced a degree of atrophy-related muscle volume loss (≈40%) with an accompanying functional deficit of ≈50%. As a point of reference, both the volume of muscle tissue loss and the functional deficit produced by nerve ablation alone are greater than that observed in a well characterized model of TA VML injury—where we surgically remove ≈20% of the TA muscle, with a corresponding functional deficit of ≈30-40% (at 12 weeks post injury). Such observations point to the complexities of treating polytrauma and served as the driving force behind the current report.

The goal of this study was to begin to optimize/adapt our established and biologically relevant VML injury model for the study of more complex polytrauma and repair. Specifically, we endeavored to identify a substantial and reproducible, yet reversible, rodent peroneal nerve injury model. The establishment of such a model would provide a foundation for future investigations designed to better

assess the complex mechanisms that attend polytraumatic extremity injuries, and eventually, permit development of novel therapeutics that leverage those findings for improved functional recovery.

In this regard, the improved design and fabrication capabilities of polymer-based structures, including integration of neurotrophic factors into these conduits, may provide an opportunity to increase the rate and/or magnitude of functional recovery of muscle following nerve trauma. Previous work by our group has shown that inclusion of, for example, glial cell line-derived neurotrophic factor (GDNF) in the nerve conduit can improve recovery in small and large animal models. (Kokai *et al.*, 2011; Fadia *et al.*, 2020). As such, the long-term goal for use of improved nerve conduits is to accelerate the rate of axonal regeneration within an appropriate timeframe (i.e., 12 weeks) to enable peripheral nerves to enable more complete functional regeneration to muscle. However, we first need to establish the physiological boundary condition for reproducible and reparable nerve injuries. As a first step in that direction, we report herein on our initial observations with partial nerve transection of the peroneal nerve in the absence and presence of treatment with a polymer-based nerve conduit containing subtherapeutic doses of GDNF.

(4) 2. Results

(4) 2.1 Functional Recovery

In vivo studies were conducted over 12 weeks in a rodent model. Two groups were assessed: a control group that received a partial peroneal nerve transection with no repair (NR, n=7), and a treatment group, receiving a nerve conduit loaded with double-walled microspheres containing a subtherapeutic dose of GDNF (NC, n=8). All animals recovered post-surgery, and there were no signs of infection and no deaths. Functional testing was performed *in vivo* prior to creation of peroneal nerve injury, and mean baseline torque values following peroneal nerve stimulation of the TA muscle were

indistinguishable in all animals, which were randomly assigned to either the treated or untreated animal groups (Fig. 1A). In addition, there were no observed differences in body weight over the 12-week time course of study (Fig. 1B). Functional testing was also performed *in vivo* 4, 8, and 12-weeks post-injury and/or repair to assess functional recovery. As shown, mean values were expressed as torque normalized to animal body weight at each time point (N-mm/kg of body weight) to control for increases in torque production due to animal growth (Fig. 1C). No significant differences were seen between the no repair group or the treatment group at any time point. One-way ANOVA with multiple comparisons was used for all statistical analysis in this section.

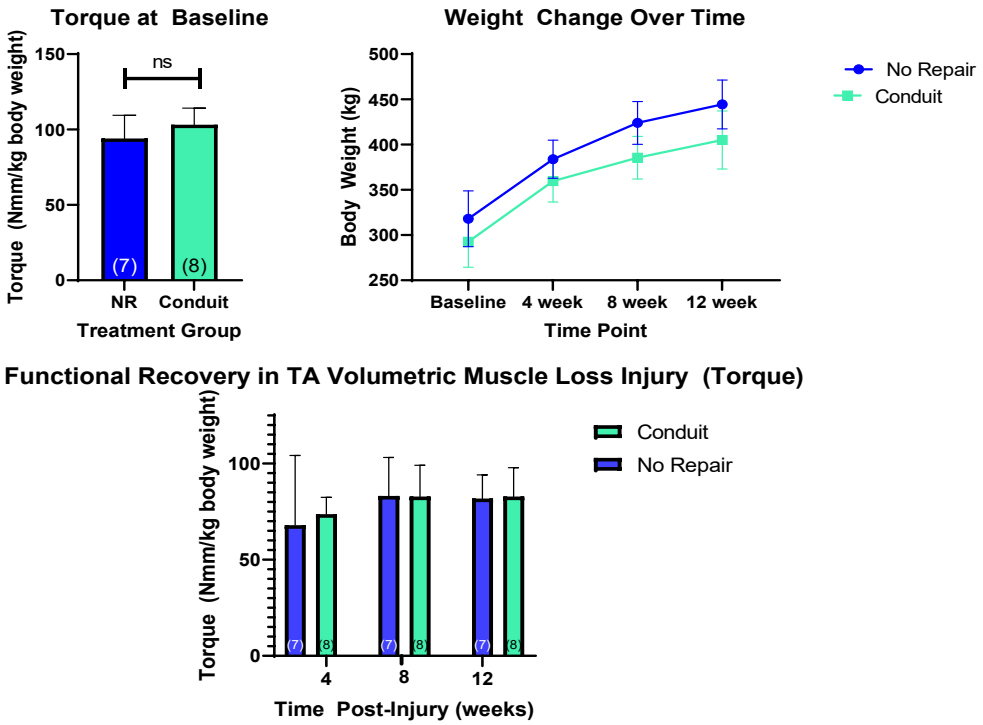

Figure 4-1. Functional Recovery in a Partial Laceration Peroneal Nerve Injury Model – (A) Baseline torque generation pre-injury (p = 0.9, no significant difference). (B) Animal weight pre-injury and at 4, 8, and 12-weeks post-injury, corresponding to functional testing timepoints. (C) Measured

torque at 4, 8, and 12-weeks post-repair, assessing functional recovery facilitated by conduit implantation. (n=7 no repair group and n=8 conduit group, no significance reported for this data).

(4) 2.2 Histological and Morphological Examination of Muscle and Nerve Tissues

Following functional assessment at 12 weeks, isolated TA muscles were collected for morphological and histological examination. Isolated muscles were cross sectioned through the belly of the muscle and processed for hematoxylin and eosin staining (H&E). H&E staining was performed on the no repair and treatment groups as well as the contralateral control TA muscles. Representative images are shown in Figure 2. No significant differences were noted between the three groups in the stained sections or in the gross morphology. Both no repair and treatment groups appeared to maintain similar morphology to the contralateral control and no fibrosis was observed on cross-sections of any group.

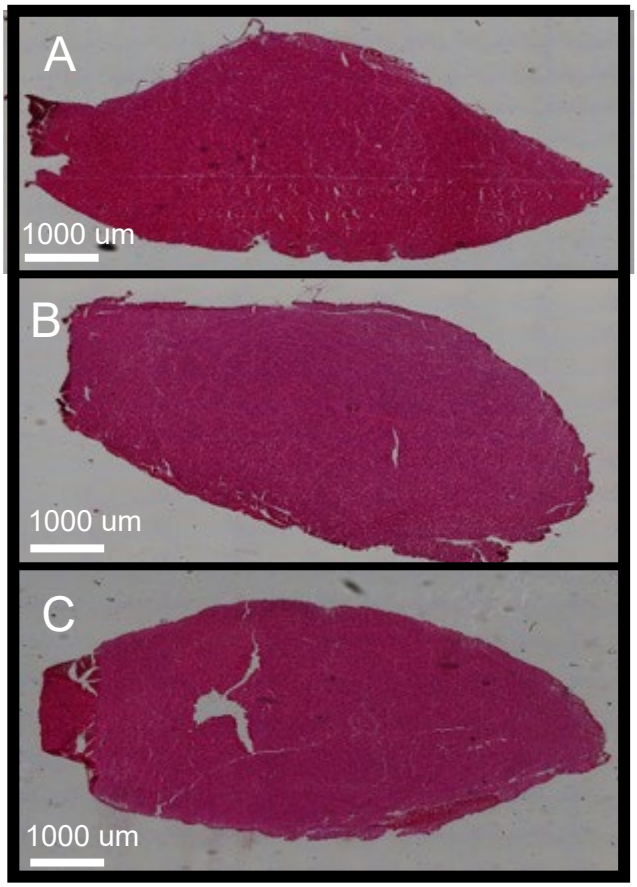

Figure 4-2. Histological assessment of the TA. Representative H&E images of the TA muscle for (**A**) uninjured contralateral control, (**B**) conduit group, (**C**) and no repair group after 12 weeks. All scale bars are 1 mm.

(4) 2.3 Semi-automated Muscle Fiber Analysis (SMASH)

Additional TA muscle sections were processed for further analysis using SMASH, a semi-automated muscle fiber analysis software. Laminin staining identified the outline of muscle fibers throughout sections (Fig. 3A-C) and SMASH analysis allows for individual fiber detection, as illustrated with color segmentation (Fig. 3D-F). For this analysis, the entire area of the tibialis anterior muscle was analyzed. The number of fibers per cross section, median fiber cross sectional area (FCSA), and minimum feret diameter (MFD) were assessed and no significant difference between the contralateral control, no repair, and nerve conduit groups (Fig. 3G) was found. Likewise, the FCSA and MFD showed consistency between the treatment and control groups with no significant differences observed (Fig. 3H-I). Note that median values were used as previously described (Dyer *et al.*, 2022) as the whole FCSA distribution is nonnormal for each muscle. However, when the individual median values are combined for each group, the data are normal, allowing the use of parametric analyses. Brown Forsythe and Welch ANOVA with multiple comparisons was used to analyze the data. The surgically applied conduit showed no noticeable negative response in the muscle tissue analysis.

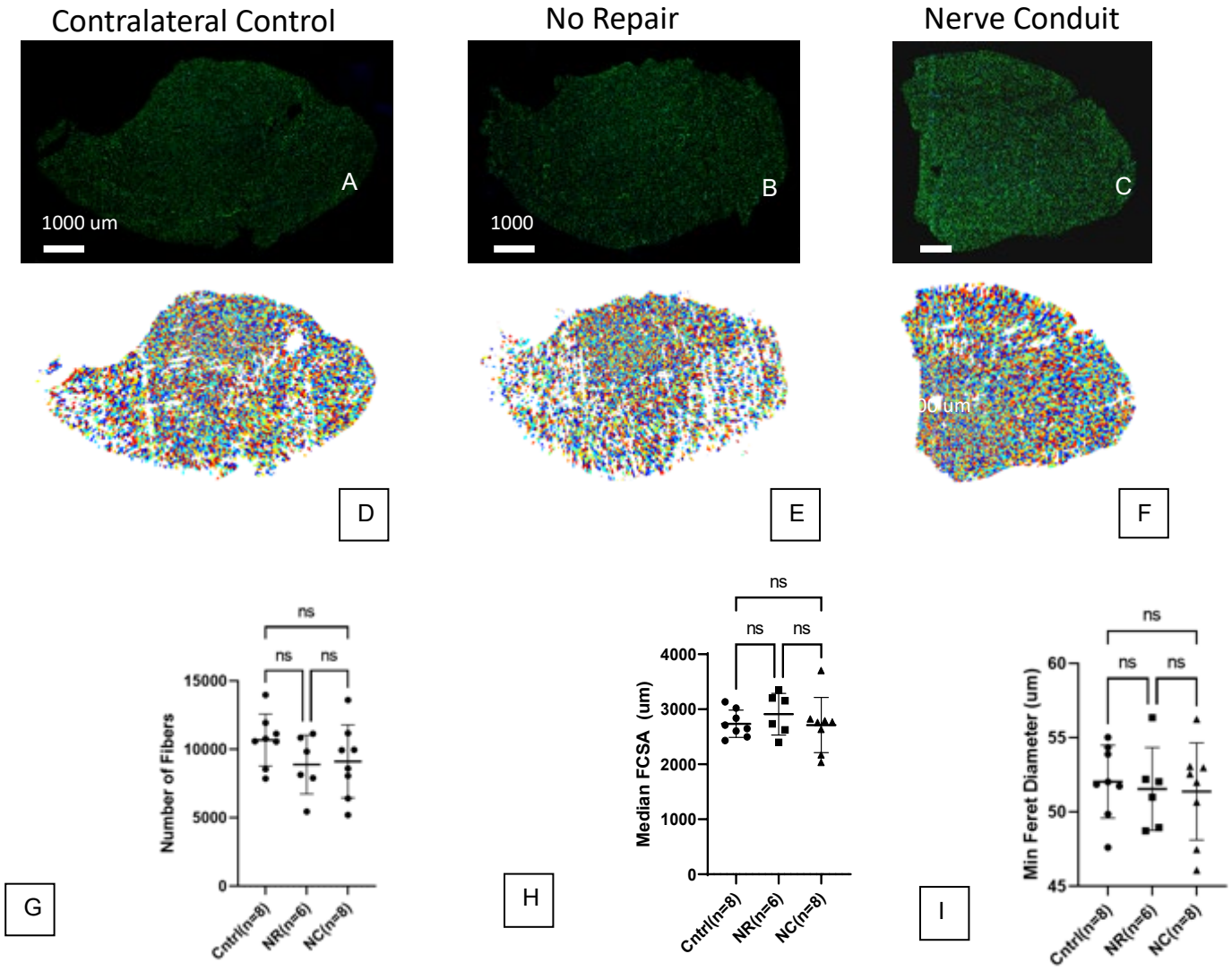

Figure 4-3. Muscle fiber quantification using SMASH. Representative laminin-stained sections of the TA muscle for (**A**) contralateral control, (**B**) no repair, (**C**) nerve conduit groups. (**D-F**) Colorized outputs from the software identifying individual muscle fibers within sections corresponding to (A-C), respectively. (**G**) Total fiber count, (**H**) median fiber cross-sectional area (FCSA), and (**I**) the mean minimum feret diameter for contralateral control (Ctrl), no repair (NR), and nerve conduit (NC) groups. All scale bars are 1 mm. (*p<0.05 indicates significance). Brown-Forsythe and Welch ANOVA test with multiple comparisons was used.

(4) 2.4 Nerve Analysis

Overall, the tissues in both no repair and nerve conduit groups demonstrated similar morphology (Fig. 4), while the use of nerve conduit repair did not affect the morphology of the neural tissues inside the conduit (Fig. 5). The total number of axons as well as the small and large fibers did not differ between groups (Fig. 6A). Despite having similar mean numbers, when the axons were assessed individually for their sizes, the conduit group had a higher portion of smaller-sized regenerating axons compared to the no repair group (Fig. 6B). Mean Schwann cell count between both groups was not significantly different (Fig. 6C).

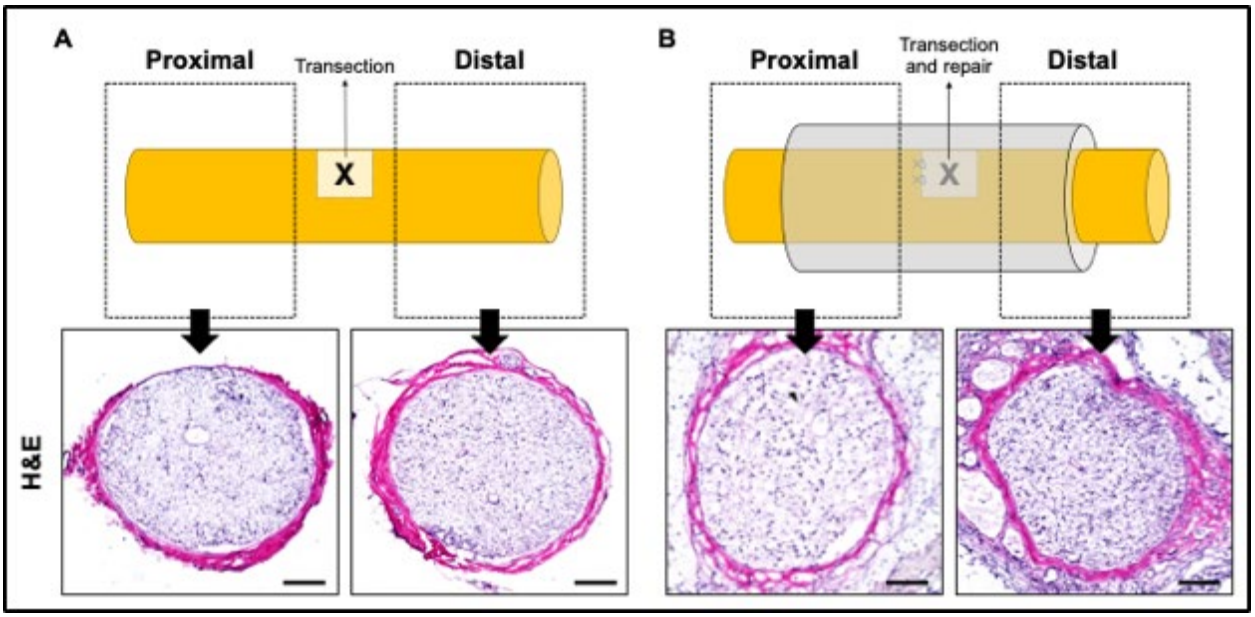

Figure 4-4. Histological assessment of the Nerve. Schematic depiction of representative images of both A) no repair and B) repair with conduit groups and morphology of the neural tissues with H&E stain. Sections from both distal and proximal segments in both groups demonstrated similar structure. All scale bars: 100μm.

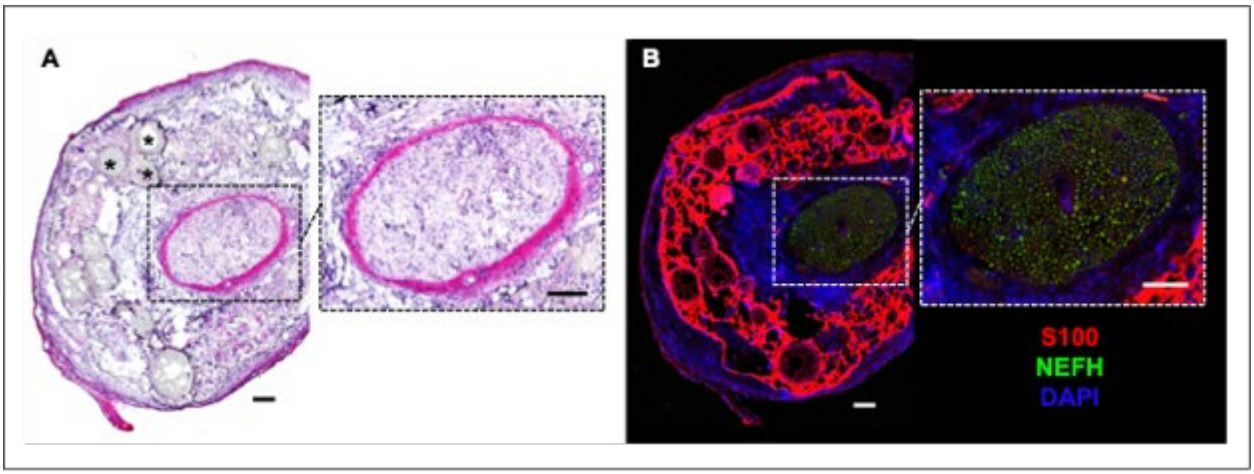

Figure 4-5. Representative Morphology of the Neural Tissues Inside the Nerve Conduit. Segments distal to the repair site are being depicted. A) H&E staining of the nerve inside the nerve conduit in the treatment group with the nerve conduit. Please note the presence of microspheres demonstrated by the stars (*) outside the nerve, within the nerve conduit surrounding the tissue. B) The same tissue demonstrated in A is stained for immunofluorescence microscopy for S100 (red), NEFH (green) and DAPI (blue). All scale bars: 100μm.

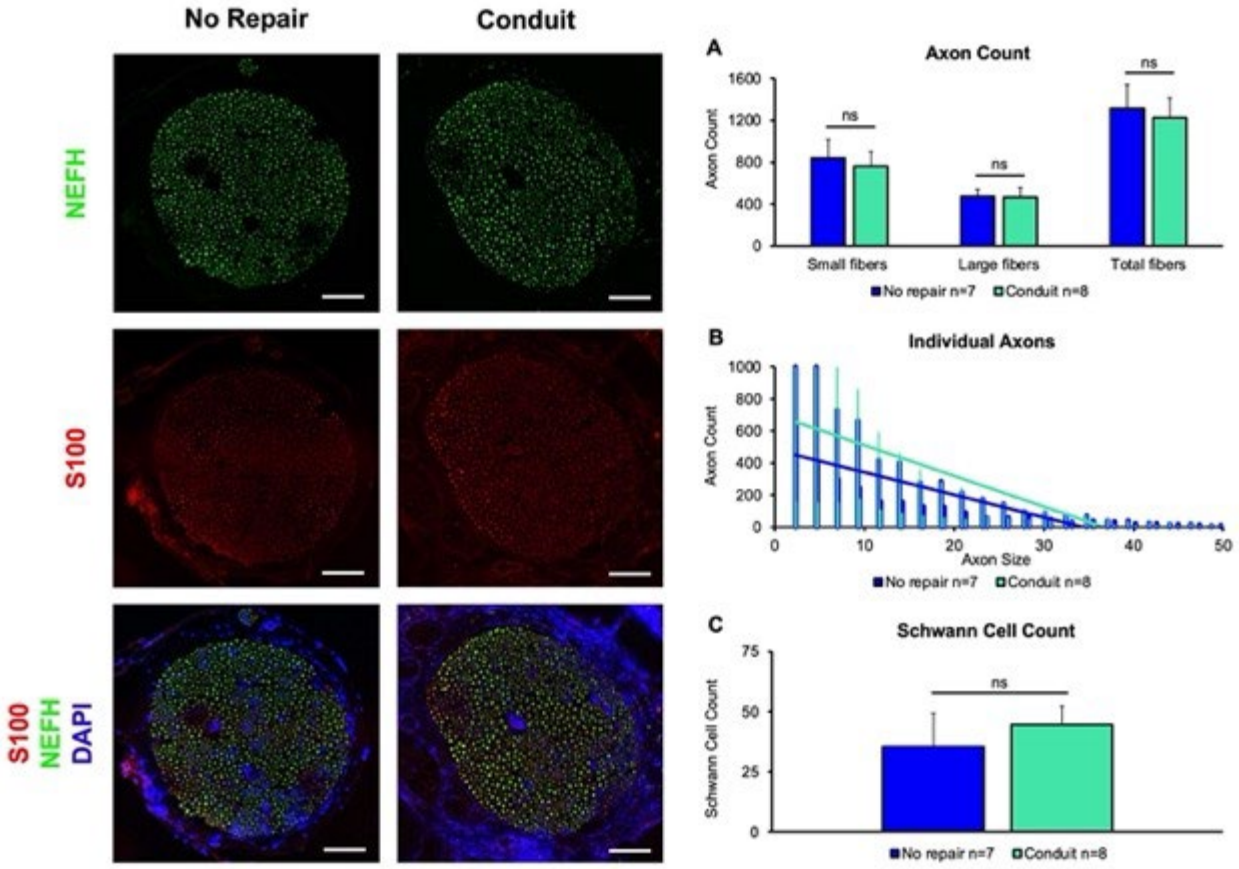

Figure 4-6. Immunofluorescence staining of representative sections of nerve. Samples from both no repair and conduit groups were stained for NEFH (green) for axons, S100 (red) for Schwann cells and DAPI (blue) for nuclei. A) Axon count, B) individual axon sizes (μm^2) and number of axons in each diameter and C) Schwann cell count. Error bars represent standard deviation. Scale bars: 100μm. Ns: not significant, $p>0.05$. Students t-test was used for comparison.

(4) 2.5Kinetic Analysis

Using a previously described equation of fit (see Methods) *k* ('rate') represents a metric of contraction onset magnitude, while *v* ('rapidity') represents the delay to contraction onset. Higher *k* corresponds

to faster force development, and higher *v* corresponds to shorter contraction delay (i.e., faster response).

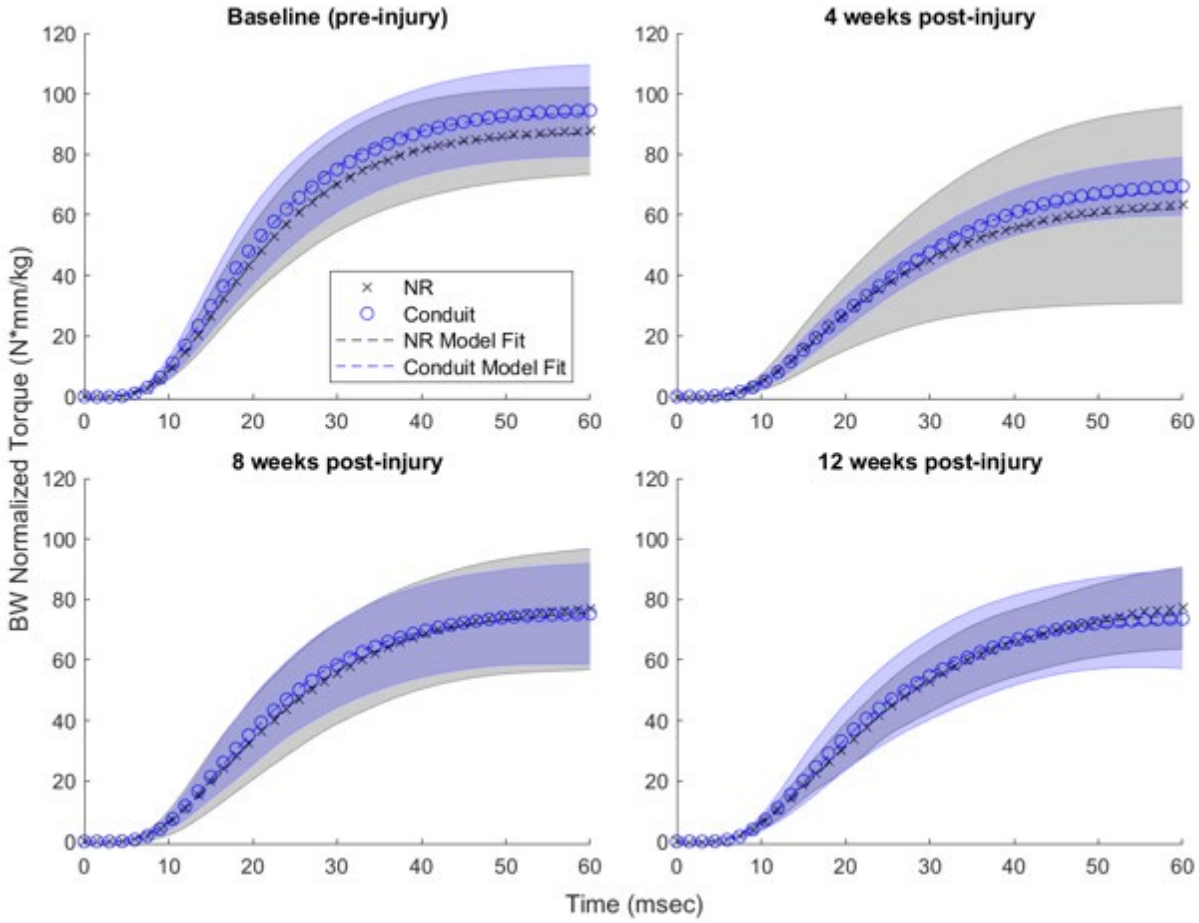

Figure 4-7. **Dynamic torque production from peroneal nerve stimulated contraction.** Torque is shown as mean ± SD, represented by the cloud. The dotted line shows the kinetic model fit to the average torque curve. Since the kinetic model is normalized on [0, 1] vertical and horizontal axes intervals, the model shown is appropriately scaled in torque and time to overlay with the original, unnormalized data.

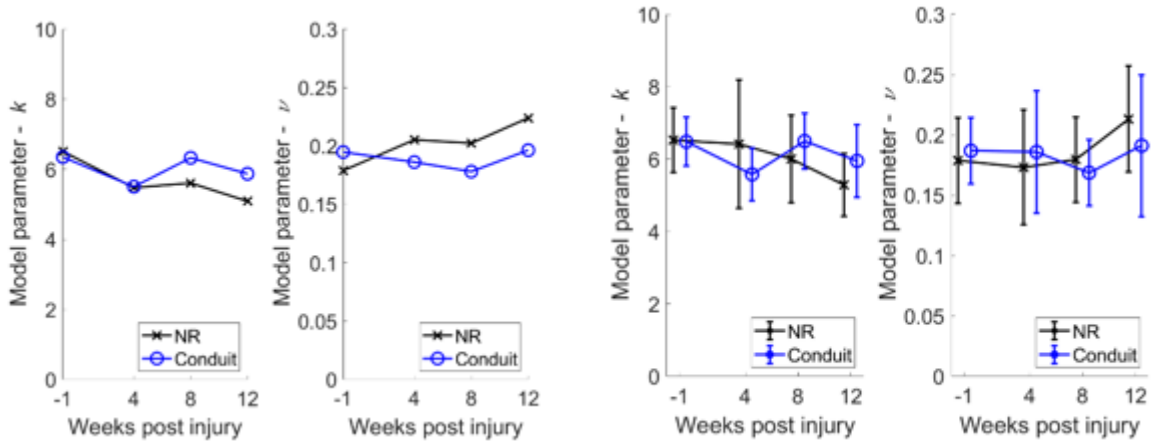

Figure 4-8. Kinetics of mean contraction curve (left) and mean ± SD kinetics of individual animals (right). Data in the right plots are offset for readability.

(4) 3. Discussion

Successful treatment of a peripheral nerve injury results in regeneration of the injured nerve and maintains function of the target muscle. Our previous work has shown the devastating effects of total nerve ablation injuries that can even exceed the loss of function in target muscles exceeding that of a VML injury model. However, a more modest injury would allow for greater understanding of the relationship between peripheral nerve and VML injuries. Thus, the goal of this study was to identify a potential injury model that would allow for appreciable and reproducible nerve regeneration within the 12-week time frame has previously been evaluated for VML repair. The injury created here was a partial peroneal nerve transection where approximately 50% of the peroneal nerve diameter was cut. This nerve transection was repaired using a PCL nerve conduit loaded with double-walled microspheres containing a subtherapeutic dose of GDNF. The no repair and nerve conduit both achieved similar functional recoveries and exhibited similar characteristics in histology, kinetics, and morphology after 12 weeks.

The kinetics analyzed in Figure 9 exhibited noticeable deviation between study groups at the baseline timepoint. This was likely due to small differences in experimental technique such as electrode placement and limb positioning. We note that the three separate datasets presented in Figure 9 were collected by three different experimenters. To account for these differences, the data were normalized to the baseline timepoint. One result from this analysis is that non-normalized comparisons of kinetics cannot be made between datasets. A notable group was the polytrauma condition for a concomitant increase in *k* with a decrease in *v*, demonstrate marked muscle function dysregulation. This pattern suggests that the muscle developed force very rapidly after a longer delay – a pattern that is consistent with the low maximal torque seen for this group.

The removal of synergistic muscles to the TA during the nerve injury creation removes ~15-20% of torque generation in the anterior compartment (Corona *et al.*, 2012, 2014b; J. a. Passipieri *et al.*, 2017; Mintz *et al.*, 2020b). Therefore, maximum theoretical recovery would be ~80 N-mm/kg across the treatment groups (for 100 N-mm/kg average at baseline). The injury model described here could allow full restoration of function in the TA up to the 80% theoretical maximum. The therapeutic intervention of the nerve conduit used for this study did not hinder as measured by histological examination of the nerve tissue. The GDNF dose included in the microspheres within the conduit were at the subtherapeutic levels (<97% of the therapeutic levels). This was performed to preserve the double-walled structure of the microspheres with the drug being encapsulated in the PLGA core. Historically, a substitute protein with similar molecular weight, such as lysozyme, was utilized to make microspheres with similar mechanical properties.(Kokai et al., 2010) In the current study, instead of utilizing a different protein, the same protein in the therapeutic nerve conduits, GDNF, was used but at subtherapeutic dose to preserve the double walled structure and the overall mechanical properties of the final nerve conduit, while not potentially elucidating its neurotrophic effects on the recovering nerve. This was also confirmed by the similar axonal and Schwann cell count with and without the use of nerve conduit. Therefore, the axonal regeneration achieved in this study could be further enhanced

with increased dosing of GDNF to elicit a more pronounced difference in future nerve repair studies. This was successful in demonstrating the potential use for this type of nerve conduit without significant immunological response or other complications during the surgical procedure. Despite this success, it was also seen from these results that the nerve injury model used here was not significant enough to cause long term effects to the TA muscle function. As shown in figure 1, functional recovery of the no repair animal was at or near the theoretical maximums with the synergistic muscles removed. This indicates that the partial nerve injury used here was ineffective at causing muscle atrophy or significantly degrading the functional torque of the TA at the time points analyzed. While these results are strongly encouraging, we still need to determine the exact balance between an injury model capable of being repaired and one that is sufficient to cause atrophy in the target muscle.

(4) 4. Conclusions and Clinical Significance

In this study, we utilized a polymer-based conduit as a wrap to protect the neurorrhaphy site following a partial transection of the peroneal nerve. Due to the unexpectedly modest nature of the induced nerve injury, the added presence of the nerve conduit (containing subtherapeutic doses of GDNF) did not alter neural tissue repair, or functional recovery of muscle, in any detectable fashion. Our results highlight the challenges of developing high-throughput small animal models that can be used as reliable testbeds for studying the mechanistic complexities of polytraumatic injuries as well as developing new treatment paradigms for more efficacious restoration of functional recovery. Nonetheless, it seems clear that greater focus on the early time course (< 1 month) and magnitude of the impact of peripheral nerve damage to the target muscle is key to a better understanding of VML polytrauma. Future studies will target more extensive peripheral nerve injuries, albeit short of critical size defects, as well as earlier time points of investigation (1-2 weeks rather than 4 weeks) in or to further optimize and enable the study of simultaneous nerve and muscle repair for traumatic extremity injuries. In this regard, our current work provides a rigorous combination of nerve and muscle metrics that can be used to assess

and accelerate progress in this field. The long-term goal is to combine the power of improved animal models, and the mechanistic data they can provide, with data-driven development and implementation of computational models (i.e., agent-based modeling;(Westman *et al.*, 2021)), and the predictive insights they can provide, to advance the understanding and treatment of complex polytraumatic VML injuries.

(4) 5. Methods and Materials

(4) 5.1 Animal Care

This study was conducted in accordance with the appropriate animal welfare guidelines. All animal procedures were approved by The University of Virginia Animal Care and Use Committee. 16 male 12-week-old, Lewis rats were used in this study (Charles River Laboratories). These animals were allowed ad libitum access to food and water and were pair housed for the duration of the study.

(4) 5.2 Nerve Conduit Fabrication

The preparation of the GDNF-containing polymer conduit has been previously described in detail (Kokai, Ghaznavi and Marra, 2010; Kokai *et al.*, 2011; Bliley *et al.*, 2015; Fadia *et al.*, 2020). From inside to outside, the nerve conduit is comprised of a single layer of poly(caprolactone) (PCL), a layer of double-walled microspheres and finally 4 layers of PCL (Fig. 10).

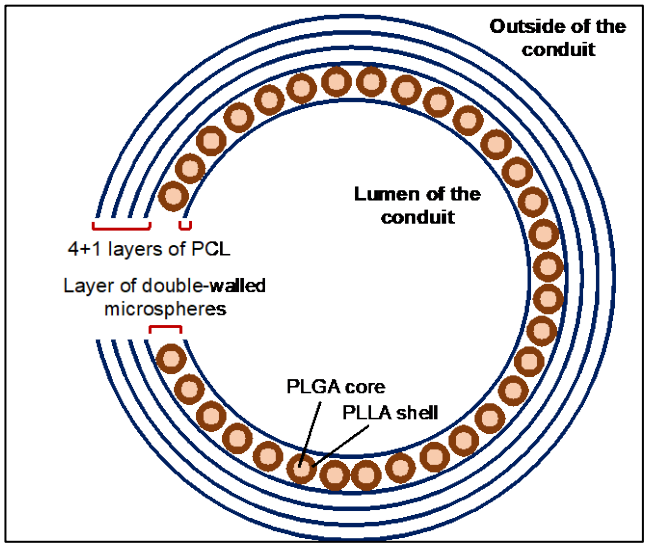

Figure 4-9. Schematic depiction of the cross-section of the nerve conduit including a total of 5 layers of poly(caprolactone) (PCL) as well as the layer containing double-walled microspheres composed of a PLGA core and a PLLA shell.

To fabricate the conduit, a 7% (v/v) poly(caprolactone) solution (440744, Sigma, St. Louis, MO) is prepared in ethyl acetate (270989, Sigma, St. Louis, MO), followed by addition of NaCl (S7653, Sigma, St. Louis, MO) sifted with a 30 μm sieve. Double-walled microspheres (Figure 1-B) are created by mixing poly(lactic-co-glycolic acid) (PLGA) (50:50, P2191, Sigma, St. Louis, MO) and poly(L-lactide) (PLLA) (94829, Sigma, St. Louis, MO) separately with dichloromethane (270997, Sigma, St. Louis, MO). A solution of GDNF (Recombinant Human GDNF Protein, R&D Systems, Minneapolis, MN) is prepared, lyophilized, and the dried pellet is added to the PLGA solution to be mixed with the PLLA solution. This emulsion is added in a dropwise fashion to a 0.5% PVA solution stirring at 900 rpm.

A glass mandrel rod of 0.8 mm diameter and 6 cm length is vertically dipped into the PCL solution. Immediately after the first dip, about 35 mg of double walled microspheres is added by rolling the mandrel coated with PCL. This was followed by 4 more vertical dips into the PCL solution to create the final nerve conduit with a wall thickness of 0.13-0.15 mm. The nerve conduit is then cut into 1 cm-long segments to be implanted to the animals, which included 7ng of GDNF per conduit. The drug in

this setting is used at non-therapeutic levels to function as a surrogate to create non-functioning microspheres with maintained physical properties and contained a dose that is >97% lower than the previously published therapeutic levels(Kokai, Ghaznavi and Marra, 2010; Kokai *et al.*, 2011; Bliley *et al.*, 2015; Fadia *et al.*, 2020).

(4) 5.3 Formation of Partial Peroneal Nerve Laceration

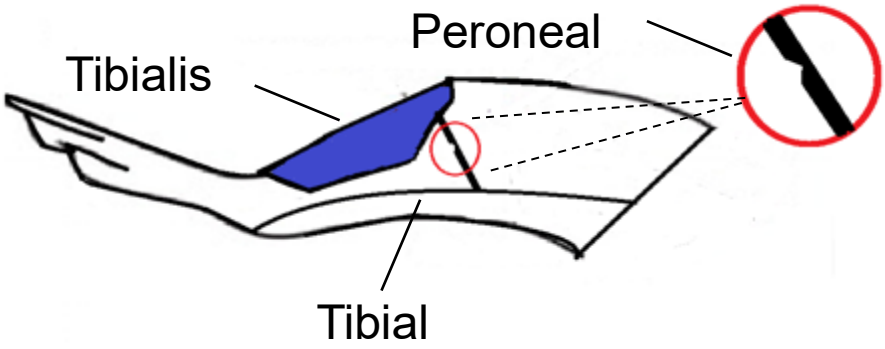

Figure 4-10. Partial Peroneal Nerve Injury Model. Graphic of the injury model, where a partial nerve transection was performed on the peroneal nerve to assess functional recovery in the tibialis anterior. The disruption of nerve fibers leading to the tibialis anterior should cause disruption of synapses with the muscle fibers in the tibialis anterior leading to a degradation of function of the muscle tissue.

Animals were anesthetized using inhaled isoflurane and the surgical area was aseptically prepared using alternating washes of povidone-iodine and ethanol solutions. The peroneal nerve was exposed as previously described(Passipieri *et al.*, 2019). Once exposed, the peroneal nerve was separated from the sural and tibial nerves using gentile dissection and microscissors were used to cut

50% of the nerve's width. Figure 10 indicates the approximate location of the injury in relation to the TA and the tibial nerve. Treatment groups received a single 10-0 nylon microsuture rejoining the cut ends and the nerve conduit was placed over the injury. The synergistic muscles to the TA, extensor digitorum longus (EDL) and extensor hallucis longus (EHL) were removed. Two microsutures were used to close the nerve conduit as shown in Figure 12D. 6-0 vicryl suture was used to close the muscle incision. Skin glue and 6-0 prolene were used for skin closure. Postoperative extended-release buprenorphine (Ethiqa XR) was administered subcutaneously.

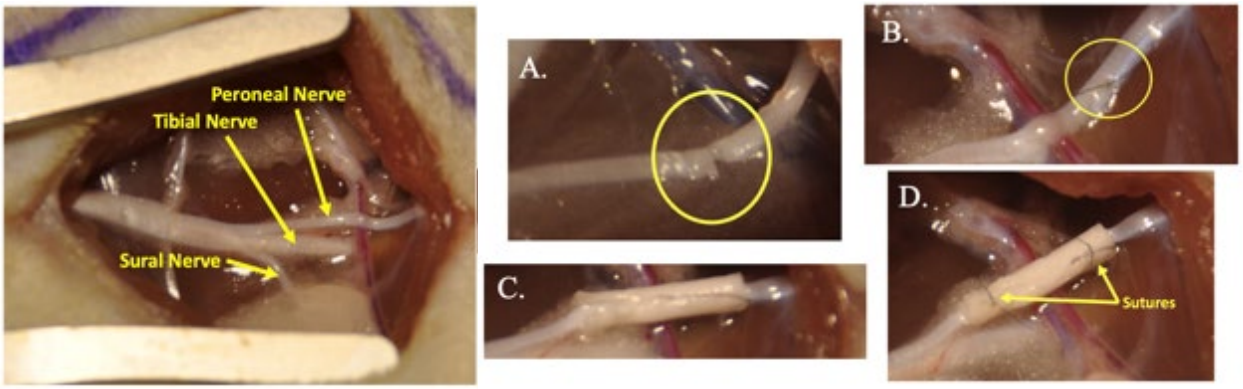

Figure 4-11. Partial Peroneal Nerve Transection and Application of PCL Conduit–
Demonstration of anatomy and injury model to the peroneal nerve. A) A partial nerve transection located ~1cm distal to the branching of the sciatic nerve.

(4) 5.4 In Vivo Functional Testing

Functional testing was performed on all animals prior to VML surgery to establish baseline torque responses for each animal. Testing was again conducted post-healing at three time points of

4-, 8-, and 12-weeks post-surgery, in vivo functional analysis was performed to assess recovery post-VML injury. Torque production of the subject's TA was measured in vivo as previously described (Corona *et al.*, 2014; Mintz *et al.*, 2016; Passipieri *et al.*, 2017). Rats were anesthetized (2% isoflurane; Henry Schein, Dublin, OH) and the left hindlimb was aseptically prepared. The rat was placed on a heated platform and the left foot was secured at a 90 angle to a footplate attached to the Aurora Scientific 305C-LR-FP servomotor (Aurora, ON, Canada). Two sterilized percutaneous needle electrodes (Chalgren, Gilroy, CA) were inserted superficially through the skin to stimulate the left peroneal nerve. An electrical stimulus was applied (Aurora Scientific Stimulator Model 701C) and stimulation voltage and electrode placement were optimized with continuous 1 Hz twitch contractions. Contraction of the anterior crural muscles leading to dorsiflexion of the foot was determined by measuring the maximal isometric tetanic torque over a range of stimulation frequencies sufficient to result in plateau of the torque response (10–150 Hz). At 12 weeks, animals were euthanized through CO_2 inhalation, and injured TA muscles, peroneal nerves, and contralateral controls were explanted, weighed, and frozen in preparation for imaging.

(4) 5.5 Histological and Immunofluorescence Examination of the muscle

TA muscles were explanted at sacrifice. All tissues were flash frozen in liquid nitrogen and stored at -80C until ready for sectioning. A cryotome was used to create 12 mm cross-sections of the treatment and control TA muscles for all animals in each group at 12 weeks. Hematoxylin and eosin staining was performed following standard procedures to assess cellular morphology and fibrosis, respectively. Images were captured at 4x and 10x (Nikon Upright Microscope). Histological images were examined, particularly in the region of injury to identify new fiber formation, cellular proliferation and growth, or potential fibrosis.

Other tissue sections were stained with immunofluorescent laminin antibody (Abcam, ab11575) stain conjugated to Alexa Fluor 488 (Abcam, ab150077). All antibodies were diluted in Dako Antibody Diluent (Dako Antibody Diluent S0809; Agilent Technologies). Images were captured by confocal

microscopy (Leica DMi8; Buffalo Grove, IL). Fiber cross sectional area (FCSA) and minimum feret diameter (MFD) were determined as previously described ((Christensen *et al.*, 2022). These images were enhanced and uniformly edited using the CLAHE (contrast limited adaptive histogram equalization) plugin of ImageJ (NIH). FCSA and MFD measurements were taken using the software SMASH, a semi-automatic muscle analysis program built in MatLab, developed by L.Smith and E.Barton from the University of Pennsylvania. A full detailed analysis of the SMASH software, it's functions and limitations may be found in (Smith and Barton, 2014).

(4) *5.6 Histological and Immunofluorescence Examination of the Nerve*

For the groups with no repair and nerve conduit, the peroneal nerve was explanted at the 12-week endpoint to include the repaired section, nerve conduit in total and 5 mm of neural tissue from both distal and proximal ends of the repair site. Tissues were processed similar as previously described(Passipieri *et al.*, 2021). Upon extraction, tissues were cryopreserved by using an embedding medium (Tissue-Tek® O.C.T. Compound, Sakura Finetek, Torrance, CA) and slowly submerging into 2-methlybutane sitting in liquid nitrogen. Frozen blocks were sectioned in 5 µm-thick slices for cross-sections using a cryostat. Sections included distal and proximal segments of the repair site (FIGURE FBB1). All sectioned slides were initially stained with hematoxylin and eosin (H&E) per manufacturer's guidelines. Images were captured with 10x magnification using Keyence BZ-X710 microscope (Keyence, Itasca, IL).

Sections were further stained for axons and Schwann cells. After cross-sectioning, slides stored in -80^{o}C were pre-processed with cold acetone. Blocking was performed using bovine serum albumin (A7906, Sigma, St. Louis, MO), gelatin (G704, Sigma, St. Louis, MO) and goat serum (G9023, Sigma, St. Louis, MO). The primary antibodies for S100 (1:100, ab34686, Abcam, Boston, MA) and neurofilament heavy chain (NEFH, 1:100, 13-1300, Thermo-Fisher Scientific, Waltham, MA)

were incubated overnight as a co-stain, followed by application of S100 secondary (1:1000, ab150079, Abcam, Boston, MA) and NEFH secondary (1:1000, A28175 Thermo-Fisher Scientific, Waltham, MA) for 1 hour. Finally, 4′,6-diamidino-2-phenylindole (DAPI, 1:1000, D9542, Sigma, St. Louis, MO) was incubated for 5 minutes and after washing, samples were cover-slipped using Fluoromount mounting medium (NB900-66726, Novus Biologicals, Centennial CO).

(4) 5.7 Kinetic Analysis

Kinetic analysis was conducted using custom code in MATLAB 2021a. Raw TA torque data files were parsed, the first 120 points (representing 60 msec) after stimulation were selected, 60 Hz lowpass filtered, normalized to the maximum force in the interval, and the parameters *k*, and *v*, were fit according to the following equation

$$Torque(t) = (1 - e^{-kt})^{1/v}$$

using MATLAB's "fit" function and the nonlinear least squares option. The lower bounds were set to 0 and 0.01 for *k* and *v*, respectively. The upper bounds were set to 30 and 1 for *k* and *v*, respectively. The midpoint of the range was used for a starting guess for both parameters. Cases for which the fit could not be calculated due to data quality were discarded. The data was quality controlled by only using fits for which the calculated R-squared value was greater than 0.95.

(4) 5.8 Statistical Analysis

All data are presented as mean ± standard deviation unless otherwise noted. Sample group sizes are given in respective figure captions, main text, or Materials and Methods sections. Where appropriate, the statistical significance of functional recovery data was determined by one-way or two-way ANOVA and Fisher's LSD. Functional recovery was evaluated within each time point (one-way

multiple-comparison analysis). This decision was based on the established scientific rationale in the field, namely, that functional recovery from nerve damage is time dependent. SMASH data was analyzed using the Brown-Forsythe and Welch ANOVA test with multiple comparisons. Axon and Schwann cell counts between the two groups from immunofluorescent stained nerve samples was compared using Student's T-test. Statistical analysis was conducted by using GraphPad Prism 8.0 for Windows (La Jolla, CA).

(4.3) REFERENCES

Bliley, J.M. *et al.* (2015) ‘Ethylene Oxide Sterilization Preserves Bioactivity and Attenuates Burst Release of Encapsulated Glial Cell Line Derived Neurotrophic Factor from Tissue Engineered Nerve Guides For Long Gap Peripheral Nerve Repair’, *ACS Biomaterials Science & Engineering*, 1(7), pp. 504–512. Available at: https://doi.org/10.1021/ab5001518.

Christensen, K.W. *et al.* (2022) ‘Assembled Cell-Decorated Collagen (AC-DC) Fiber Bioprinted Implants with Musculoskeletal Tissue Properties Promote Functional Recovery in Volumetric Muscle Loss’, *Advanced Healthcare Materials*, 11(3), p. 2101357. Available at: https://doi.org/10.1002/adhm.202101357.

Corona, B.T. *et al.* (2012) ‘Further Development of a Tissue Engineered Muscle Repair Construct In Vitro for Enhanced Functional Recovery Following Implantation In Vivo in a Murine Model of Volumetric Muscle Loss Injury’, *Tissue Engineering Part A*, 18(11–12), pp. 1213–1228. Available at: https://doi.org/10.1089/ten.tea.2011.0614.

Corona, B.T. *et al.* (2014) ‘Implantation of In Vitro Tissue Engineered Muscle Repair Constructs and Bladder Acellular Matrices Partially Restore In Vivo Skeletal Muscle Function in a Rat Model of Volumetric Muscle Loss Injury’, *Tissue Engineering Part A*, 20(3–4), pp. 705–715. Available at: https://doi.org/10.1089/ten.tea.2012.0761.

Dyer, S.E. *et al.* (2022) ‘Administration of particulate oxygen generators improves skeletal muscle contractile function after ischemia-reperfusion injury in the rat hindlimb’, *Journal of Applied Physiology*, 132(2), pp. 541–552. Available at: https://doi.org/10.1152/japplphysiol.00259.2021.

Fadia, N.B. *et al.* (2020) ‘Long-gap peripheral nerve repair through sustained release of a neurotrophic factor in nonhuman primates’, *Science Translational Medicine*, 12(527), p. eaav7753. Available at: https://doi.org/10.1126/scitranslmed.aav7753.

Fu, S.Y. and Gordon, T. (1995) ‘Contributing factors to poor functional recovery after delayed nerve repair: prolonged denervation’, *Journal of Neuroscience*, 15(5), pp. 3886–3895. Available at: https://doi.org/10.1523/JNEUROSCI.15-05-03886.1995.

Garg, K. *et al.* (2015) ‘Volumetric muscle loss: Persistent functional deficits beyond frank loss of tissue’, *Journal of Orthopaedic Research*, 33(1), pp. 40–46. Available at: https://doi.org/10.1002/jor.22730.

Garg, K., Corona, B.T. and Walters, T.J. (2015) ‘Therapeutic strategies for preventing skeletal muscle fibrosis after injury’, *Frontiers in Pharmacology*, 6. Available at: https://www.frontiersin.org/articles/10.3389/fphar.2015.00087 (Accessed: 31 October 2022).

Greising, S.M., Dearth, C.L. and Corona, B.T. (2016) ‘Regenerative and Rehabilitative Medicine: A Necessary Synergy for Functional Recovery from Volumetric Muscle Loss Injury’, *Cells Tissues Organs*, 202(3–4), pp. 237–249. Available at: https://doi.org/10.1159/000444673.

Grogan, B.F., Hsu, J.R. and Consortium, S.T.R. (2011) ‘Volumetric Muscle Loss’, *JAAOS - Journal of the American Academy of Orthopaedic Surgeons*, 19, p. S35.

Kokai, L.E. *et al.* (2011) ‘Sustained Growth Factor Delivery Promotes Axonal Regeneration in Long Gap Peripheral Nerve Repair’, *Tissue Engineering Part A*, 17(9–10), pp. 1263–1275. Available at: https://doi.org/10.1089/ten.tea.2010.0507.

Kokai, L.E., Ghaznavi, A.M. and Marra, K.G. (2010) ‘Incorporation of double-walled microspheres into polymer nerve guides for the sustained delivery of glial cell line-derived neurotrophic factor’, *Biomaterials*, 31(8), pp. 2313–2322. Available at: https://doi.org/10.1016/j.biomaterials.2009.11.075.

Mintz, E.L. *et al.* (2016) ‘Applications of In Vivo Functional Testing of the Rat Tibialis Anterior for Evaluating Tissue Engineered Skeletal Muscle Repair’, *Journal of Visualized Experiments : JoVE*, (116), p. 54487. Available at: https://doi.org/10.3791/54487.

Mintz, E.L. *et al.* (2020a) ‘Long-Term Evaluation of Functional Outcomes Following Rat Volumetric Muscle Loss Injury and Repair’, *Tissue Engineering Part A*, 26(3–4), pp. 140–156. Available at: https://doi.org/10.1089/ten.tea.2019.0126.

Mintz, E.L. *et al.* (2020b) ‘Long-Term Evaluation of Functional Outcomes Following Rat Volumetric Muscle Loss Injury and Repair’, *Tissue Engineering Part A*, 26(3–4), pp. 140–156. Available at: https://doi.org/10.1089/ten.tea.2019.0126.

Passipieri, J. a. *et al.* (2017) ‘Keratin Hydrogel Enhances In Vivo Skeletal Muscle Function in a Rat Model of Volumetric Muscle Loss’, *Tissue Engineering Part A*, 23(11–12), pp. 556–571. Available at: https://doi.org/10.1089/ten.tea.2016.0458.

Passipieri, J.A. *et al.* (2019) ‘In Silico and In Vivo Studies Detect Functional Repair Mechanisms in a Volumetric Muscle Loss Injury’, *Tissue Engineering Part A*, 25(17–18), pp. 1272–1288. Available at: https://doi.org/10.1089/ten.tea.2018.0280.

Passipieri, J.A. *et al.* (2021) ‘Adipose Stem Cells Enhance Nerve Regeneration and Muscle Function in a Peroneal Nerve Ablation Model’, *Tissue Engineering Part A*, 27(5–6), pp. 297–310. Available at: https://doi.org/10.1089/ten.tea.2018.0244.

Smith, L.R. and Barton, E.R. (2014) ‘SMASH – semi-automatic muscle analysis using segmentation of histology: a MATLAB application’, *Skeletal Muscle*, 4(1), p. 21. Available at: https://doi.org/10.1186/2044-5040-4-21.

Westman, A.M. *et al.* (2021) ‘Agent-based model provides insight into the mechanisms behind failed regeneration following volumetric muscle loss injury’, *PLOS Computational Biology*, 17(5), p. e1008937. Available at: https://doi.org/10.1371/journal.pcbi.1008937.

(4.4) Conclusions and Future Directions

In developing an injury model for peroneal nerve injury in relation to VML, we have established some meaningful groundwork. In order to evaluate functional deficit in relation to peroneal nerve damage, the injury must cause denervation or atrophy of the target muscle, while still maintaining the ability to recover adequately given a regenerative therapeutic. In our previous work, we established that total peroneal nerve ablation injuries were too severe and investigated the possibility of partial nerve transections. Due to the complete lack of functional recovery with or without repair in the total peroneal nerve ablation this would not be a suitable injury model for future work. Particularly, the maximal isometric torque seen was lower than VML model injuries alone with no nerve damage. Thus, the need for a more modest injury model. As depicted in Figure 4-11, total ablation injury models used previously in our lab created injuries that were beyond the capability of repair (blue lines). The functional deficit in this injury model, with or without repair, was more traumatic than a published standard 20% VML injury model (Corona *et al.*, 2012, 2014; Mintz *et al.*, 2016; Passipieri *et al.*, 2019b; Christensen *et al.*, 2022) receiving no repair (green dashed line) and showed to be irrecoverable. In the data presented in the paper contained within this chapter, partial nerve transection injuries (red lines) treated with the nerve conduit or receiving no repair reached near theoretical maximums (purple dashed line). This theoretical maximum was discussed in more detail in the previous sections, but is due to the removal of synergistic muscles to the TA. In figure 4-11, we have also included 2 unpublished sets of data that also utilized the partial peroneal nerve transection. In this case, both groups received a nerve conduit, where one group also received a subsequent VML injury model. This could be a promising approach for future nerve injury models. There were a few pitfalls in the development of this work exploring partial nerve transections. The most apparent is the lack of meaningful functional deficit in the partial peroneal nerve transection model. The no repair groups were able to recover to a greater extent than we believed they would. Encouragingly from this work, we were able to identify an effective repair and a PCL conduit that did

not inhibit nerve recovery in any way. Future work could utilize the model we have developed with modifications.

An alternative strategy for a nerve VML polytrauma model injury is required to move this work forward. One potential strategy could be to alter the timing of data collection. Perhaps the peroneal nerve injury in this chapter would be suitable to analyze at early time points of repair in the 1–4-week range. Another alternative could be performing the partial transection performed in this work and further damage the remaining nerve in a manner relevant to polytrauma injury, such as crushing. We believe with minor tweaks to the current surgical model an effective nerve VML polytrauma model will be established.

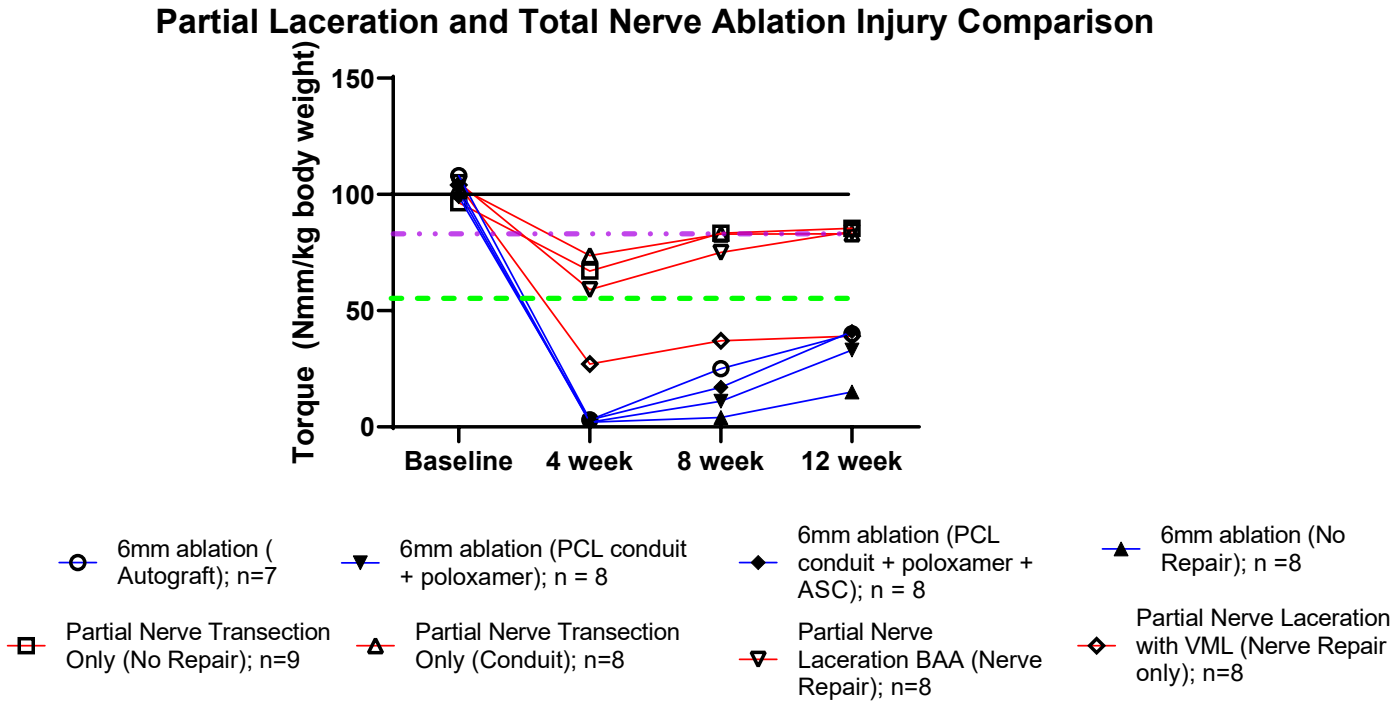

Figure 4-12. Nerve Injury Model Comparison– Torque generation values pre-injury (baseline) and at 4, 8, and 12-weeks post-repair following complete peroneal nerve ablation (6mm gap unless otherwise noted) with or without subsequent VML injury (blue lines) and partial peroneal nerve transection with or without a nerve conduit (red lines). Group size is indicated for each group as well as treatment received. At 12 weeks of repair, no significant difference was noted between the partial nerve transection groups with or without repair.

Chapter 5: Final Thoughts

The overarching goal of the work presented in this dissertation was to explore the potential for regenerative therapeutics designed for treatment of the most devastating extremity trauma injuries, that is, VML polytrauma. This work is of broad relevance to the fields of regenerative medicine and tissue engineering, with a focus on neuromuscular repair. We described three different approaches to this end: 1) tissue engineering methods for co-culturing multiple cell types *in vitro* (Chapter 2), 2) a novel scaffold biofabrication process for functional regeneration in an established VML injury model (Chapter 3), and 3) development of animal models for improved evaluation of polytraumatic VML injury and repair (Chapter 4). Due to the complexity of VML polytrauma, much of the current work in the field is focused on understanding and managing individual components of tissue injury. We know that injuries created in traumatic events are seldom focused to only one area and can be significantly more complex, involving multiple tissue types. This highlights the importance of this work, aiming towards targeting and regenerating numerous components of related injuries simultaneously. The complexity of the problems being addressed is increased but will ultimately produce more viable and functional recovery in long term clinical outcomes.

In Chapter 2, we aimed to create void filling, three-dimensional tissue constructs *in vitro* with the goal of implantation into a VML injury. We described bioprinted HA bioinks containing muscle and neuronal co-cultures capable of cell proliferation and differentiation on ECM sheet-based scaffolds, ultimately creating nTEMR cellularized constructs. The addition of three-dimensional co-culture allows for creation of more competent and functional tissue implants than when only one cell type is introduced to the scaffold prior to implantation, particularly when combined with mechanical stimuli to further improve the differentiation of tissues. Ultimately, producing innervated and vascularized tissue *in vitro* would have significant clinical implications and the first steps towards this goal has been demonstrated here. The incorporation of bioprinting technologies allows the size and shape of the

bioprinted construct to be adapted to entirely fill any void created by a VML or even a polytraumatic injury affecting multiple extremities. Creation of a void-filling, three-dimensional, innervated tissue construct has never been done to my knowledge. The *in vitro* results from this chapter showed great promise and with further adaptation could indeed head towards *in vivo* implantation in a VML model. The development of an nTEMR construct with innervated muscle tissue and complex muscular organization would be ideally suited for VML injury repair and other devastating extremity injuries that need more than a two-dimensional, sheet based therapeutic. Issues in timing the proper introduction of tissues in co-culture still need to be addressed along with adjustments to cell densities to produce the most biologically relevant and mimetic tissue. I suggest low neuron to muscle cell densities, along with an initial delay in introduction of multiple progenitor cell types to allow sufficient adhesion and proliferation of each cell type.

In Chapter 3, a novel, cellularized microfiber collagen scaffold was biomanufactured with tunable properties and the potential for scalability and treatment of polytraumatic myotendinous injury. These scaffolds have been shown capable of growing multiple cell types and regenerating muscle and tendon tissue *in vivo*. Initially designed for treatment of tendon injuries, these collagen-based scaffolds are already commercially available from Embody, LLC in Norfolk, VA. Due to the success and biomanufacturing capabilities of these scaffolds, it was of interest to investigate their potential for use in soft tissues as well as tendon. The results of this chapter were strongly encouraging as to the potential of these scaffolds to regenerate muscle tissue in a functionally relevant capacity. In the future these scaffolds may be adapted for polytraumatic injuries involving both muscle and tendon loss at the myotendinous junction. The tunable properties and architectures of the extrusion print method are ideal for further adaptation of these scaffolds. Scaffolds may be designed with multiple architectures within a single scaffold, one portion containing mechanical and morphological properties akin to muscle and one portion containing mechanical and morphological properties akin to tendon. Each section could be seeded with progenitor cells relevant to their own type, much like muscle

progenitors were used in the VML injury published from this work. This would be the first attempt, to my knowledge, of repairing a myotendinous junction targeting both tissue types simultaneously.

In Chapter 4, a recoverable, partial peroneal nerve transection injury model was developed for its potential use in polytraumatic injury research. Due to the complex nature of polytraumatic VML injuries leading to damage of multiple tissues, like muscle and nerve, it is vital to have an established model capable of analyzing the effects of nerve damage on muscle tissue, particularly when connected with a VML injury. In a VML injury with upstream nerve damage, the atrophy of the tissue may be greater than any possible amount of regeneration from an implanted therapeutic. Therefore, it is essential to repair the nerve prior to or subsequently with the VML injury. The timing of nerve repair is an essential area of study to understand how to best treat these types of polytraumatic injuries. A peripheral nerve injury model is necessary that can be functionally repaired within an appropriate time, while still demonstrating sufficiently relevant damage to the target muscle tissue. The partial nerve transection injury model presented in this chapter showed the capability of the nerve to be fully restored using our PCL nerve guide conduit but was too modest to produce relevant damage to the target muscle tissue at the time points analyzed. Total ablation injuries have already shown to be too severe to facilitate regeneration within an appropriate time frame. However, continuation of this work could certainly identify methods for meeting a middle ground, such as varying the type of damage done to the nerve or varying the points of data collection to analyze the impact of the nerve injury. Promisingly in this study, the nerve guide conduit was capable of providing nerve regeneration with no negative impacts using a subtherapeutic level of GDNF. This serves to validate the future potential for the injury model, as it allowed for accurate and consistent application of the nerve conduit without drawbacks. Future work should focus on earlier time points of healing, in the 1-to-2-week range instead of beginning assessment at the earliest time of 4 weeks. When a successful model has been established this work can move towards analyzing a VML injury in conjunction with polytrauma, specifically peroneal nerve damage, to research even more clinically relevant repairs.

As is the intent of pre-clinical animal studies, the greatest implications of this work revolve around the potential translational impact on human patients. Providing functional restoration to patients impacted by polytraumatic extremity injury is of the utmost importance. The work presented here contributes, in a variety of ways, to future studies that will enhance the development and efficacy of tissue engineering strategies for polytraumatic injury. I hope to see the advancement of regenerative, biomanufactured therapeutics to leap into the clinic and know this work supports that possibility.